This is to certify that the
thesis entitled

MECHANICAL PROPERTIES OF THERMOELECTRIC
SKUTTERUDITE MATERIALS

presented by

ROBERT SCHMIDT

has been accepted towards fulfillment
of the requirements for the

MASTER degree in MATERIALS SCIENCE

Eldon D. Case
Major Professor's Signature

December 16, 2010
Date

MSU is an Affirmative Action/Equal Opportunity Employer

MECHANICAL PROPERTIES OF THERMOELECTRIC SKUTTERUDITE MATERIALS

By

Robert Schmidt

A THESIS

Submitted to
Michigan State University
in partial fulfillment of the requirements
for the degree of

MASTER OF SCIENCE

Materials Science Engineering

2010

ABSTRACT

MECHANICAL PROPERTIES OF THERMOELECTRIC SKUTTERUDITE MATERIALS

By

Robert Schmidt

Thermoelectric materials are semiconductor materials that can generate an electric current from a thermal gradient. To be used in a device, the thermoelectric material must be able to withstand the applied thermal and mechanical forces without failure. The powder processing, microstructure, elastic moduli, thermal expansion and hardness properties were measured for three thermoelectric skutterudite materials, two n-type skutterudite materials of composition $Co_{0.95}Pd_{0.05}Te_{0.05}Sb_3$, either with or without doping with 0.1 atomic % cerium, and a p-type skutterudite of composition $Ce_{0.9}Fe_{3.5}Co_{0.5}Sb_{12}$. The ball milling portion of powder processing was most efficiently accomplished in one step with ethanol, producing a powder that was hot pressed into billets with an average grain size of less than 2 μm. Elastic moduli were determined for all billets, with Young's modulus approximately 135 GPa for n-type, and 129 GPa for p-type, varying according to porosity and composition. Moduli decreased linearly with temperature until 523 K to 623 K, above which a viscoelastic region began and moduli decreased more rapidly. The bulk coefficient of thermal expansion (CTE) was 10.0 x 10^{-6} K^{-1} for non-cerium doped n-type, 11.2 x 10^{-6} K^{-1} for cerium doped n-type, and 13.0 x 10^{-6} K^{-1} for p-type. The p-type material had a lattice parameter of 9.1241 Å at 303 K. The CTE value determined by x-ray diffraction was the same as the CTE measured from the bulk specimen. A new phase appeared in X-ray diffraction of the p-type material at 603 K and remains stable after cooling.

ACKNOWLEDGEMENTS

I acknowledge the funding from the Department of Energy, Grant DE-FC26-04NT42281, without which none of this work could have been done. Also, funding for the RUS equipment from DURIP grant N-00014-09-1-0785.

I would like to acknowledge all my co-authors on the room temperature properties paper [Schmidt 2010], Jennifer E Ni for taking all the SEM micrographs and consultation on RUS and XRD analysis, Professor Eldon D. Case for directing the project and keeping everything moving, corresponding with the publisher, advising in all the experiments, and extensive writing and revising work, Professor Jeffrey S. Sakamoto for providing the specimens for use in the study, writing of the paper's introduction and review of the paper, Daniel C. Kleinow for powder processing and training on use of the powder processing equipment for specimens SKD-Wet1 and SKD-Wet2, Bradley L. Wing for powder processing of SKD-Wet3 and RUS analysis, Ryan C. Stewart for powder processing of SKD-Wet3 and RUS analysis, and Edward J. Timm for creating the ingots used to make the specimens, hot pressing all of the powders into billets, cutting all the billets into specimens and for use and maintenance of the powder processing equipment.

Thank you to the High Temperature Materials Laboratory at Oak Ridge National Laboratory. I would like to acknowledge the director, Edgar Lara-Curzio, for his support on and accepting the independent user program proposal 2009-031, Elastic moduli and coefficient of thermal expansion for n- and p-type skutterudite thermoelectric materials, and making the resources of the laboratory available for use. I would like to

acknowledge my primary contact for the user proposal, Rosa Trejo. Rosa Trejo reserved, prepared, maintained and trained me on using the high temperature RUS equipment and the TMA machine. Thank you to E. Andrew Payzant for setting up the XRD experiment and training on the analysis software, and Roberta Peascoe-Meisner for operating the XRD equipment.

I would like to acknowledge my advisor, Professor Eldon Case, for his patient advising and teaching throughout the work on this thesis.

TABLE OF CONTENTS

LIST OF TABLES

LIST OF FIGURES

1 Introduction

Thermoelectric materials are semiconductor materials that develop an electrical potential across the material when subjected to a temperature gradient. When several legs of thermoelectrics are wired together in series, the thermoelectric materials may be used for energy harvesting from a heat source. Each leg is individually subjected to a temperature gradient in parallel, but several legs are wired together in series, typically tens to hundreds of legs in a single circuit.

Thermoelectric materials, by design, are placed in a condition where the material has a thermal gradient across the material, typically a few hundred degrees Kelvin differential over a distance of a few millimeters. In addition, each use subjects the thermoelectric device to a thermal gradient. Attached to each end of the thermoelectric material is a current collector, such as titanium or copper, to connect to the circuit. The current collector has a different thermal expansion coefficient than the thermoelectric material. As a result of the differing expansion coefficients, the thermoelectric material experiences stresses around the current collector that change with temperature. The thermal stresses from the thermal expansion mismatch and thermal gradient, along with the external stresses from vibrations or other loads, may lead to cracking of the thermoelectric material. In nonisotropic thermoelectric materials, the thermoelectric material itself may have thermal expansion anisotropy, [Zhao 2009, Yang 2009a, Fujishiro 2005, Ren 2006, Kenfaui 2010, Salvador 2009], although the skutterudite structure is isotropic and not a concern in this thesis.

The basic binary skutterudite structure is a cubic structure, consisting of eight expanded simple cubic structures of cobalt atoms, with rings of 4 antimony atoms inside 6 of the 8 cubes of cobalt. The other two cobalt cubes are unfilled cages that are sufficiently large to accept a filling atom. Since skutterudite has a cubic structure, the thermal expansion is isotropic [Nye 1957]. In the case of one material studied in this thesis, $Ce_{0.9}Fe_{3.5}Co_{0.5}Sb_{12}$, the structure can be looked at as building from the binary skutterudite form of Fe_4Sb_{12}, with the iron partially substituted with cobalt, and the structure filled with cerium.

1.1 Fracture and mechanical failure of thermoelectric devices

For the purposes of design of thermoelectric devices, the mechanical properties need to be characterized. In general, thermoelectric materials are brittle, such as Zn_4Sb_3 [Ueno 2005], $CoSb_3$ [Salvador 2009, Yang 2009a], PbTe [Salvador 2009], and lead antimony silver tellurium compounds (LAST) [Ren 2006]. A molecular dynamics model has shown that a nanowire of $CoSb_3$ may exhibit ductile fracture, although the same study notes the brittle behavior observed in the bulk $CoSb_3$ and all known experimental specimens tested to date [Yang 2009b].

According to linear elastic fracture mechanics, fracture in brittle materials is caused by the stress intensity factor exceeding a critical value [Wachtman 1996]. The stress intensity increases as the flaw or crack size increases. In practice, the fracture strength of a brittle material is determined by the largest flaw in the region of applied stress [Wachtman 1996, Ren 2006]. In a machining experiment on silicon nitride, the

machined surface displayed microcracking and grain pullout as a result of surface grinding [Xu 1995].

Grinding operations are common methods of cutting and surface finishing of ceramics. In surface grinding, the workpiece is affixed to a table under a grinding wheel. The grinding wheel is positioned typically with its' axis of rotation toward the front of the machine. The table is moved laterally in the x and y direction under the grinding wheel to remove a small amount of material on the top with each pass. The grinding process is capable of producing a very flat surface on a ceramic, with flatness tolerances of less than 1 μm possible [Grzesik 2008]. The process produces significant forces between the spinning friction blade and the workpiece below, forces that may be capable of microcracking and fracture if not managed [Xu 1995].

In a grinding experiment, the primary mechanism for material removal is grain dislodgement [Xu 1995]. The depth of the microcracked zone is related to the depth of the damage from microcracking and grain pullout, as well as the grinding force applied [Xu 1995]. Xu et al. anticipated a higher resistance to microcracking in fine grain material, resulting in higher grinding forces on the fine grained material, and confirmed through experiment that higher grinding forces were required on fine grained material [Xu 1995].

One study of fracture strength in LASTT examined the specimen sides and fractured surfaces for damage and the critical flaw. The damage observed included grain pullout, edge cracks, and internal microcracking [Ren 2006]. The authors suggested the damage may have been caused by cutting and polishing (Figure 2) [Ren 2006]. Grain pullout occurs after microcrack damage at the grain boundary [Xu 1995]. The grain

pullout indicated the polishing operation introduced microcracks to the affected zone of the operation surface.

A common thermoelectric material, Bi_2Te_3, has been studied for microcracking damage during sintering. Bi_2Te_3 is well recognized as anisotropic, with the coefficient of thermal expansion measured as $12.9 \times 10^{-6} K^{-1}$ along the a axis of the crystal and $22.2 \times 10^{-6} K^{-1}$ along the c axis [Francombe 1958]. Due to thermal expansion anisotropy (TEA), randomly oriented grains can have potentially large differences in thermal expansion rates and corresponding stresses. One way that the potential for and degree of microcracking can be lessened is by orienting the grains such that the individual grains are bordered by grains in a similar orientation [Jiang 2005]. Preferential orientation in Bi_2Te_3, intentionally introduced during sintering by spark plasma sintering, resulted in a bending strength increase of 7 to 8 times over the original zone-melted material before processing, to a final bending strength of 80 MPa [Jiang 2005]. The orientation in the pressing direction was preferential to the c-axis, with an orientation factor of 0.85, measured by the Lotgering method [Jiang 2005]. Similar results from preferential orientation were found on $Bi_2Te_{2.85}Se_{0.15}$ with hot pressing used for densification, and the degree of orientation increased with increasing hot pressing temperature [Seo 1997].

Numerical simulation has shown that larger grains produce a large field of microcracks prior to crack propagation [Johnson 2001]. As grain coarsening occurs during sintering, the larger grains may create microcrack fields during cooling. The model begins with a macrocrack, and then applies stresses similar to what may occur during cooling of a material with TEA [Johnson 2001, Tvergaard 1988]. During the cooling, Johnson described "a cloud of microcracks" in front of the macrocrack, delaying

fracture [Johnson 2001, p. 363]. The microcrack cloud increased in size and significance in preceding crack growth when grain to grain variation in residual stress was increased, such as in a material with large TEA [Johnson 2001]. Thus, simulation predicts a large cloud of TEA-induced microcracking ahead of a propagating crack.

The microcracking of brittle materials reduced elastic moduli [Case 1993], reduced strength, and reduced dielectric strength [Shin 1998]. Microcracking may be added intentionally, but microcrack damage has been overlooked before [Case 2005]. The thermoelectric materials in this study are brittle, and mechanical testing and materials properties were studied based on established methods for testing of similar brittle materials [Wachtman 1996, Ren 2006, Ni 2010]. Testing methods included Vickers and nano indentation, X-ray diffraction, resonance methods, and scanning electron microscopy (SEM) micrograph analysis.

1.2 X-ray Diffraction Measurement

X-ray diffraction studies can be used to determine lattice parameter and thermal expansion rate. As the skutterudite thermoelectric material has been developed, the filling and substitution atoms have been changed to optimize for the desired characteristics. The lattice parameter of the skutterudite structure may increase by filling or substituting atoms. Recknagel measured the lattice parameter as 0.90353(3) nm for unfilled $CoSb_3$ [Recknagel 2007]. The lattice parameter of $CoSb_3$ agreed well with other literature work, 0.90385 nm [Meisner 1998], 0.90345 nm [Caillat 1996] and 0.9036(5) nm [Kraemer 2005]. As tellurium was substituted for antimony in $CoSb_{3-x}Te_x$ for concentrations x of 0 to 0.10, the lattice parameter increased linearly from 0.90350 nm to 0.90442 nm [Liu 2007].

Similar to substitution, filling the skutterudite structure with an atom increased the lattice parameter. Yang measured structural properties of misch-metal-filled skutterudites, of formula $Mm_yFe_{4-x}Co_xSb_{12}$, where Mm is the misch-metal combination of primarily Ce, La, Nd and Pr [Yang 2007]. Yang reported a linear increase in lattice parameter as both the concentration of Mm was increased and the proportion of Fe was increased. Extrapolating Yang's result to the unfilled binary skutterudite, $CoSb_3$, the lattice parameter fit with established values, further noting that the use of Mm increased the lattice parameter more than an equal amount of a single lanthanide element [Yang 2007]. Yang speculates that the additional strain created by the mix of filling species makes the lattice parameter expand more than measured for skutterudites filled with a single species. The thermal conductivity, thermopower and electrical resistivity are unaffected by the distortion caused by using Mm [Yang 2007].

Thermal expansion measurements of bulk materials were compared with the expansion of the lattice parameter. The partially filled skutterudite $Mm_yFe_{4-x}Co_xSb_{12}$, with misch-metal concentrations of 0.82 and 0.88 yielded a thermal expansion coefficient of 11.35×10^{-6} K^{-1} [Yang 2007]. The thermal expansion coefficient compares to the unfilled $CoSb_3$ thermal expansion coefficient of 6.36×10^{-6} K^{-1} between 300 and 930 K measured by Caillat [Caillat 1996]. The coefficient measured by Caillat [Caillat 1996] for $CoSb_3$does not agree with Yang [Yang 2007] or the measurements in this thesis, but adding dopants is expected to increase the thermal expansion coefficient.

1.3 Resonance Measurement of Elastic Moduli

One common non-destructive method for measuring the elastic moduli of a specimen is through resonance methods. Ravi et al. [Ravi 2008], Recknagel et al. [Recknagel 2007], Salvador et al. [Salvador 2006] and Schmidt et al. [Schmidt 2010] measured the elastic moduli of antimony-based skutterudite materials by resonance methods. Several members of our group contributed to the elastic moduli measurements [Schmidt 2010], and their contributions are further detailed in the Acknowledgements section of this thesis. The Young's moduli at room temperature for all the antimony-based skutterudite specimens measured by Ravi, Recknagel, Salvador and Schmidt ranged from 127 to 148 GPa [Ravi 2008, Recknagel 2007, Salvador 2006], and these values of Young's modulus provide a reasonable expectation for Young's modulus of similar antimony-based skutterudites.

1.4 Scanning Electron Microscopy Observation

Scanning electron microscopy has been used to observe many material properties, including material cracking behavior [Case 1984, Case 1993, Zhao 2009], proper sintering and grain size evaluation [Schmidt 2010, Ren 2006, Kenfaui 2010, Hasselman 1993], and inclusions or porosity [Salvador 2009, Ren 2006, Schmidt 2010, Hasselman 1993]. Sintering has been shown to be able to cause cracking and reduce the elastic moduli [Jiang 2005, Case 1993], and SEM microscopy can be used to examine a specimen for cracking in a densified specimen. The SEM may be used to produce a micrograph for grain size evaluation by the line intercept method. The size of the grains can be used to determine if grain coarsening occurred during sintering. Coarsening

results are observable by SEM micrograph as larger grains or as microcracking driven by larger grains in anisotropic materials [Johnson 2001].

1.5 Applications of Thermoelectric Materials

The application of thermoelectric materials in waste heat recovery is promising. Thermoelectric materials are appropriate to use in applications where the temperature difference is no longer sufficient to run a mechanical device, such as the remaining heat after running an engine or turbine [Liu 2007]. Skutterudite thermoelectric materials may be appropriate in applications that Bi_2Te_3 may have been considered for previously, or for applications at higher temperature than Bi_2Te_3 can operate [Liu 2007].

Use of thermoelectric materials as a replacement for refrigerators is unlikely. Replacing chlorofluorocarbons can be done using thermoelectric materials, but thermoelectrics are relatively poor in energy efficiency at removing heat, when compared to compressor based refrigeration. Due to poor efficiency, application of thermoelectric materials as refrigeration is unlikely outside niche and small applications, even when considering the highest theoretically possible ZT [Feldman 1995].

Overall, applications of thermoelectric materials all require knowledge of the elastic moduli, fracture toughness, and thermal expansion behavior of the thermoelectric material. The measurements of the mechanical properties are a necessary part of developing new materials for application.

2 Expe

2.1 Spe

2.1.1 E

of the c

ingot.

Univers

Size U

apped

sealed i

ealed

2.1.2 P

ingot of

SS-316n

in a pla

emblec

was skip

Appen

above bo

2 Experimental Procedure

2.1 Specimen preparation and microstructural characterization

2.1.1 Billet fabrication

For both the n-type and p-type skutterudite specimens, approximately 100 grams of the constituent materials melted together in a sealed glassy carbon crucible to cast an ingot. The ingots were prepared by Ed Timm (Mechanical Engineering, Michigan State University) and Professor Jeffrey Sakamoto (Materials Science Engineering, Michigan State University), with the materials mixed inside a glove box. The mixed materials were capped inside a glassy carbon crucible, removed from the glove box, evacuated and sealed in a fused silica tube. The crucible was then placed in a rocking furnace to be melted into a solid ingot.

2.1.2 Powder processing

The powder processing procedure consisted of three general operations. First, the ingot of skutterudite was crushed, ground, sieved and reground (CGSR) until the resulting powder passed through a 75 μm sieve. Second, the CGSR powder was milled in a planetary ball mill to further reduce the particle size. Finally, the milled powder was remilled with ethanol or hexane added to the ball mill jar. The second step, dry milling, was skipped for processing of batches 2, 3 and 4 of JSp-SKD-15 and all of JSn-SKD-14 (Appendix A).

Each powder processing step was performed inside a glovebox (Omni-Lab double glove box with oxygen sensor and moisture sensor, Vacuum Atmospheres Company,

Hawthorne, CA) and maintained with an argon atmosphere. The atmosphere was continuously circulated through the equipped purifier to remove oxygen, resulting in oxygen sensor measurements of less than 10 ppm and usually under 1 ppm within the glovebox.

Whenever a powder was stored, the powder was placed in 20 mL glass scintillation vial with foil lined white plastic screw lid (RPI 121000, Research Products International Corp., Mt. Prospect, IL) with the ingot name, date of collection, milling time, speed, and any wet milling liquid used on the outside of the vial and on the lid with a permanent marker.

2.1.2.1 CGSR processing (Crushed, ground, sieved and reground)

Before processing a new ingot, the sieve, mortar and pestle were removed from the glovebox for cleaning. The tungsten carbide-lined (WC) mortar and pestle were rinsed out and scrubbed by hand with soapy water (New Day Hand Soap Item 34091, Triple S, Billerica, MA) and abrasive pad (Scotch-Brite General Purpose Hand Pad 7447, 3M, St. Paul, MN) until the liner of the mortar and pestle was shiny and no previously ground material could be seen or felt on the surface, generally 2 to 5 minutes. If any buildup was difficult to remove, a steel razor blade was used to remove it. After all visible buildup was removed, the WC mortar and pestle were rinsed with flowing tap water, then doused with acetone from a squeeze bottle sufficient to rinse all surfaces, and then given a final rinse with reverse osmosis water from a squeeze bottle sufficient to rinse all surfaces. The WC mortar and pestle were air dried before being returned to the glove box.

was

arce

dow

arce

Clar

and t

the n

Inc.,

the n

was p

ptess

morta

fragm

Valle

morta

down

Kimb

reside

pestle

mbute

shorter

The 100 g skutterudite ingot, approximately 40 mm in diameter and 10 mm thick, was brought inside the glove box while remaining sealed inside the glassy carbon crucible. A steel mallet, approximately 13 cm long and 2.5 cm in diameter, was wiped down with a KimWipe (Kimberly Clark 34155, Neenah, Wisconsin). To break the crucible and remove the ingot, the crucible was wrapped in a large KimWipe (Kimberly Clark 34256, Neenah, Wisconsin) and lightly tapped with the steel mallet until broken and the ingot removed. The ingot was placed inside the cleaned mortar and cracked with the mallet using a hydraulic press (Carver Hydraulic Unit Model Number 3912, Carver, Inc., Wabash, IN) inside the glove box. To crack the ingot, it was placed in the center of the mortar, then the mortar was set on the base of the hydraulic press. The steel mallet was placed between the top of the ingot and the upper plate of the hydraulic press. The press was pumped until a crack was heard and the ingot broken into several pieces. The mortar was placed on a large KimWipe to keep the glove box clean and collect errant fragments generated during crushing. The ingot was crushed by hand with the steel mallet to obtain particle sizes approximately 1 mm or less in diameter. The mechanical mortar and pestle machine (Retsch RM200, Retsch GmbH, Haan, Germany) was wiped down with KimWipes, especially the seal on the lid and the scraper, until a clean KimWipe remained white after wiping the surfaces. The mortar and pestle, with the crushed fragments from the ingot in the mortar, were placed in the mechanical mortar and pestle machine. The mechanical mortar and pestle ground the crushed ingot for 5 minutes with the pestle tightened to between 5 and 6.

Two sieves were used to sieve the ground powder, one marked for n-type skutterudite material and one for p-type skutterudite material. The ground powder was

placed in the appropriate 75 μm sieve (8" diameter x 2" height ASTM E 11 sieve, model 60.150.000075, Retsch GmbH, Haan, Germany) to collect the fine powder in a tray (Bottom collector pan, model 697203050, Retsch GmbH). The lid and seal of a shaker table (Retsch AS 200) were wiped down with KimWipes then the tray and sieve were placed on the shaker table. The shaker table was run at a setting of 50 for 5 minutes. The ground powder that remained on top of the 75 μm sieve was reground in the mortar and pestle for an additional 5 minutes. The regrinding process continued until all powders passed through the 75 μm sieve, which typically required a total of 3 to 5 grindings per 100 gram ingot. All the powder was placed in 20 mL glass scintillation vials with foil lined white plastic screw lid (RPI 121000, Research Products International Corp., Mt. Prospect, IL) and labeled with the ingot name, date of collection, and CGSR on the outside of the vial and on the lid with a permanent marker.

The crushed, ground, sieved and reground (CGSR) powders were then milled in a planetary ball milling using one of three methods: (i) dry milled only, (ii) first dry milled and then wet milled, or (iii) wet milled only. Billet SKD-18 was dry milled only. Billets SKD-Wet1, SKD-Wet2, and the first batch of SKD-Wet3 were dry milled and then wet milled. Billet SKD-Wet4 and batches 2, 3, and 4 of SKD-Wet3 were wet milled only (Appendix A). All dry and wet milling procedures were performed in a planetary ball mill (Retsch PM100) using a 500 mL stainless steel milling jar (Retsch 01.462.0228) . After each dry and wet milling run, the powders that adhered to the walls of the milling jar were removed by scraping with a 9 inch stainless steel spatula (VWR 57952-253, VWR LabShop, Batavia, IL). Also, at the completion of each milling run, a 1 to 2 gram powder sample was placed in a labeled vial for subsequent particle size analysis.

2.1.2.2 Dry milling

Each dry milling powder batch consisted of 23 to 25 grams of CGSR powder. The batch of powder was dry milled for 3 hours at 150 rpm in the planetary ball mill using approximately 230 grams of 10 mm diameter spherical 440C stainless steel media or 20 mm diameter spherical 420 stainless steel media, with the one exception of N-SKD-Min2 Batch 1 milled with tungsten carbide media (Appendix A). After the mill completed the 3 hour run, the powder and media were poured out into a sieve stack, consisting of a coarse sieve (8" diameter x 2" height ASTM E 11, model 60.150.000, Retsch GmbH, Haan, Germany) stacked on a catch basin (Bottom collector pan, model 697203050, Retsch GmbH). The jar was scraped down with the metal spatula to recover the powder caked on the sides and bottom until the sides and bottom of the jar looked shiny, with the recovered powder added to the sieve. The sieve was shook by hand for 1-2 minutes to remove caked powder from the media. The resulting powder was weighed in a plastic weigh boat (VWR 89106-764, VWR Labshop), a sample of 1-2 grams removed to a labeled glass scintillation vial. The remaining powder either placed in a second labeled scintillation vial or returned to the jar for the next milling step of wet milling, depending upon if the wet milling would be started immediately or at a later date.

2.1.2.3 Wet milling

Each wet milling batch was performed with the resulting powder from one CGSR plus dry milling batch or a new batch of CGSR powder (Appendix A). Batch sizes were 21 to 24 grams of dry milled powders or 23 to 24 grams of CGSR powder (Appendix A).

For powder that had previously been dry milled, the powders were milled with 25 mL of hexane (SKD-Min2) or ethanol (ETN-SKD-10 and JSpSKD-15, batch 1) for 6 hours (Appendix A). For CGSR powder, the powders were milled with 25 to 42 mL of ethanol for 6 or 9 hours. Batches 2 and 3 of JSpSKD-15, the first wet milled batches attempted, were milled with 25 mL of ethanol, batch 2 for 6 hours and batch 3 for 9 hours. All wet mill runs were processed at mill speeds of 110 rpm using 170 g of 6 mm diameter 440C stainless steel spheres and 230 g of 20 mm 420 stainless steel spheres, with the one exception of N-SKD-Min2 Batch 4 using 230 g of 20 mm spheres and 170 g of 3 mm 440C stainless steel spheres (Appendix A). The exception was a trial run to test using 3 mm spheres in place of 6 mm spheres as the media, with no noticed improvement noted. Once the wet milling was completed, the jar was opened, the coarse sieve placed on top upside down and the jar with the sieve on top were closed into the large argon filled ante chamber. A partial vacuum of approximately 50 kPa was pulled on the chamber, as measured on the needle gage on the chamber, and the vacuum was held for approximately 5 minutes to accelerate the evaporation of the hexane or ethanol. Following drying, the ante chamber was refilled with argon from the glove box to equalize the pressure between the ante chamber and glove box, the ante chamber opened to the glove box and the jar returned to the glove box, and the powder was recovered in a method identical to that used for dry milling.

2.1.3 Specimen fabrication by hot pressing

Several milling batches from a single ingot were combined to provide powder for a hot pressed specimen (Table 2.1). SKD-Wet1 consisted of powders from billet n-SKD-

Min2 wet milled batches 1, 2, 3, and 4. The dry milled and wet milled powders were hot pressed at 893K to 973K at pressures of about 75 MPa for 2 hours (Table 2.2). All hot pressing was performed by Edward Timm, Specialist, Mechanical Engineering Department, Michigan State University. A graphite die, 1.225 inches in diameter, was lined with grafoil to reduce sticking of the powder to the die. While in the glove box, the powder to be hot pressed was added to the grafoil-lined die (Table 2.1) and cold pressed by hand to hold together until the die was placed in the hot press machine.

The hot pressing cycle began with heating the die from room temperature to 523 K at 0 MPa pressure over 20 minutes, then to 773 K and 74.4 MPa of pressure over 20 minutes. While maintaining pressure, the temperature was raised to the maximum temperature (Table 2.2) over 10 minutes, then held for 120 minutes. After holding at the maximum temperature, the temperature was lowered to 100 K less than sintering temperature and pressure reduced to 0 MPa over 20 minutes. Finally the temp was reduced to a set temperature of 323 K over 120 minutes before allowing to cool to room temperature, but, in practice, cooling occured at a slower rate due to slow cooling rate. A typical cycle takes about 1 day to complete due to the speed of cooling to room temperature.

The hot pressed billet was removed from the die by Edward Timm and the grafoil lining removed from the billet.

Table 2.1 - Hot Pressed Billet Table. Each billet was pressed from multiple batches of powder, mixed together to create a puck of 7 mm thickness.

Ingot Label	Batches used in Hot Pressed Billet	Type	Billet Label
N-SKD-Min2	B1, B2, B3, B4	n-type 0.1 weight % Ce-doped	SKD-Wet1
ETN-SKD-10	B1, B2, B3	n-type, no Ce	SKD-Wet2
JSp-SKD-15	B1, B2, B3, B4	p-type	SKD-Wet3
JSn-SKD-14	B3, B4, some B2	n-type, no Ce	SKD-Wet4

Table 2.2 - Hot Pressing Parameters Table. Each billet was hot pressed to sinter the powders into a billet.

Billet Label	Composition	Mass of powder in die (g)	Type	Max Temp	Time at Temp (min)	Pressure (MPa)
SKD-Wet1	$Co_{0.95}Pd_{0.05}Te_{0.05}Sb_3$, doped with 0.1 atomic % Ce	31.0	n-type	923 K	120	74.4
SKD-Wet2	$Co_{0.95}Pd_{0.05}Te_{0.05}Sb_3$	42.0	n-type	923 K	120	74.4
SKD-Wet3	$Ce_{0.9}Fe_{3.5}Co_{0.5}Sb_{12}$	41.9	p-type	918 K	120	74.4
SKD-Wet4	$Co_{0.95}Pd_{0.05}Te_{0.05}Sb_3$	42.0	n-type	973 K	120	74.4

2.1.4 Dimensioning hot pressed billets

Specimens for subsequent mechanical property and microstructural analysis were cut from hot pressed billets using a K.O. Lee Surface Grinder (5361 SHS, K.O. Lee Co, Aberdeen, South Dakota) operated by Edward Timm. For the Resonant Ultrasound Spectroscopy analysis, rectangular parallelepiped specimens nominally 10 x 7 x 5 mm were cut from the hot pressed billets (Table 2.3). The specimen dimensions were calculated from the mean of 5 measurements per dimension at different locations on the specimen to an accuracy of $\pm$ 0.001 mm and resolution of $\pm$ 0.010 mm by electronic calipers (Mitutoyo CD-6"CSX, Kanagawa, Japan). The specimen mass was measured to $\pm$ 0.0003 gram accuracy using an electronic balance (Adventurer AR2140, Ohaus Corp, Pine Brook, NJ). Specimen mass densities were calculated from the mean specimen dimensions and specimen mass. Specimens used for microstructural analysis were mounted in thermoplastic and polished on an automatic polishing machine (Leco Vari/Pol VP-50, Leco Corporation, St. Joseph, MI) with successively smaller diamond grit paste from 90 μm to 1 μm. Each grit was used, starting at 90 μm, followed by 67 μm, 30 μm, 17 μm, 10 μm, 6 μm and 1 μm. Additional detail on the polishing procedure is given in Section 2.4.

Table 2.3 - RUS Specimen Dimensions and Mass. Each dimension was measured 5 times and the average of the three was taken.

Specimen Label	Dimension (mm)	Dimension (mm)	Dimension (mm)	Mass (g)	Density (g/cm^3)
SKD-Wet1A	9.978	6.912	5.16	2.6990	7.584
SKD-Wet1B	9.968	6.936	5.148	2.7013	7.590
SKD-Wet1C	9.952	6.936	5.162	2.7109	7.608
SKD-Wet1D	9.974	6.964	5.144	2.6980	7.551
SKD-Wet1E	9.978	6.924	5.142	2.6909	7.575
SKD-Wet1F	9.956	6.94	5.16	2.7065	7.591
SKD-Wet2A	10.03	6.688	5.03	2.5130	7.448
SKD-Wet2B	10.038	6.688	5.03	2.5140	7.445
SKD-Wet2C	10.03	6.74	5.026	2.5303	7.447
SKD-Wet2D	10.032	6.736	5.02	2.5313	7.462
SKD-Wet2E	10.022	6.696	5.024	2.5141	7.457
SKD-Wet2F	10.034	6.692	5.022	2.5176	7.466
SKD-Wet2G	10.04	6.722	5.026	2.5304	7.460
SKD-Wet2H	10.04	6.72	5.034	2.5283	7.444
SKD-Wet3G	9.986	6.598	4.984	2.4814	7.556
SKD-Wet3H	9.972	6.602	4.978	2.4851	7.583
SKD-Wet3I	9.962	6.558	4.986	2.4606	7.554
SKD-Wet3J	9.982	6.576	4.98	2.4721	7.562
SKD-Wet3K	9.972	6.618	4.976	2.4936	7.593
SKD-Wet3L	9.966	6.64	4.974	2.4984	7.590
SKD-Wet3M	9.984	6.612	4.98	2.4888	7.570
SKD-Wet3N	9.966	6.59	4.976	2.4689	7.555
SKD-Wet4A	9.968	6.92	4.99	2.4910	7.237
SKD-Wet4B	9.97	6.912	4.954	2.4845	7.278
SKD-Wet4C	9.962	6.95	4.98	2.5032	7.260
SKD-Wet4D	9.96	6.986	4.974	2.5192	7.279
SKD-Wet4E	9.962	6.938	4.99	2.4983	7.244
SKD-Wet4F	9.962	6.96	4.982	2.5059	7.254
SKD-Wet4G	9.96	6.97	4.98	2.5133	7.270
SKD-Wet4H	9.96	6.924	4.974	2.4982	7.283

2.1.5 Microstructural characterization

For microstructural characterization, specimen surfaces were either (i) polished or (ii) fractured and then examined with a scanning electron microscope (JEOL 6400, JEOL Ltd., Japan) operated by Jennifer Ni or Robert Schmidt using a working distance of 15 mm and an accelerating voltage of 15 kV. The specimen surfaces were sufficiently electrically conductive that no conductive coatings were applied prior to SEM examination. The as-polished specimen surfaces were examined to determine the size and shape of the surface pores and to determine whether or not surface-breaking cracks were present.

2.2 Room temperature Resonant Ultrasound Spectroscopy (RUS)

The Young's modulus, E, shear modulus, G, and Poisson's ratio, ν, were measured for the $Ce_{0.9}Fe_{3.5}Co_{0.5}Sb_{12}$ and $Co_{0.95}Pd_{0.05}Te_{0.05}Sb_3$ skutterudite materials using commercial Resonant Ultrasound Spectroscopy (RUS) equipment (Quasar RUSpec, Quasar International, Albuquerque, NM) [Migliori 1997, Ni 2010, Ren 2009]. If the specimen dimensions, mass and frequency response are known, the elastic moduli may be calculated [Migliori 1997, Ren 2009]. The RUS equipment measured the amplitude of the material response to a driving frequency, with each resonance detected as a peak in amplitude (Figure 2.1).

RUS specimens were cut from the hot pressed billet to nominal dimensions of 10 x 7 x 5 mm, and the mass and dimensions of each specimen were measured in the as-cut condition (Table 2.3, see section 2.1.4). The cut specimens were placed on a tripod arrangement of RUS transducers, with one driver transducer and two pickup transducers.

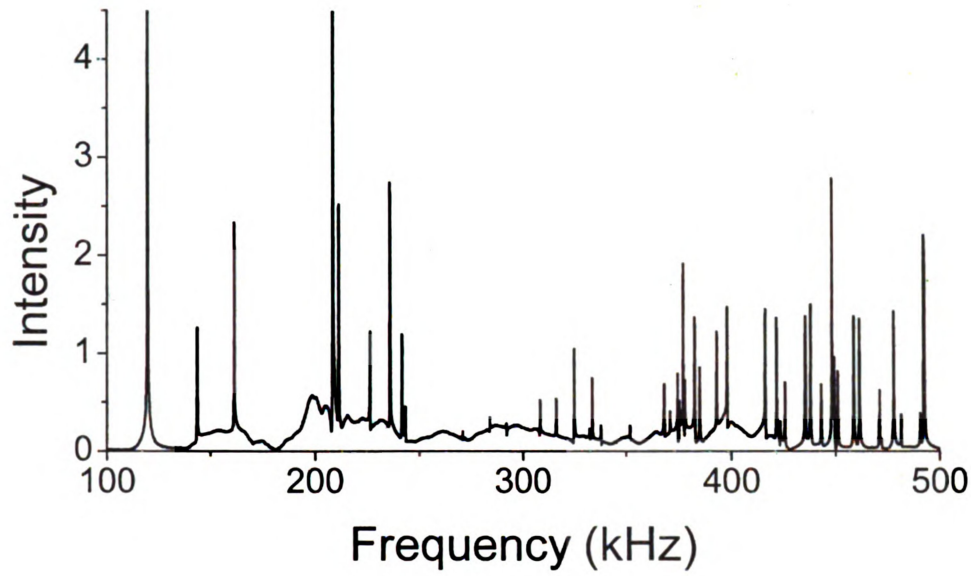

Figure 2.1 – A portion of a RUS spectrum from specimen SKD-Wet1A has 40 or more peaks between 20 and 700 kHz.

Table 2.4 – RUS Modulus Conditions Table. At least 14 resonance peaks were matched for every RUS analysis.

Billet Label	Type	Number of Resonance Peaks Matched
SKD-Wet1-A	n-type, doped with cerium	18
SKD-Wet1-B	n-type, doped with cerium	23
SKD-Wet1-C	n-type, doped with cerium	14
SKD-Wet1-D	n-type, doped with cerium	16
SKD-Wet1-E	n-type, doped with cerium	24
SKD-Wet1-F	n-type, doped with cerium	16
SKD-Wet2-A	n-type, no cerium	16
SKD-Wet2-B	n-type, no cerium	15
SKD-Wet2-C	n-type, no cerium	14
SKD-Wet2-D	n-type, no cerium	17
SKD-Wet2-E	n-type, no cerium	15
SKD-Wet2-F	n-type, no cerium	17
SKD-Wet2-G	n-type, no cerium	19
SKD-Wet2-H	n-type, no cerium	21
SKD-Wet3-G	p-type	21
SKD-Wet3-H	p-type	20
SKD-Wet3-I	p-type	16
SKD-Wet3-J	p-type	24
SKD-Wet3-K	p-type	24
SKD-Wet3-L	p-type	15
SKD-Wet3-M	p-type	21
SKD-Wet3-N	p-type	17
SKD-Wet4-A	n-type, no cerium	18
SKD-Wet4-B	n-type, no cerium	20
SKD-Wet4-C	n-type, no cerium	21
SKD-Wet4-D	n-type, no cerium	19
SKD-Wet4-E	n-type, no cerium	19
SKD-Wet4-F	n-type, no cerium	18
SKD-Wet4-G	n-type, no cerium	18
SKD-Wet4-H	n-type, no cerium	23

For the RUS measurements, the 10 x 7 mm specimen surface was placed on the transducers for greatest stability of the specimen on the transducers.

The mechanical resonance frequencies of each specimen were determined through a range of 20 kHz to 700 kHz, equally divided into 29,999 steps. The range was chosen to encompass at least the 55 lowest resonance frequencies for the specimens. At each step, the sinusoidal frequency was applied by the driving transducer to the specimen. Both pickup transducers detected the amplitude of the resonance within the specimen, and the measured resonance frequency spectra from both transducers was summed. A resonance frequency response was detected as a spike in the amplitude from either of the two pickup transducers (Figure 2.1). A frequency response may be attenuated at the pickup point for one of the transducers if the transducer was positioned on an anti-node of the standing wave [Ren 2009]. The sum of resonance frequencies from both transducers was used to maximize the detection of a resonance frequency [Ren 2009]. In addition, a separate baseline measurement was taken without a specimen on the transducers to show which peaks, if any, could be attributed to equipment noise. Resonance frequencies were determined by identifying the local maximum amplitude, while disregarding peaks that closely match peaks from the noise run.

At least two measurements of the resonance frequency response spectra were taken for each specimen. For each RUS measurement, the specimen was repositioned or turned over to the opposite face. For the room temperature response, the specimen always had the same set of resonant frequencies, but the amplitude detected by the pickup transducers may change when the specimen was repositioned [Ren 2009]. The

resonance frequency spectra measurement that could display the resonant frequencies with the sharpest definition was chosen for the analysis of the specimen's elastic moduli.

Based on the specimen dimensions, mass, and resonant frequency spectrum, the Young's modulus, shear modulus and Poisson's ratio were calculated using the software available on the RUS apparatus (Quasar Galaxy RI2000 and RPModel software, Quasar International). Between 14 and 24 resonance frequencies from the RUS spectra were used to calculate the modulus values for each specimen (Table 2.4). The Quasar Galaxy RI2000 and RPModel software required an initial guess for two modulus values, the Young's modulus and shear modulus, or the Young's modulus and Poisson's ratio, to iterate from and fit to the measured frequencies. Initial guesses of Young's modulus and Poisson's ratio were first taken from either (i) published values for similar antimony-based skutterudites [Ravi 2008, Recknagel 2007] or (ii) nanoindentation results measured at the Composite Materials Laboratory at Michigan State University. The RPModel software was iterated and frequencies from the RUS spectra fitted to the recalculated model until the RMS error of the fitted model was less than 0.10% while maximizing the number of fitted frequencies.

2.3 High Temperature Resonant Ultrasound Spectroscopy

High temperature Resonant Ultrasound Spectroscopy (RUS) was performed at the High Temperature Materials Laboratory at Oak Ridge National Laboratory during visits July 20-28 and October 5-9, 2009, under HTML user project number 2009-031, Elastic moduli and coefficient of thermal expansion for n- and p-type skutterudite thermoelectric materials, with Professor Eldon Case and Professor Jeffrey Sakamoto.

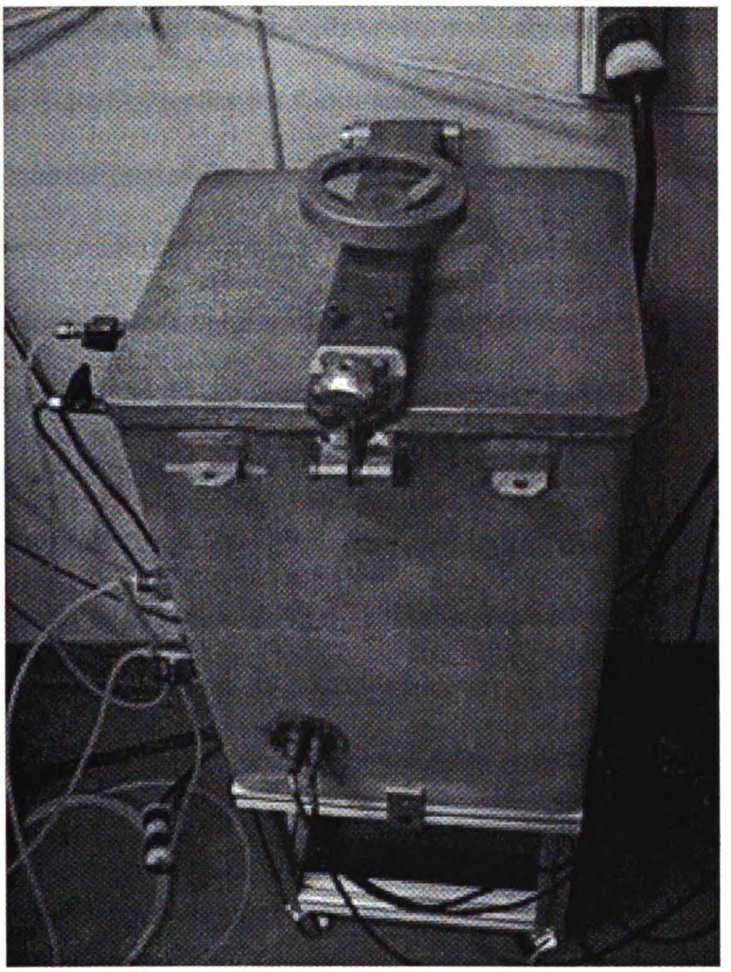

Figure 2.2 – The high temperature RUS equipment at the High Temperature Materials Laboratory in Oak Ridge National Laboratory, with a hot chamber of alumina refractories inside the chamber. Note the wires in the front to attach the RUS transducers. Four gas valves are on the left, one each for gas intake, oxygen sensor, roughing pump and bubbler. Not shown, the cable for the heater.

The equipment at Oak Ridge National Laboratories was similar to that used at Michigan State University for room temperature RUS measurement (Quasar RUSpec, Quasar International, Albuquerque, NM), with the addition of a custom built high temperature chamber (Figure 2.2) for the specimen. Inside, the chamber contained a heated region consisting of a tube-shaped alumina refractory of approximately 15 cm inside diameter and 20 cm outside diameter. The inside wall of the refractory contained resistance heating elements. On top of the tube, a removable set of three alumina bricks cover the top. Under the tube was a base of an alumina refractory with three rectangular cutouts arranged in a 3-point star. The cutouts allowed three probes to go through the base.

Below the heated chamber, three RUS transducers with high temperature probes were mounted in a tripod fashion. The high temperature transducers (custom part, Quasar International, Albuquerque, NM) were built with a high temperature probe, 3 mm in diameter, extending from the transducer approximately 15 cm, ending in a spherically rounded tip. Each probe end from the three transducers extended through the bottom refractory through one of the rectangular cutouts, and ended in the middle of the chamber, positioned to support a specimen on the tips of the three probes.

The temperature of the heated chamber was monitored using two thermocouples. The control thermocouple was sheathed in Inconel and inserted into the center of the chamber. The tip of the sheath was positioned approximately 1 cm away from the specimen. A second, unshielded thermocouple for overtemperature control was placed on the bottom of the high temperature chamber, approximately 3 cm below the control thermocouple.

Table
cycle
labels

| Speci
Label |
| --- |
| SKD- |
| SKD- |
| SKD- |
| SKD- |
| SKD- |

Table 2.5 – High temperature RUS cycle. Each high temperature RUS specimen was cycled from room temperature to a maximum temperature at 5 K/minute, with 10 minute holds for each RUS scan at the measurement temperature.

Specimen Label	Type	Maximum Temperature	Heating and Cooling Rate	Temperature Difference between Measurements
SKD-Wet1-A	n-type, doped with cerium	773 K	5 K/min	50 K
SKD-Wet2-A	n-type, no cerium	773 K	5 K/min	50 K
SKD-Wet3-G	p-type	773 K	5 K/min	50 K
SKD-Wet3-K	p-type	573 K	5 K/min	20 K
SKD-Wet4-A	n-type, no cerium	773 K	5 K/min	50 K

The entire apparatus was placed inside an aluminum chamber, approximately 50 cm wide, 30 cm deep, 80 cm tall, with a hinged lid and gasket seal. All electrical connections were made on the side of with custom built feed-throughs. Four ball valves were connected to the chamber, with one value each connected to (i) the fill gas, 96% argon and 4% hydrogen, (ii) the roughing vacuum pump, (iii) a bubbler, consisting of a pyrex vial filled part way with water and a tube extending below the surface of the water, and (iii) an oxygen sensor. The bubbler was used to reduce the back flow of air into the chamber. The oxygen sensor was not used because the gas used was 96% argon 4% hydrogen, and the sensor could not be used with the gas.

The sheathed thermocouple and the resistance heater were attached to a controller (UP550, Yokogawa Electric Corporation, Tokyo, Japan). The controller was programmed to ramp and hold the temperature of the chamber at a preassigned rate and time. Ramp rates of 5K per minute were used. An isothermal hold time of 10 minutes was used between ramp cycles. The over-temperature thermocouple was attached to an over-temperature controller (UT350, Yokogawa Electric Corporation, Tokyo, Japan) and the controller was set to cut power to the heater if the temperature exceeded 50 K more than the set temperature. During cooling, the cooling rate occurred at less than 5 K/minute below about 473 K, and the controller would not compensate for the slower time to reach the testing temperatures. To reach and hold the proper temperatures for testing, the program was manually controlled during cooling below about 473 K. The thermal cycle details (Table 2.5) are described in greater detail for each specimen below.

During setup of the high temperature RUS equipment, the RUS furnace chamber was open and a background RUS scan taken without a specimen on the RUS transducers.

This background RUS scan was used later during analysis to display resonance peaks inherent in the apparatus. The specimen was placed on the RUS transducers and RUS frequency spectra taken to verify the transducers were recording the specimen's resonance peaks.

After the specimen was placed on the RUS transducers, the chamber was prepared for thermal cycling. First, the hot zone with the specimen was covered with alumina refractory bricks. The chamber lid gasket was greased liberally and the chamber was closed. The roughing pump valve was opened and the pump run until the pressure gage read -600 torr. The roughing pump valve was closed, then the roughing pump was switched off and the RUS furnace chamber filled to atmospheric pressure with a reducing atmosphere, 96% argon and 4% hydrogen, from compressed gas tanks through a ¼ hose. Once the RUS furnace chamber was filled, the valve on the regulator mounted on the 96% argon-4% hydrogen tank was closed, and the roughing pump was used to again pump down the RUS furnace chamber to a vacuum gauge reading of -600 torr. A total of 3 pump down and refill (purge) cycles were done. Once the three purges were completed, the 96% argon 4% hydrogen gas line was fitted with an in-line rotameter (FL1442-S, Omega Engineering, Inc., Stamford, CT) and adjusted to give a constant gas flow rate of 75 to 100 cc per minute. Using the RUS equipment, a room temperature RUS scan was taken of the specimen to verify the specimen was properly positioned before starting the high temperature cycle.

Specimens SKD-Wet1-A, SKD-Wet2-A, SKD-Wet3-G, and SKD-Wet4-A were heated and cooled from 323 K to 773 K in 50 K increments at 5 K/minute, with a 10 minute isothermal hold time at each temperature, as measured by the sheathed

thermocouple. Specimen SKD-Wet3-K was heated from 333 K to 573 K in 20 K increments, with the same 10 minute isothermal hold and 5 K/minute rate of heating and cooling (Table 2.5). For each specimen, the RUS scan was taken after at least 5 minutes of isothermal hold. During cooling, temperatures below about 573 K cooled at a slower rate than 5 K/minute, and the scan was controlled manually, as the automatic control worked off of a timer instead of the temperature.

2.3.1 High Temperature RUS of SKD-Wet1-A

The first specimen scanned was SKD-Wet1-A on 21 July 2009. The room temperature resonance scan was at 294.8 K.

The specimen was cooled to the same set temperatures as heating, excluding 323 K. Resonance scans were taken by timer automatically until the temperature reached 373 K. Cooling to 373 K occurred at a slower rate than 5 K/minute, requiring a longer time and manual control.

Once the last scan was completed, the chamber heater was turned off, the gas was shut off, and the chamber allowed to cool to less than 333 K before opening. The specimen was removed from the chamber and visually inspected for any evidence of oxidation, chipping or cracking due to the thermal cycle. None was observed.

2.3.2 High Temperature RUS of SKD-Wet2-A

The second specimen scanned was SKD-Wet2-A on 23 July 2009. The room temperature resonance scan was at 295.1 K.

The specimen was cooled to 373 K for the last scan. Resonance scans were taken by timer automatically until the temperature reached 423 K. Cooling to 423 K occurred

at less than 2 K/minute, and required an additional 10 minutes before measurement. Cooling to and soaking at 373 K required 41 minutes before measurement.

Once completed, the heaters were turned off, the gas was shut off, and the chamber allowed to cool overnight. One final scan was taken the following morning at 295K before opening the chamber. The specimen was removed from the chamber and visually inspected for any evidence of oxidation, chipping or cracking due to the thermal cycle. None was observed.

2.3.3 High Temperature RUS of SKD-Wet3-G

The third specimen scanned was SKD-Wet3-G on 27 July 2009. The room temperature resonance scan was at 300.9 K. The reason for the elevated room temperature measurement was a previous specimen was removed after soaking overnight at 333 K and the equipment was still warm. Before the room temperature scan, the heater had been turned off for approximately 1 hour and the chamber had been pumped down and refilled 5 times.

Resonance scans were taken by timer automatically until the temperature was cooled to 473 K. Cooling to 473 K occurred at a slower rate than 5 K/minute, requiring a longer time and manual control. The specimen was reaching the 473 K temperature after approximately 15 minutes, providing insufficient time at the set temperature for the system to reach equilibrium. The scan at 423 K was taken 23 minutes after the previous scan, and the scan at 373 K was taken 114 minutes later, after an extended soak. The scan at 323 K was taken the following morning, 14 hours 5 minutes later, allowing the long time required for the specimen to cool.

Once completed, the heaters were turned off, the gas was shut off, and the chamber allowed to cool for approximately 30 minutes. The specimen was removed from the chamber and visually inspected for any evidence of oxidation, chipping or cracking due to the thermal cycle. A background scan was taken the following morning after the 50°C reading, at 41.4°C with the chamber opened and no specimen on the transducer probes. The specimen was noted to have a rust colored layer on the surface, but no change in dimensions or mass were measured. After heating to the maximum temperature, the RUS scans had broader peaks, and the RUS scans were unable to be analyzed.

2.3.4 High Temperature RUS of SKD-Wet4-A

The specimen SKD-Wet4-A was scanned on 6 October 2009. Prior to scanning, the dimensions were remeasured with the same calipers used previously at MSU. The room temperature resonance scan was at 294.9 K with the chamber in flowing argon nitrogen.

Resonance scans were taken by timer automatically until the temperature reached 423 K. The scan at 423 K was taken 31 minutes after the previous scan, and the scan at 373K was taken 56 minutes later.

Once the 373 K scan was completed, the heaters were turned off, the gas was shut off, and the chamber allowed to cool overnight. A resonance spectra scan was taken the following morning at 295.1K. The specimen was removed from the chamber and visually inspected for any evidence of oxidation, chipping or cracking due to the thermal

cycle. None was noted. The specimen dimensions were remeasured and no change in dimension was noted.

2.3.5 High Temperature RUS of SKD-Wet3-K

The specimen SKD-Wet3-K was scanned on 9 October 2009. Prior to scanning, the dimensions were remeasured with the same calipers used previously at MSU.

Resonance scans were taken by timer automatically until the temperature was cooled to 473K. The scan at 453K was taken 33 minutes after the previous scan, the scan at 433K was taken 33 minutes later, the scan at 413K was taken 17 minutes later, the scan at 393K was taken 17 minutes later, the scan at 373K was taken 20 minutes later, the scan at 353K was taken 27 minutes later, and the scan at 333K was taken 46 minutes later. Note that manual control resulted in greater soak time than automatic control on a few segments. This is due to interruptions in the lab and the nature of manual control. If the cooling rate was 5K/minute, the time between measurements would be 14 minutes, including isothermal hold time.

Once completed, the heaters were turned off, the gas was shut off, and the chamber allowed to cool for approximately one hour. The specimen was removed from the chamber and visually inspected for any evidence of oxidation, chipping or cracking due to the thermal cycle. A thin coating of rusty color was noted, but the surface was still shiny. The specimen dimensions were remeasured and the mass taken. No change in mass or dimension was noted.

2.4 Specimen Polishing

Prior to hardness testing or microstructure analysis, specimens were polished to a mirror finish to minimize surface defects. Specimens chosen for use were usually edge pieces from the cut billet or pieces with cracks or chips that precluded their use as full size specimens in RUS analysis. All specimen handling was done with stainless steel tweezers or while wearing gloves (Nitrile Purple Exam, Kimberly Clark, Roswell, GA).

The specimen to be mounted was first cleaned in approximately 20 mL of soapy water in a 50 mL Pyrex beaker, and placed in the ultrasonic cleaner (Ultramet III, Buehler, Evanston, IL) for at least 1 minute. The specimen was rinsed with RO water from a squeeze bottle by hand, ethanol from a squeeze bottle, and again with RO water before drying on a KimWipe. Rinsing was done until all specimen surfaces were contacted with a spray from the squeeze bottle, usually about 3 to 5 seconds per specimen per rinse.

Specimens were mounted in two ways. Specimens to be permanently mounted were set in epoxy (Epoxicure Resin and Epoxicure Hardener, Buehler, Evanston, IL). Specimens that may be removed from mounting were mounted to a 1" diameter x 1" aluminum stub by thermoplastic (Lakeside 70, Buehler, Evanston, IL).

Epoxy mounted specimens were set inside a 1" outside diameter phenolic ring cut to 1" length (Black Bakelite Ring Forms #811-221, Leco, St Joseph, MI). To mount the specimens, epoxy was poured in a disposable medicine cup and measured on an electronic balance (Adventurer AR2140, Ohaus Corp, Pine Brook, NJ). Hardener was added into the medicine cup while on the balance by hand with a syringe until the manufacturer specified proper mass ratio was reached. The epoxy was mixed by hand

with a wooden stir stick until swirl lines disappeared, approximately 1 minute. An aluminum plate was sprayed with mold release (3470 Reliable Release, Crown, Woodstock, IL) and the specimens were placed on the plate. A phenolic ring was placed around each specimen and the ring was filled with epoxy to approximately ¾ full. A steel weight, approximately 5 cm x 5 cm x 3 cm, was placed on top of the phenolic ring to hold the ring from floating up and the epoxy from flowing out underneath the ring before curing. The specimens were left to cure for a minimum of one day, then engraved with specimen names using a rotary tool on both the side and top. Any epoxy that leaked under the phenolic ring was cut off with a steel razor.

Thermoplastic mounted specimens were mounted on aluminum stubs, 1" in diameter and 1" in length. The stubs were placed on a hot plate (Stirrer/Hot Plate Model 4658, Cole-Palmer, Chicago, IL) to warm up with the heater at about setting 6. An amount of thermoplastic (Lakeside 70, Buehler, Evanston, IL) equal to about ½ the volume of the specimen was placed on top of the stub to soften. After the thermoplastic softened to roughly chewing gum consistency, the specimen was placed on the thermoplastic with tweezers, and the specimen allowed to heat up with the thermoplastic. The thermoplastic was placed around all four sides of the specimen, supporting more than half of each side. If the thermoplastic was not supporting the sides of the specimen, additional thermoplastic was added to secure the specimen. Once mounted, the mounted specimen was removed from the hot plate and allowed to cool to room temperature on the bench. After cooling, the aluminum stub was labeled with the specimen name with a permanent marker on both the side and bottom.

Specimens were polished using a Leco automated polishing wheel (Leco Vari/Pol VP-50, Leco Corporation, St. Joseph, MI). Between 3 and 6 specimens were polished at a time. The specimens were mounted in a 12-position specimen holder and adjusted to make the surface to be polished as level and coplanar as possible by hand, then secured by a set screw. The specimens were polished with a series of diamond compounds, each run on a dedicated polishing wheel (Table 2.6). Affixed to each of the polishing wheels was a WhiteTec polishing pad (White Tec #812-454, Leco, St. Joseph, MI) or, for the 1 μm and 0.5 μm diamond grits, a red felt polishing pad (Red Tec #812-445, Leco, St. Joseph, MI). If the polishing pad became contaminated as observed by inordinately large scratches on the specimens, the specimen wheel was washed and the polishing pad replaced.

The polishing wheel was placed on the machine and a spiral pattern of dots of diamond compound applied by syringe were distributed around the polishing pad, spaced between 1 and 2 cm apart and approximately 0.3 mm high. Diamond compound extender (Microid Diamond Compound Extender #811-004, Leco, St. Joseph, MI) was added by squeeze bottle to wet the surface of the polishing pad. The mounted specimens were placed on the polishing machine and the machine's drive mechanism attached, then the machine was set to run a 30 minute cycle. Diamond compound extender was reapplied as required to maintain a wet surface on the polishing pad. After each 30 minute cycle, the specimens were examined for polishing progress and possible scratches from contamination. If the specimens were sufficiently polished to the extent possible for the diamond grit being used, the specimens were washed and the polishing pad patted dry with paper towels before changing the polishing wheel to the next wheel to be used. If

Table 2.6 – Diamond Polish Table. Each diamond grit was used in succession to polish a specimen until reaching the desired polished surface on the specimen. The last polish used was either the 1 μm or 0.5 μm polishing grit compound.

Nominal Diamond Grit Size	Diamond Grit Size Range	Manufacturer	Part Number
90 μm	80-100 μm	Warren Superabrasives, Anaheim, CA	80-100MB MUS 20gm
67 μm	54-80 μm	Warren Superabrasives, Anaheim, CA	54-80MB MUS 20gm
35 μm	Not listed	Warren Diamond Powder Company, Olyphant, PA	#35 MUS MB 20G
15 μm	Not listed	Warren Diamond Powder Company, Olyphant, PA	#15 MUS MB 20G
9 μm	Not listed	Leco Corporation, St. Joseph, MI	810-913
6 μm	Not listed	Warren Diamond Powder Company, Olyphant, PA	#6 MUS MB 20G
1 μm	Not listed	Leco Corporation, St. Joseph, MI	810-870
0.5 μm	Not listed	Leco Corporation, St. Joseph, MI	810-868

the specimens required additional polishing, the process was repeated with the next smaller grit size of diamond compound and appropriate polishing wheel.

The first polishing cycles were run with the 90 μm wheel and diamond grit compound (80-100MB MUS 20gm, Warren Abrasives, Anaheim, CA). The first cycles were intended to level all the specimens out on the polishing wheel, so all the specimens had a complete surface in contact with the polishing wheel. Every specimen must have the surface to be polished fully exposed, not covered by a layer of epoxy, and show evidence of contact with the polishing wheel before changing to a smaller grit diamond compound and polishing wheel. The amount of time required varied greatly based on the angle and height differences between specimens in the specimen holder, from 15 minutes to over 3 hours. Once completed, the specimens were washed, the polishing pad and wheel were patted down with paper towels to dry, and the wheel was returned to the appropriate storage drawer. If more than 120 minutes were required, the specimens were rinsed under running water for 2 minutes per specimen after the last cycle, the polishing pad was patted dry with paper towels, and the diamond grit compound was reapplied to the wheel.

Washing the specimens consisted of repeated rinsing and examination. First, the entire wheel with specimens mounted was rinsed under running tap water to examine the specimens, then rinsing out any bubbles, craters or other catchpoints for diamond compound or contamination, using a wooden toothpick if necessary to get out diamond grit. Each specimen then received a drop of soap (Estesol Gold, Stockhausen Inc., Greensboro, NC) and was set under running tap water for 3 minutes per specimen and examined again to verify no visible contamination remained. Finally the specimens were

rinsed an additional 3 minutes under running tap water to remove any remaining residue of soap or diamond compound.

Each polishing cycle worked on successively smaller diamond grits on different polishing wheels (Table 2.6). For specimens mounted in epoxy, every diamond grit was used, generally for 2 to 4 cycles of 30 minutes each. For specimens mounted on aluminum stubs with thermoplastic, every other diamond grit compound may be skipped between 90 μms and 6 μms. Without the epoxy contacting the polishing wheel, the specimens polish away more rapidly. The rapid polishing of thermoplastic mounted specimens created a risk of removing too much material from the specimen for later testing purposes. Skipping diamond grits reduced the amount of specimen material that would be polished away while also attaining a proper final polish in less time.

2.5 Hardness Measurement

Hardness measurements were measured on polished specimens, taken down to 1 μm diamond compound for microindentation, and to 0.5 μm for nanoindentation.

For nanoindentation, the specimens were loaded into a custom aluminum specimen holder designed to hold 6 mounted specimens, along with a 6061 aluminum standard. Each specimen was arranged to run automatically using the manufacturer supplied software (MTS, Oak Ridge, TN), with the aluminum run first for verification and cleaning of the indenter tip. Using a Nanoindenter XP with CSM/LFM (MTS, Oak Ridge, TN) with a Berkovich indenter tip, between 16 and 22 indentations per specimen were indented. The aluminum standard was indented in a square 4 x 4 pattern of indentations spaced 50 nm apart to a depth of 2000 nm, followed by indentation of each

of the specimens in the same 4 x 4 pattern as well as an additional set of manually chosen locations to increase the sample size. When setting up the indentation pattern, an area on the specimen surface clear of scratches or other surface defects was chosen for indentation, as observed through the optical microscope camera on the machine. The machine was only run during the night, beginning after 5 pm when building vibrations are at a minimum. Results were examined for major outliers, caused by indenting near a flaw such as a crack or pore, vibrations or other reasons, and outliers would be disregarded. Outliers would have hardness measurements more than 5 times different from the typical measurement for the specimen.

Vickers indentations were performed with a Buehler microindenter (Buehler Semimacro Indenter, Lake Bluff, IL) and a Shimadzu hardness tester (Shimadzu HMV-2000, Kyoto, Japan). Each of the indenter machines were calibrated with a steel standard of 7.90 hV (761-048, Yamamoto Scientific Tools Lab, Co LTD, Japan). A correction factor was multiplied by the hardness value measured by indening the standard to equal the value of the standard.

Indentations with the Buehler were performed on specimens polished with at least a 1 μm diamond paste. The machine was turned on and the filars were zeroed by adjusting them together in the middle of the viewing area until the inside edge of the filars just touched. Only the middle 1/3 of the filars was used for both calibration and measurement to avoid any inaccuracies near the end of the optics and filars. Once zeroed, the filars were moved away from center, then repositioned at zero and the measurement was verified to be at 0 ± 0.1 μm. The mounted specimen was placed on the specimen stage and the microscope focused. The desired weight was set, the loading

speed and time adjusted, and a clear spot on the specimen surface chosen. Indentations were made in the specimen with a minimum of 500 μm separation between indentations and 1000 μm from any edge of the specimen. If any scratches or surface defects were seen in the place where an indentation would occur, a new location was chosen.

The Buehler indenter had a replacement 20X objective lens (MPlan 20, N.A. 0.40, 408753, Olympus, Tokyo, Japan) that was a shorter length than the indenter tip. Both the indenter tip and objective lens were mounted to a rotating turret. Due to the difference in height between the indenter tip and the objective lens, the specimen stage was lowered ¼ turn before the indenter was rotated into position above the specimen. Once the indenter was rotated into position, the indentation was applied automatically by pressing the "start" button. Once completed, the objective lens was rotated back into position, the specimen raised ¼ turn, and the focus readjusted. The filars were used to measure across both diagonals of the indentation and recorded on a paper worksheet.

The first 5 indentations were examined for damage that would make an accurate measurement impossible, due to excessive chipping around the edges of the indentation obscuring the corners of the indentation. If less than 3 of the first 5 indents were usable, the indentations on the specimen were suspended at the given speed and load. Otherwise, at least 20 indentations were made per specimen, with a goal of at least 20 usable indents per specimen per load. Once all the indentations were taken, the measurements were transferred to an Excel spreadsheet for computation and the paper retained as a backup in a binder in the lab.

Indentations by the Shimadzu hardness tester were performed similarly to the Buehler, with some variations due to differences in the machine. After the machine was

turned on, the filars were zeroed by centering a thin line above the right filar between two lines above the left filar and pressing the "clear" button. Then the machine load (25 grams to 1000 grams), load time (5 to 10 seconds), indentation surface (flat), measurement type (Vickers hardness), number of measurements per indentation (2), and number of indentations (1) were set using the keypad and following the screen menus.

The specimen was placed on the stage and focused under the 50X objective lens. The specimen was positioned for the indentation, with a minimum 1000 μm from any specimen edge and a minimum 500 μm from another indentation. The turret was rotated to the indenter and the "start" button pressed. Once the indentation was completed, the turret was rotated back to the 50X objective lens and the indentation diagonals were measured with the filars. The diagonal measurements were recorded from the screen on a paper worksheet and the specimen was moved for the next indentation. Out of the first 5 indentations, if the majority of indents were unreadable, the indentations were ceased at the load and time used. A total of at least 20 indentations were made, with at least 20 measured indentations intended as the goal. The resulting measurements were transferred from the paper worksheet to an Excel spreadsheet for computations and the paper worksheet placed in a 3-ring binder inside the lab for backup.

Each pair of indentation diagonal measurements were averaged and the hardness computed by the equation,

$$HV = \frac{1.8544 * m * g}{d^2} \qquad \text{(Equation 2.1)}$$

where HV is the Vickers hardness in Pascals, m is the mass of the load in kilograms, g is the gravitational constant in meters per second, and d is the average diagonal

measurement of the indentation [Wachtman 1996]. The factor 1.8544 was used to convert the projected area of the Vickers indent to the actual area of the 3D indentation, based on the geometry of the Vickers indenter [Wachtman 1996]. The resulting hardness value was multiplied by the correction factor previously obtained by indentation of the steel standard. The corrected hardness values from a set of indentations were averaged and the standard deviation calculated.

2.6 Thermal Expansion Measurements

Thermal expansion was measured on bulk specimens in the High Temperature Materials Laboratory at Oak Ridge National Laboratories. Using a Thermomechanical Analyser (TMA) (Q400, TA Instruments, New Castle, DE), the specimens were measured for thermal expansion. The machine was calibrated with standard weights following the software instructions by Rosa Trejo before use for a week, and recalibrated after any change in machine components. The glass sample tray and probe were wiped down with KimWipes dampened with ethanol before zeroing the length measurement and loading a specimen. The specimen was positioned with the 10 mm nominal dimension vertical for measurement, using the 3 mm diameter glass expansion probe centered on top of the specimen. A constant 0.1 N force was applied and maintained throughout testing. The chamber was flushed with 50 mL/min of 96% Argon 4% Hydrogen gas from a compressed gas cylinder. Although the gas stream was maintained throughout to limit oxidation, the chamber is not sealed and cannot be evacuated of air. To limit the amount of oxygen, the first step of the thermal cycle was a 1 hour isothermal hold with the specimen at room temperature to purge out as much air as reasonably possible.

2.6.1 TMA Measurement of SKD-Wet1-B

Thermal expansion was measured on SKD-Wet1-B on 21 July 2009 with a cycle from room temperature to 773 K and back, repeated for 5 total cycles, at a heating and cooling rate of 3 K/minute, with a 60 minute hold before the first cycle to flush the chamber, and a constant force of 0.1 N on the specimen throughout cycling.

The cycle resulted in some hysteresis detailed in the results section, a result requiring additional investigation. While checking the machine for possible causes of hysteresis, the glass probe was broken. Later runs were performed with a new probe of the same type, installed and tested by the manufacturer technician.

2.6.2 TMA Measurement of SKD-Wet2-B

Thermal expansion was measured on SKD-Wet2-B on 6 October with a cycle from room temperature to 773 K and back, repeated for 2 total cycles, at a heating and cooling rate of 1.5 K/minute, with a constant force of 0.1 N on the specimen throughout cycling. The specimen had been scheduled to run for more cycles, but the cycling was stopped after 2 cycles due to a change in specimen dimensions at high temperatures. The specimen showed a permanent growth in dimension most evident above 673K, indicative of a nonreversible process.

2.6.3 TMA Measurement of SKD-Wet4-B

Thermal expansion was measured on SKD-Wet4-B on 8 October 2009 with a cycle from room temperature to 573K and back, repeated for 4 total cycles, at a heating and cooling rate of 1.5K/minute, with a constant force of 0.1N on the specimen throughout cycling.

2.6.4 TMA Measurement of SKD-Wet3-J

Thermal expansion was measured on SKD-Wet3-J on 7 October 2009 with a cycle from room temperature to 573K and back, repeated for 3 total cycles, at a heating and cooling rate of 1.5K/minute, with a 60 minute hold before the first cycle to flush the chamber, and a constant force of 0.1N on the specimen throughout cycling.

2.7 XRD Examination

2.7.1 XRD Examination of SKD-Wet3 powder

X-ray diffraction (XRD) measurements of the SKD-Wet3 powder were performed on 5 October 2009 by Andrew Payzant and Roberta Peascoe-Meisner in the High Temperature Materials Laboratory at Oak Ridge National Laboratory. The measurements were performed using a PANanlytical X'pert Pro (PANalytical PW3040-PRO, Serial #DY1331, PANalytical B. V., Almeno, Netherlands) with the powder in a temperature stage (Anton Paar XRK900 Reaction chamber, Anton Paar GmbH, Graz, Austria). The sample, JSpSKD-15-Dry-B1, was dry milled powder from the ingot that later was hot pressed into SKD-Wet3. The dry milled powder was chosen over the wet milled powder because it had not shown signs of spontaneous combustion, as the wet milled powder had previously done (see section 2.8, section 3.5).

The step size for 2θ was 0.001° through a range of 15° to 40° 2θ, and an X-ray source with a copper anode (PW3373/10 Cu LFF DK184043, PANalytical B. V., Almeno, Netherlands). The diffraction pattern was measured between 303K and 633K at 30K increments.

2.7.2 XRD Examination of SKD-Wet1 and SKD-Wet2 powder

X-ray diffraction measurements of the SKD-Wet1 and SKD-Wet 2 powder were performed 28 April 2010 by Richard Staples, Chemistry Department, Michigan State University. The patterns were obtained on a Rigaku Rotaflex 200B diffractometer equipped with Cu Kα X-ray radiation and a curved crystal graphite monochromator (Rigaku Corp., Tokyo, Japan), operating at 45 kV and 100 mA. A graphite filter and a series of slits were used (DS 0.5mm, SS 0.5 mm, RS 0.0.3 mm, RSm 0.45mm detector). Intensity was measured by counting with a NaI Scintillation detector every 0.02° 2θ and a rate of 1° 2θ per minute, and measured through a range of 10 to 90° 2θ. Each sample was packed into a rectangular well on a fused silica slide, with a layer of grease applied by finger to hold the sample powder from falling when positioned vertically in the machine fixture.

2.8 Particle Size Analysis

Particle size analysis was done on each batch of milled specimens until safety concerns arose, with all action suspended when powders of each type ignited during handling when exposed to air at room temperature. The second batch of p-type powder to be examined ignited while being removed from a sample vial of wet milled powder. Due to the incident, only one powder batch of the p-type skutterudite was analyzed. The first specimen of n-type powder from JSnSKD-14 (later hot pressed to SKD-Wet4) that had been wet milled also ignited, suspending n-type particle size analysis as well. Previously, wet milled n-type powder had been examined without incident for the powders pressed into SKD-Wet1 and SKD-Wet2. The conditions for particle size

analysis reported in this thesis are for the powders analyzed prior to the powder autoignition incidents.

Prior to particle size analysis, approximately 0.2 g of the sample powder was suspended in a solution of 50% sucrose (Mallinckrodt Baker, Phillipsburg, NJ) and degassed DI water, and 0.1% of a surfactant added (see section 3.2). The solution was analyzed in a laser particle analyzer (Saturn DigiSizer 5200, Micromeritics Instrument Corporation, Norcross, GA) per the manufacturers instructions. The process was run by Jennifer Ni, Graduate Student, Materials Science Engineering, Michigan State University, or Kristen Khabir, Undergraduate Student, Materials Science Engineering, Michigan State University, according to the process recommended in the manufacturer's manual. A total of 8 scans were averaged for each sample analyzed.

2.9 Grain Size Analysis

Grain size analysis was performed on specimens from each wet mill billet and from JSn-SKD-18. Grain size analysis was performed by two methods; the first method used polished specimens that were thermally etched, and the second method used fractured surface for grain size analysis.

Prior to grain size analysis, the specimens were polished with a final polishing compound of 0.5 μm diamond grit. Each polished specimen was examined by SEM for porosity and cracks, and examination of the size of surface scratches. After thermal etching or fracture, the specimens were examined again for grain size analysis by SEM. For SEM examination, the specimen was affixed to an aluminum stub by carbon tape, then examined with the JEOL 6400 SEM at the Center for Advanced Microscopy,

Michigan State University, operated by Jennifer Ni, Graduate Student, Materials Science Engineering, Michigan State University. All images were taken at a working distance of 15 mm and an accelerating voltage of 15 kV. The images were taken at magnifications of between 2000x and 10000x. The image was digitized at a resolution of 2048 x 1536.

2.9.1 Grain size analysis by Thermal Etch

The thermal etch process was based on a successful method used by Professor Sakamoto of Michigan State University on a similar skutterudite specimen. Professor Sakamoto's specimen was taken to 873K at 5 K/min and held at temperature for 120 minutes, then cooled at a maximum of 5 K/min back to room temperature. The specimens for this study were cycled in either a vacuum or flowing argon environment, and run in either the muffle tube furnace or Minimite furnace.

The first thermal etch was run in a muffle tube furnace (CTF 12/75/120, Carbolite, Derbyshire, UK) with flowing argon atmosphere. The muffle tube assembly was unused before the first run, and labeled n-SKD for future uncontaminated use with only the same type of material. The end seal used all stainless steel fittings with Teflon tape on the threaded connections, and a polyurethane rubber seal with vacuum grease. The tube was pumped down for approximately 2 minutes with a roughing pump and refilled with argon to atmospheric pressure three times before beginning the heating cycle. The muffle tube was approximately 40 inches long, and the specimen to be heat treated was put within 2 inches of the center by use of a yard stick. The run was unsuccessful and the muffle tube furnace was only used for the first thermal etch attempt.

The subsequent thermal etches were cycled in a 1" outside diameter glassy silica ampoule (custom, Michigan State Glass Shop, East Lansing, MI) in a Minimite (Lindberg Blue M Minimite, Thermo Scientific, Waltham, MA) furnace. The switch from the muffle tube furnace was made to create a cold trap with approximately half of the ampoule outside the furnace in room temperature air. The intent was to make a cool area to attract condensate away from the specimen, and avoid a potential cause of difficulty with the initial thermal etch run.

The washed and polished specimen was placed in the silica ampoule, a vacuum applied by a roughing pump and torch sealed by Edward Timm, Specialist, Mechanical Engineering Department, Michigan State University. Approximately 6 cm of ampoule was inside the furnace and 6 cm outside the furnace. The specimen was near the end of the ampoule and the center of the furnace. The opposite end of the furnace was insulated with a 3 cm x 6 cm piece of Kaowool insulation (Kaowool ceramic fiber 16 lb blanket, Babcock and Wilcox, Lynchburg, VA).

The furnace was set to ramp to 873 K at 5 K/minute, hold for between 1.5 hours and 4 hours, then cool at 5 K/minute to room temperature. The furnace was run overnight to allow enough time for the furnace and ampoule to cool before handling. Once cooled, the ampoule was covered with at least two layers of paper towel and broken with a tap from a hammer on the opposite side of the ampoule from the specimen.

Following thermal etch, the specimens were mounted on aluminum stubs for SEM analysis. The SEM image was evaluated according to the line intercept method of ASTM E-112. Grain boundary intercepts were counted, and between 200 and 300 intercepts

were measured per micrograph on lines in random orientation. The length of the lines were measured and scaled by the scale bar imprinted on the image.

2.9.2 Grain size analysis by Fracture Surface

To examine by fracture surface, the specimen was fractured in a controlled manner. The specimen was mounted on a glass slide with thermoplastic (Lakeside 70, Buehler, Evanston, IL). The method used to mount the specimen to the slide was identical to that used to mount a specimen to an aluminum stub (section 2.4) except a glass slide was used in place of the aluminum stub, then the slide was labeled with the specimen label using a permanent marker.

The specimen was scored by low speed diamond blade saw (Isomet Low Speed Saw, Buehler, Evanston, IL) while mounted. The mounted specimen was scored between 1/3 and 2/3 through on the low speed saw at speed setting of between 3 and 4. The scored specimen was removed from the slide by softening on the hot plate, then scraping off the softened thermoplastic with a razor blade and tweezers. The residue was removed with repeated application of ethanol and wiping with KimWipes until no residue of thermoplastic was visible on the KimWipe. Once all evidence of the thermoplastic was gone by visual inspection, the specimen was given a final rinse of ethanol, followed by a rinse of reverse osmosis water.

The scored and rinsed specimen was fractured along the scored surface by inserting a screwdriver as a wedge. The fractured specimen was examined by SEM. A printout of the SEM micrograph was made to fill an 8-1/2 x 11 sheet of paper. The SEM micrograph print was evaluated according to the line intercept method of ASTM E-112.

The method used a set of about 10-30 straight lines drawn in random orientations across the micrograph. Each grain boundary a line crossed was counted, and sufficient lines were drawn to include between 200 and 300 grain boundary intercepts. The total length of the lines were measured and scaled by measuring the scale bar imprinted on the image. The scaled line length was divided by the number of intercept to produce an average length of line between grain boundary intercepts. The average line length was multiplied by a stereographic projection factor.

3 Results

3.1 Particle size analysis

Particle size analysis was performed only until it was discovered that the skutterudite powder exhibited potentially dangerous pyrophoric behavior. Prior to autoignition of two samples when exposed to air, a sample from each of the dry milled only and the dry/wet milled powder batches was analyzed by the Saturn Digisizer.

The analysis fluid for all particle size analysis on the Saturn Digisizer (except for one test) was a 50% by weight sucrose / deionized water solution with 0.1% sodium pyrophosphate added as a dispersant. For each run, approximately 0.2 g of the milled skutterudite powder was dispersed in the Saturn Digisizer analysis fluid. One particle size analysis run used 0.1% sodium lignosulfonate as the analysis fluid with all of the other Saturn Digisizer parameters identical to the other particle size analysis runs for milled skutterudite. The dispersant test revealed sodium pyrophosphate dispersed the skutterudite powder more effectively than sodium lignosulfonate, thus the sodium lignosulfonate dispersant was not used beyond the single test.

The powder particle analysis was performed for all n-type powder batches from which specimens SKD-Wet1 and SKD-Wet2 except one SKD-Wet2 powder batch (Tables 3.1 and 3.2). Of the p-type powder, only one batch of the wet milled from ingot JSp-SKD15 batch 2 underwent powder particle analysis.

The powder particle size distribution for Min2-SKD (Figure 3.1) includes distinct modes at approximately 2 μm and 20 μm. The Min2-SKD powder was later used to hot press specimen SKD-Wet1. After wet milling, two modes remained in the powder

Table 3.1 - Particle size analysis of the cerium doped n-type skutterudite powder, $Co_{0.95}Pd_{0.05}Te_{0.05}Sb_3$, doped with 0.1 atomic % Ce, nSKD-Min2. Particle sizing was measured by laser scattering with the Saturn Digisizer in a suspension of 50% by weight sucrose/ deionized water solution with 0.1% sodium pyrophosphate as a dispering liquid.

Specimen Name	Type	Wet or Dry Milled	Batch Number	Test Number	Median Particle Size (μm)	Mean Particle Size (μm)
nSKD-Min2	Ce-doped n-type	Dry	2	1	4.7	8.9
nSKD-Min2	Ce-doped n-type	Dry	2	2	4.3	8.8
nSKD-Min2	Ce-doped n-type	Dry	3	1	3.5	9.0
nSKD-Min2	Ce-doped n-type	Dry	3	2	3.4	7.8
nSKD-Min2	Ce-doped n-type	Dry	4	1	2.6	5.6
nSKD-Min2	Ce-doped n-type	Wet	1	1	2.4	5.0
nSKD-Min2	Ce-doped n-type	Wet	2	1	2.7	5.1
nSKD-Min2	Ce-doped n-type	Wet	2	2	2.7	5.0
nSKD-Min2	Ce-doped n-type	Wet	3	1	2.6	5.0
nSKD-Min2	Ce-doped n-type	Wet	3	2	2.4	3.7
nSKD-Min2	Ce-doped n-type	Wet	3	3	1.9	3.1
nSKD-Min2	Ce-doped n-type	Wet	4	1	2.0	4.1
nSKD-Min2	Ce-doped n-type	Wet	4	2	1.9	3.6

Table
Co
with
solut

*For
disp
any o

| Spec
Nam |
|---|
| EN |
| EN |
| EN |
| EN |
| EN |
| EN |
| EN |
| EN |
| EN |
| EN |
| EN |
| EN |
| EN |
| SK |
| EN |
| EN |
| EN |
| EN |
| EN |
| EN |
| EN |
| EN |
| EN |
| EN |
| EN |
| EN |
| EN |
| EN |

Table 3.2 - Particle size analysis of non-cerium doped n-type skutterudite powder, $Co_{0.95}Pd_{0.05}Te_{0.05}Sb_3$, ETN-SKD10. Particle sizing was measured by laser scattering with the Saturn Digisizer in a suspension of 50% by weight sucrose/ deionized water solution with 0.1% sodium pyrophosphate as a dispering liquid*.

*For ETN-SKD10 Wet, Batch 1 Test 1, 0.1% sodium lignosulfonate was used as the dispersing liquid as a test. Due to agglomeration concerns, this liquid was not used on any other test.

Specimen Name	Type	Wet or Dry Milled	Batch Number	Test Number	Median Particle Size (μm)	Mean Particle Size (μm)
ETN-SKD10	n-type	Dry	1	1	2.9	6.3
ETN-SKD10	n-type	Dry	1	2	3.0	7.6
ETN-SKD10	n-type	Dry	1	3	2.9	6.7
ETN-SKD10	n-type	Dry	2	1	2.4	4.0
ETN-SKD10	n-type	Dry	2	2	2.5	4.4
ETN-SKD10	n-type	Dry	3	1	2.8	4.9
ETN-SKD10	n-type	Dry	3	2	3.6	8.0
ETN-SKD10	n-type	Dry	3	3	3.5	7.8
ETN-SKD10	n-type	Dry	4	1	3.1	8.1
ETN-SKD10	n-type	Dry	4	2	2.6	5.1
ETN-SKD10	n-type	Dry	4	3	2.1	3.6
ETN-SKD10*	n-type	Wet	1	1	2.1	3.8
ETN-SKD10	n-type	Wet	1	2	1.8	2.5
ETN-SKD10	n-type	Wet	1	3	1.9	2.6
ETN-SKD10	n-type	Wet	2	1	3.2	3.4
ETN-SKD10	n-type	Wet	2	2	2.7	3.1
ETN-SKD10	n-type	Wet	2	3	1.8	3.1
ETN-SKD10	n-type	Wet	2	4	2.0	3.9
ETN-SKD10	n-type	Wet	2	5	2.0	3.2
ETN-SKD10	n-type	Wet	3	1	2.2	4.6
ETN-SKD10	n-type	Wet	3	2	2.6	4.0
ETN-SKD10	n-type	Wet	3	3	2.8	4.0
ETN-SKD10	n-type	Wet	3	4	2.6	4.9
ETN-SKD10	n-type	Wet	4	1	2.6	5.2
ETN-SKD10	n-type	Wet	4	2	2.4	4.6

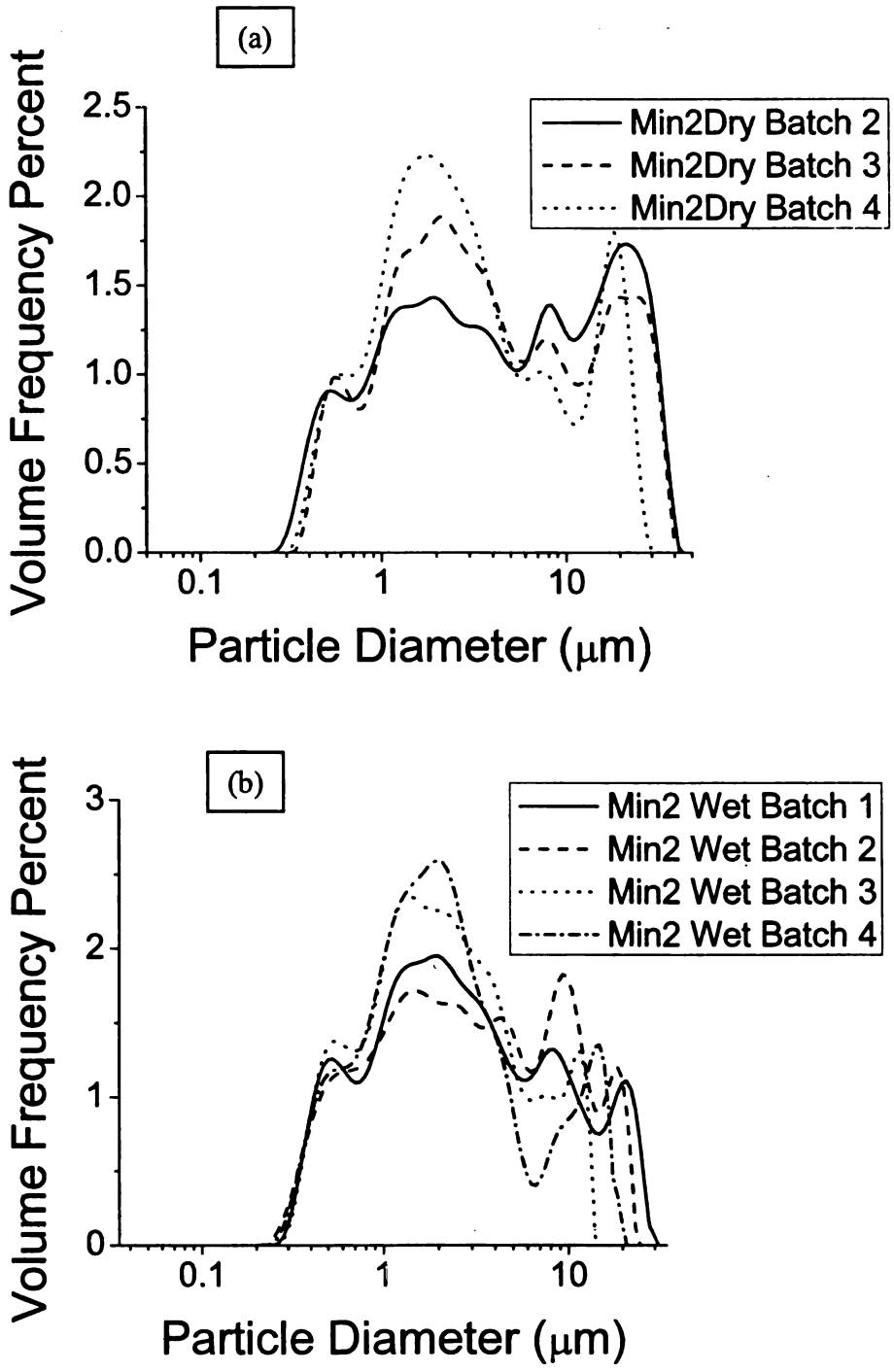

Figure 3.1 – Graph of particle size analysis of powders from ingot Min2-SKD, $Co_{0.95}Pd_{0.05}Te_{0.05}Sb_3$, doped with 0.1 atomic % Ce, from which the wet milled powders were used for specimen SKD-Wet1. The dry milling process produced a powder particle size distribution with two distinct modes at approximately 2 μm and 20 μm. When the dry milled powder was wet milled, the average particle size was reduced primarily by reducing the particle size of the larger particles.

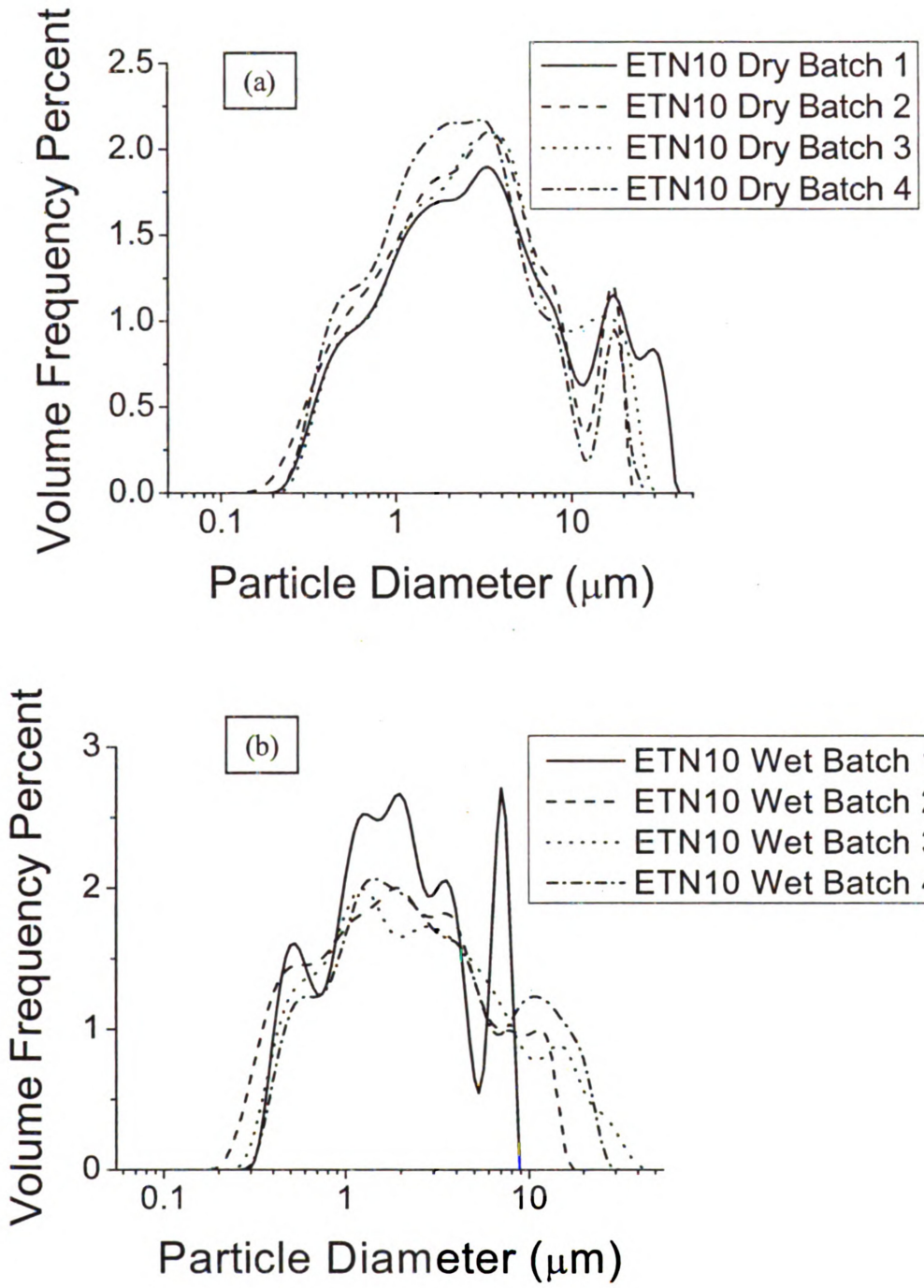

Figure 3.2 – Graph of particle size analysis of powders from ingot ETN-SKD-10, $Co_{0.95}Pd_{0.05}Te_{0.05}Sb_3$, from which the wet milled powders were used for specimen SKD-Wet2. The dry milling process produced a powder particle size distribution with two distinct modes at approximately 3 μm and 20 μm. When the dry milled powder was wet milled, the average particle size was reduced primarily by reducing the particle size of the larger particles. One representative test from each batch was chosen for graphing for clarity.

particle size distributon but a greater percentage of the powder was distributed near the smaller mode. The change between dry milling and wet milling suggests wet milling reduced the size of the larger particles but did not result in a general reduction of the entire range of particle sizes.

In the powder particle size distribution for ETN-SKD-10 (Figure 3.2), two modes in the particle size distribution were observed, one at approximately 3 μm and a second mode at 20 μm in both dry milled and wet milled powders. As with the Min2 powders (Figure 3.1), wet milling primarily reduced the particle size of the larger particles of the distribution, resulting in a smaller percentage of particles near the 20 μm mode.

The similar bimodal particle size distribution in both Min2-SKD and ETN-SKD-10 suggests two separate mechanisms occurring during milling. One mechanism maintained a distribution around 20 μm, and the mechanism was disturbed by adding a wet milling agent. Caking of the mill jar, particularly around the corner radius at the inside base of the jar, was typical of all milling batches, (Figure 3.3). Caking occurred on wet milled batches in the same location and manner as dry milled batches, but was more loosely caked to the surfaces and required less time scraping to remove. Two milling liquids for wet milling were used, as noted in Appendix A, and the caking amount and the difficulty to scrape the caking dropped significantly after changing from hexane to ethanol. While caking may not be the cause of the 20 μm mode, there is a correlation between caking and the larger particle sizes measured in the distribution.

Only one p-type powder particle size distribution was completed, from wet milled JSp-SKD15 batch 2. The measured median particle size was 2.253 μm and mean particle size was 3.611 μm, with a frequency distribution (Figure 3.4). In comparison to wet

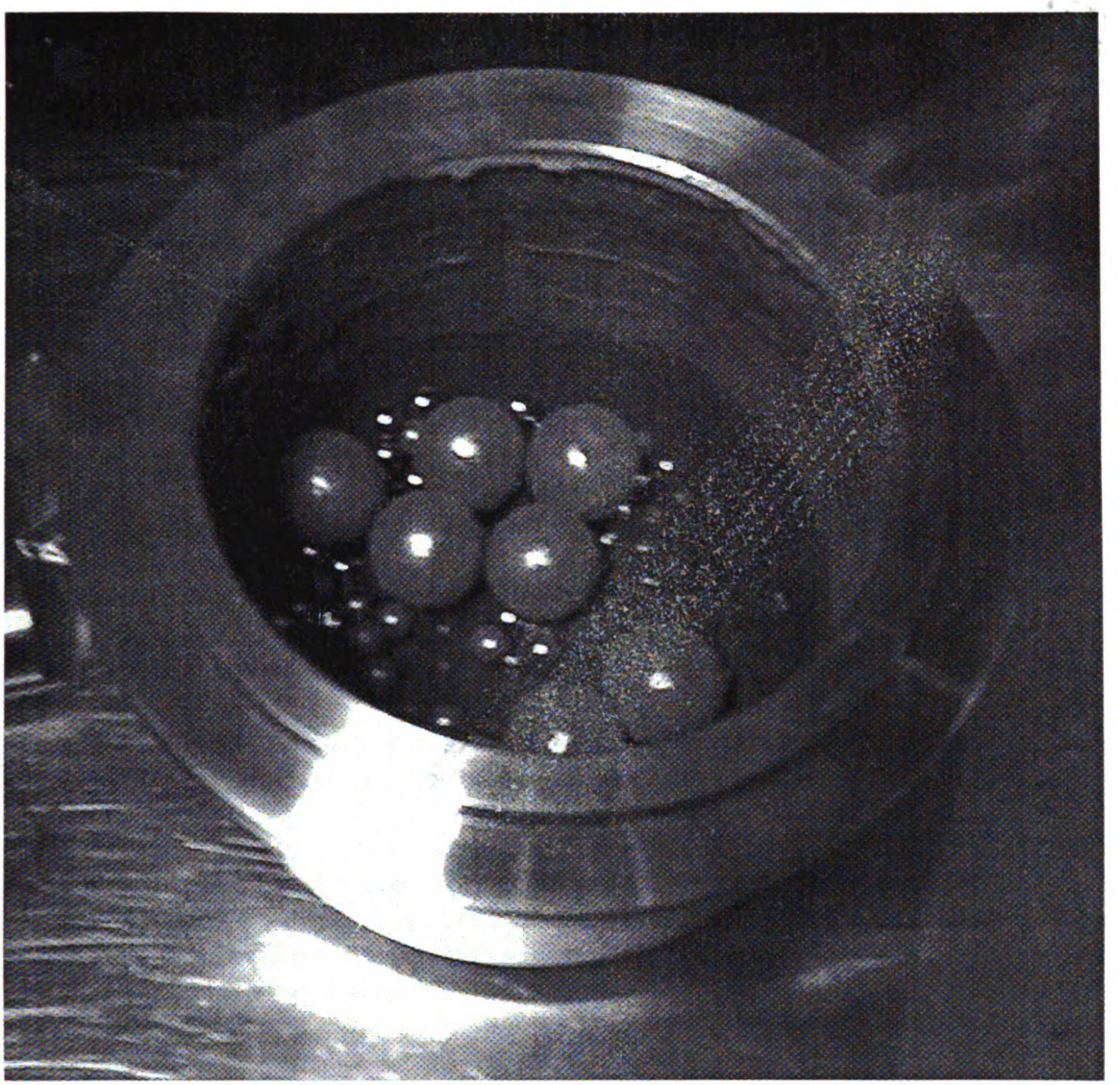

Figure 3.3 – Caking of the media and jar occurred on every mill run. Powder was visible in a layer on all sides of the jar from the wet milled run of powder from n-type ingot Min1a, $Co_{0.95}Pd_{0.05}Te_{0.05}Sb_3$ doped with 0.1 atomic % Ce. The caking was typical of all wet milling runs. Hexane remained in the bottom of the jar after milling. A switch to ethanol from hexane dramatically decreased the amount of scraping required to recover the powder, but all interior surfaces were coated regardless of liquid.

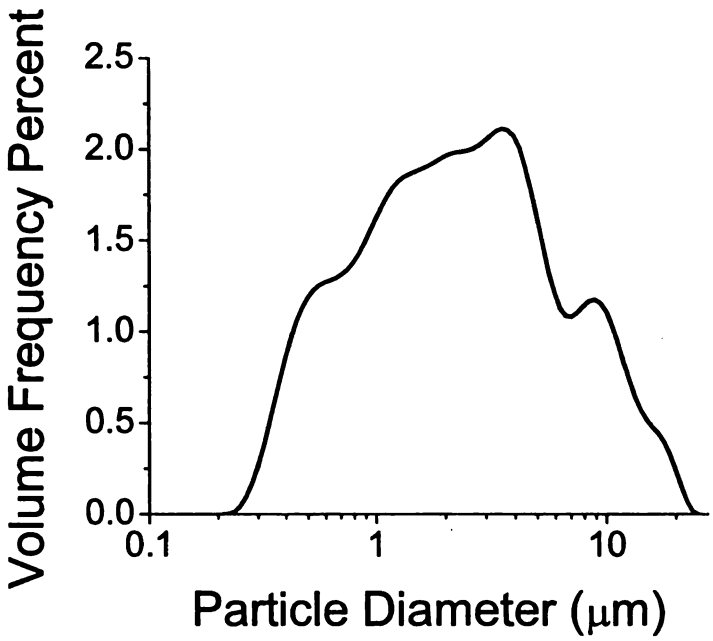

Figure 3.4 – Graph of particle size analysis for wet milled powder from ingot JSpSKD-15, $Ce_{0.9}Fe_{3.5}Co_{0.5}Sb_{12}$, Batch 2, one of 4 batches of milled powder from the same ingot used to make SKD-Wet3. Due to the second specimen showing pyrophoric behavior before it could be analyzed, this was the only batch analyzed. The hot pressed billet had a bimodal distribution, with a matrix of an average 1.2 μm diameter with grains interspersed of over 5 μm diameter. This bimodal character was not evident in the powder particle size distribution to the extent observed in the hot pressed specimens. The limited sample size of one prevented further investigation.

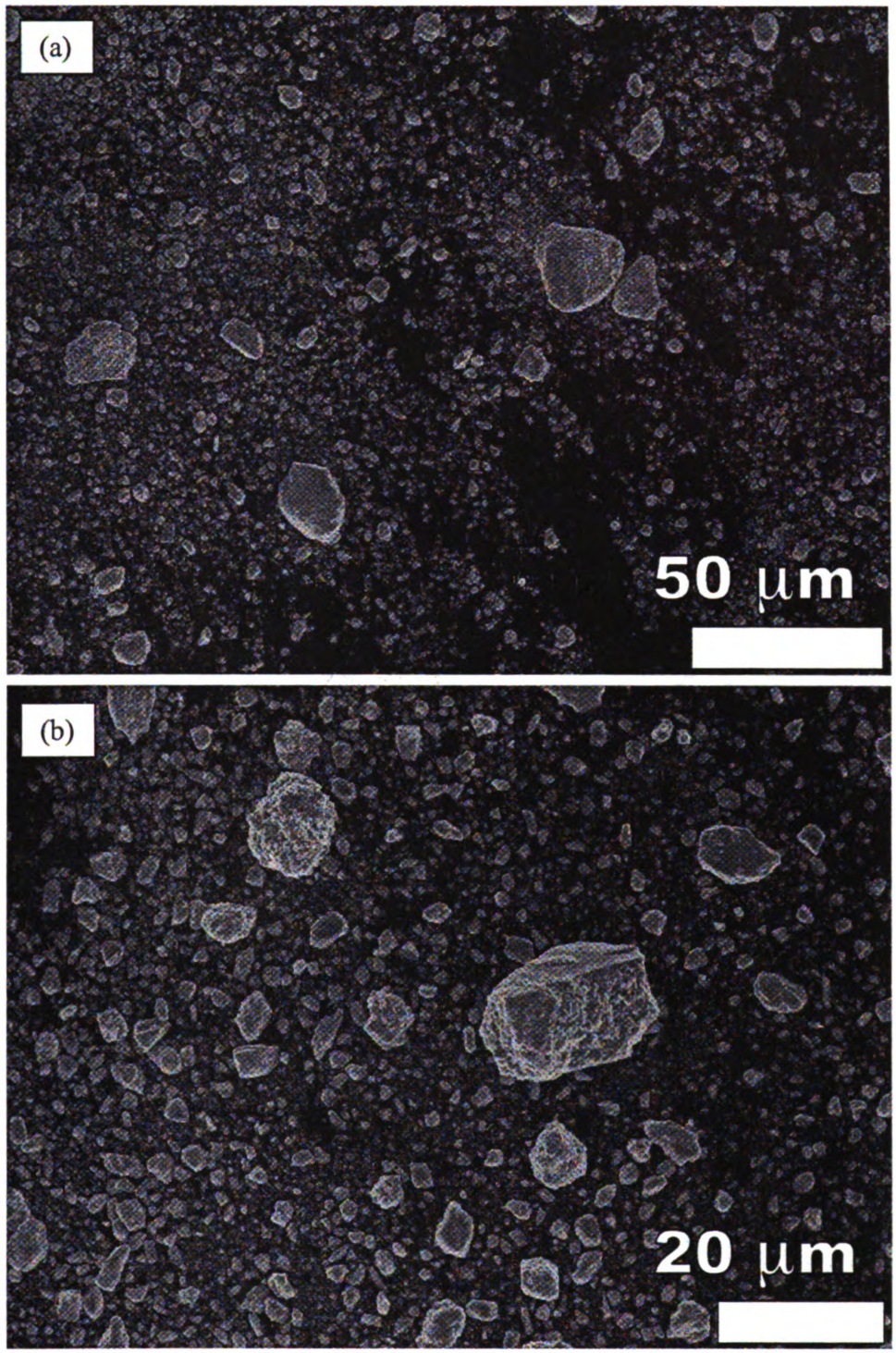

Figure 3.5 – Micrographs of dry milled (a) and wet milled (b) powders from nSKD-Min2 Batch 1, $Co_{0.95}Pd_{0.05}Te_{0.05}Sb_3$, doped with 0.1 atomic % Ce, for powder shape evaluation and qualitative comparison with laser particle size analysis. The sizes of the particles observed by SEM are consistent with the laser particle size analysis. Note the length scale change between the dry milled and the wet milled powder. Cleavage planes are seen in the largest particle (b).

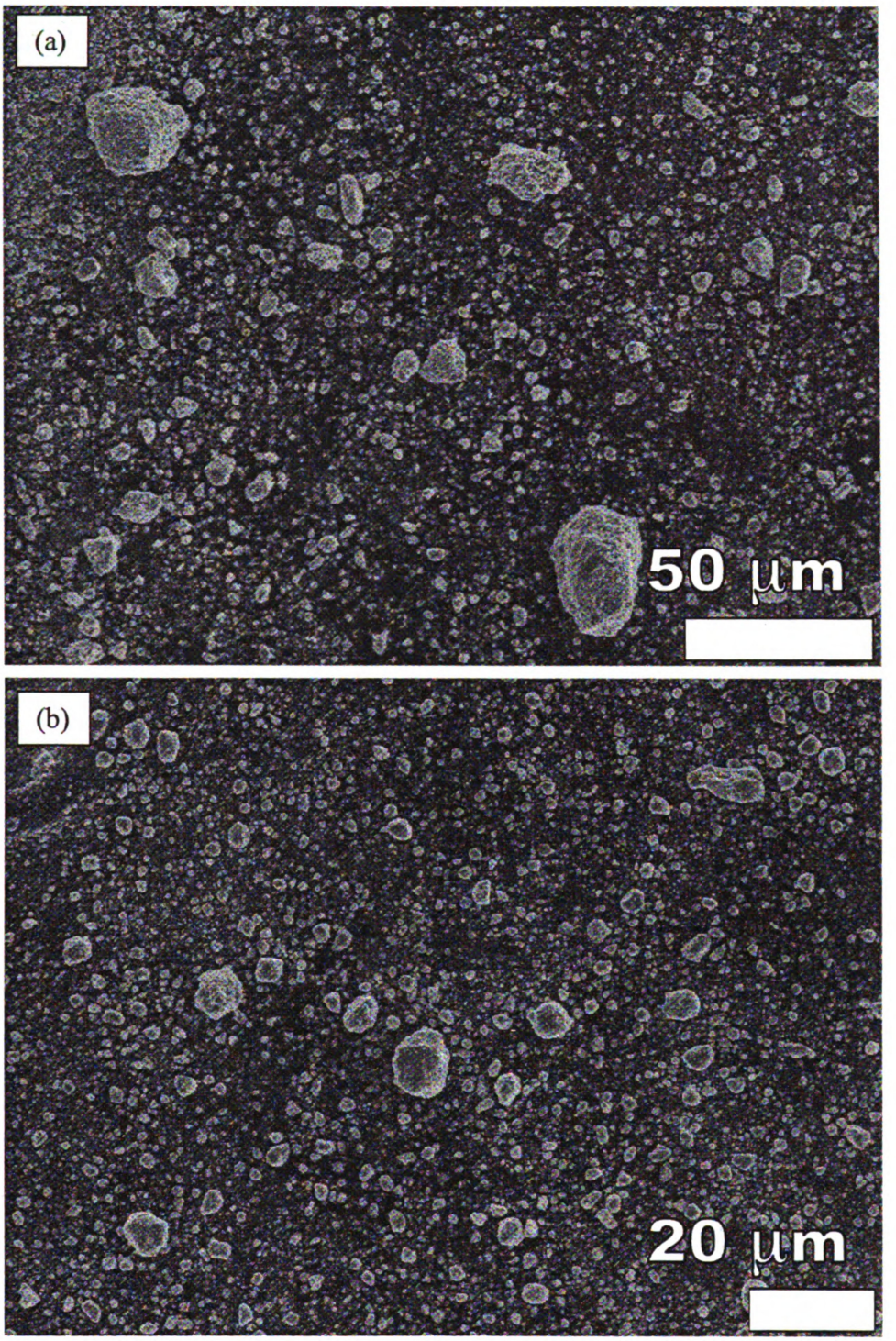

Figure 3.6 – Micrographs of dry milled (a) and wet milled (b) powders from nSKD-Min2 Batch 2, $Co_{0.95}Pd_{0.05}Te_{0.05}Sb_3$, doped with 0.1 atomic % Ce, for powder shape evaluation and qualitative comparison with laser particle size analysis. The sizes of the particles observed by SEM are consistent with the laser particle size analysis. Note the length scale change between the dry milled and the wet milled powder.

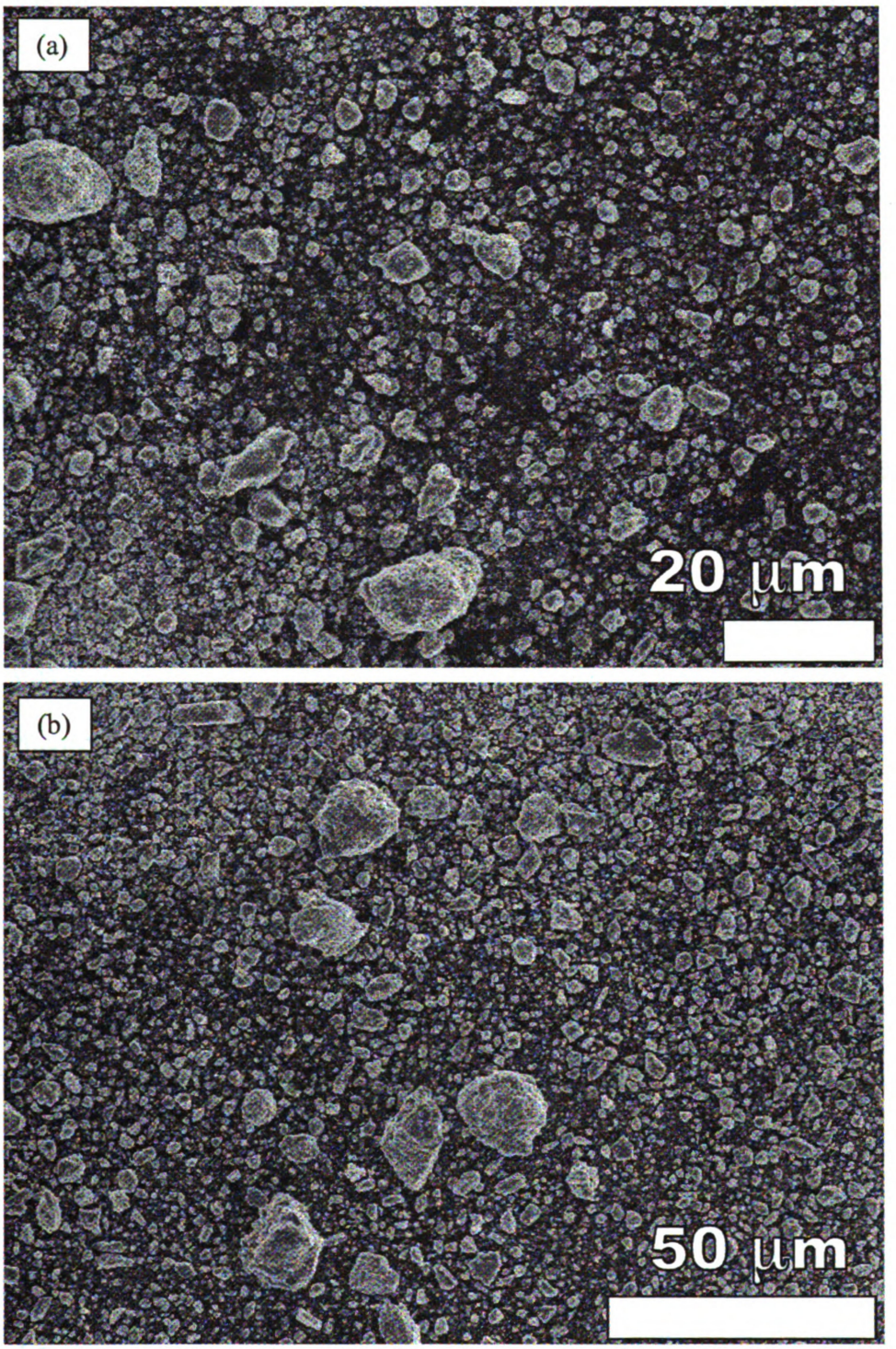

Figure 3.7 – Micrographs of dry milled (a) and wet milled (b) powders from nSKD-Min2 Batch 3, $Co_{0.95}Pd_{0.05}Te_{0.05}Sb_3$, doped with 0.1 atomic % Ce, for powder shape evaluation and qualitative comparison with laser particle size analysis. The sizes of the particles observed by SEM are consistent with the laser particle size analysis. Note the length scale change between the dry milled and the wet milled powder.

milled powders from Min2 and ETN-SKD-10, (Figures 3.1b and 3.2b), wet milled JSp-SKD15 powder included fewer particles over 10 μm. The amount of observed particles in JSp-SKD15 over 10 μm changed after sintering (see section 3.2).

The second batch of JSp-SKD15 powder to be tested caught fire as approximately 0.1 g of powder was being drawn out of the vial on a metal spatula. Both the batch that was analyzed and the batch that ignited were from powder batches wet milled in ethanol. Based on processing conditions, both batches were expected to be of a similar particle size distribution, but was unconfirmed. After the fire, particle size analysis of JSp-SKD15 was discontinued.

Micrographs of the milled powders from Min2-SKD were consistent with the particle size distribution measured from the Saturn Digisizer, with the observed powder particle sizes within the range of 0.1 to 20μm (Figures 3.5 through 3.7). The particle sizes in the micrographs (Figures 3.5 through 3.7) included a few larger particles of 10 μm or greater, with cleavage planes evident (Figure 3.5b) on the surface. The cleavage planes indicate mechanical cleaving of the particles, indicative of particle size reduction from the ball milling. Other surfaces show agglomeration of smaller particles together, and some rounding of the particle corners, particularly evident on the wet milled batches (Figures 3.5b, 3.6b, 3.7b). The particles had typical aspect ratios of less than 5:1, with most under 2:1.

3.2 Microstructural evaluation

The specimen microstructural was analyzed to (i) determine the grain size and (ii) identify and characterize the size, shape and spatial distribution of porosity. Specimens for microstructural analysis were prepared by either (i) thermally etch polished specimens or by (ii) fracturing specimens. The powder particle size distribution prior to sintering was compared to the grain size distribution following sintering. The powder particle size distributions of powder batches after batch 1 of JSpSKD-15 were not analyzed due to pyrophorocity of the skutterudite powders.

All bulk specimens were examined as polished (Figure 3.8). The as-polished surfaces exhibited fully sintered specimens and observed porosity consistent with relative densities of 0.94 or greater. Each specimen was polished to a final polishing grit of 1 μm prior to SEM observation, then examined as-polished prior to attempting to thermally etch the specimen surfaces. The SEM micrographs of the polished surfaces showed porosity amounts consistent with the measured density of each specimen (Figure 3.8).

Hot pressed billet SKD-Wet1, produced from wet milled powders from n-type ingot SKD-Min2, a $Co_{0.95}Pd_{0.05}Te_{0.05}Sb_3$ with 0.1 atomic % cerium doped billet, contained isolated quasi-spherical pores, 1 μm or less in diameter (Figure 3.8a). The porosity in hot pressed billet SKD-Wet2, fabricated from wet milled powders of ingot ETN-SKD10, $Co_{0.95}Pd_{0.05}Te_{0.05}Sb_3$, clustered or in linear arrays (Figure 3.8b), but otherwise was similar in size and shape to the porosity in SKD-Wet1 (Figure 3.8a). The observed porosity for SKD-Wet2 (Figure 3.8b) was greater than that exhibited in

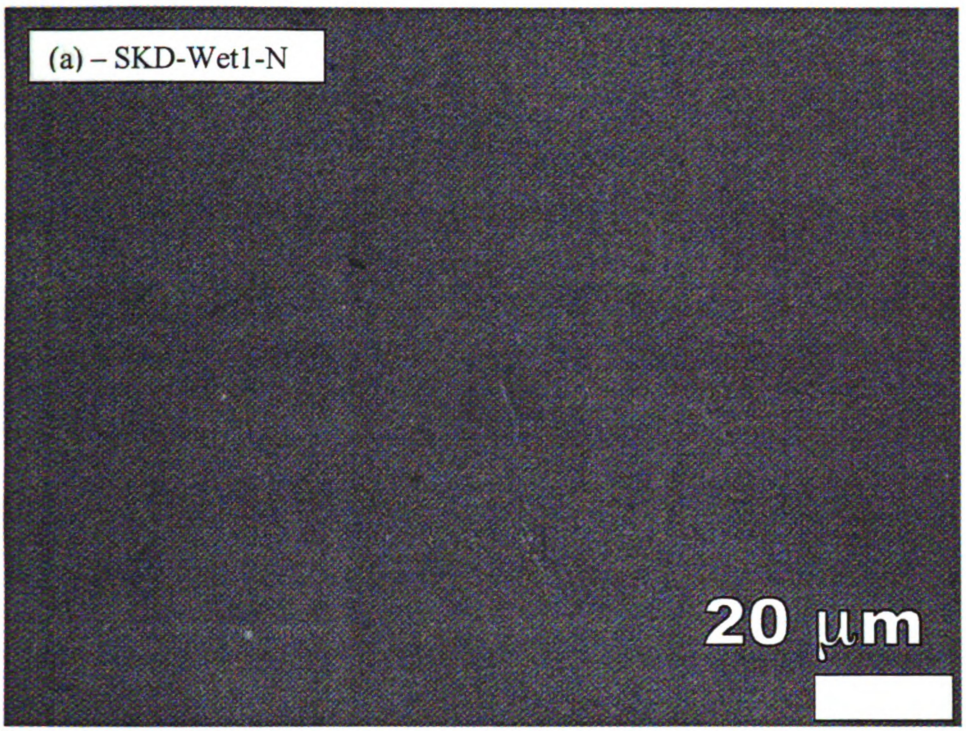

Figure 3.8 – Polished surface SEM micrographs. The polished surfaces showed properly sintered specimens with limited porosity, consistent with measured densities of 0.93 and greater. The specimen SKD-Wet1N, $Co_{0.95}Pd_{0.05}Te_{0.05}Sb_3$, doped with 0.1 atomic % Ce, showed isolated spherical porosity less than 1 μm in diameter (a). Specimen SKD-Wet2J $Co_{0.95}Pd_{0.05}Te_{0.05}Sb_3$, showed numerous isolated spherical porosity, less than 1 μm in diameter (b). Specimen SKD-Wet3N showed polygonal porosity often clustered in groups of 2 to 4, 1 to 3 μm in diameter (c). Specimen SKD-Wet4J, $Co_{0.95}Pd_{0.05}Te_{0.05}Sb_3$, showed numerous quasi-spherical pores, less than 1 μm in diameter (d). Specimen SKD-18 showed clustered polygonal porosity, often in groups of greater than 4, 1 to 2 μm in diameter (e).

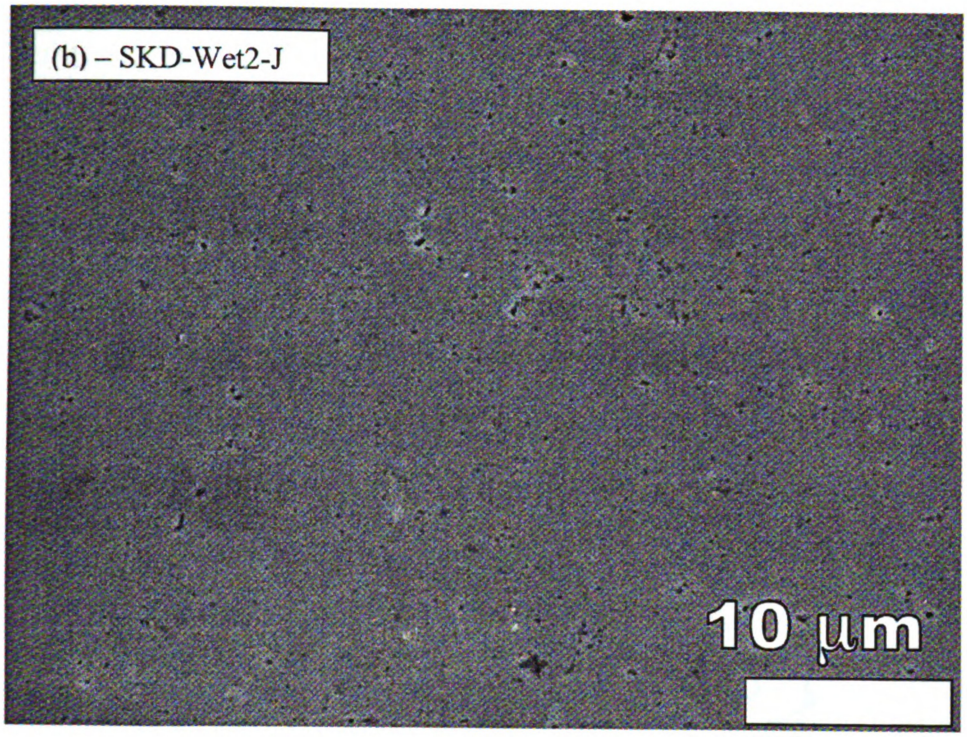

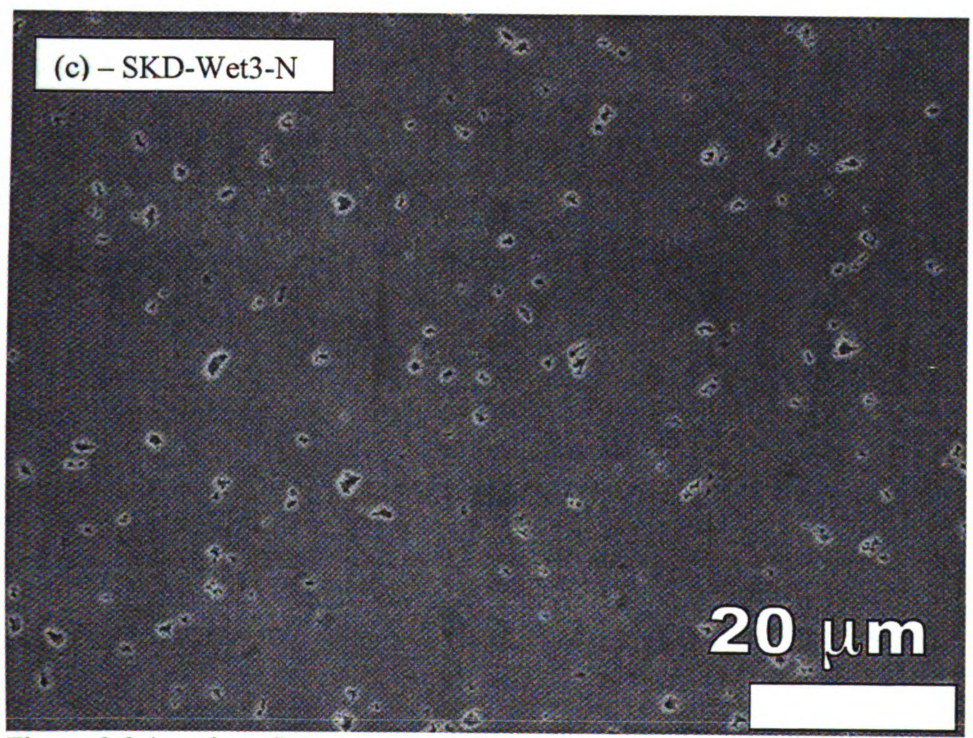

Figure 3.8 (continued)

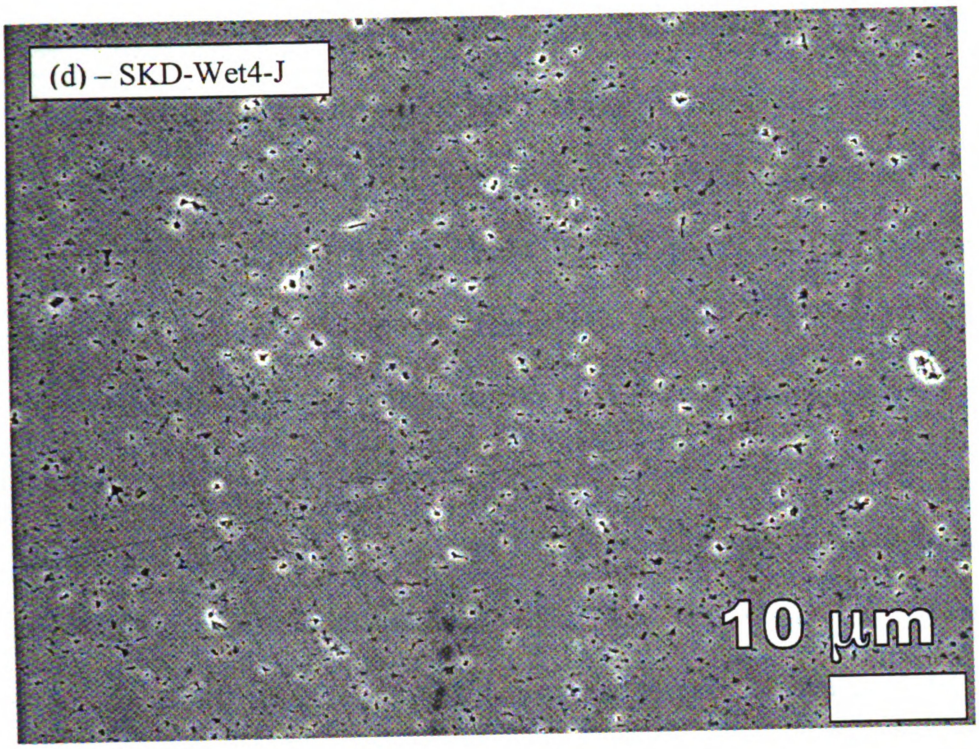

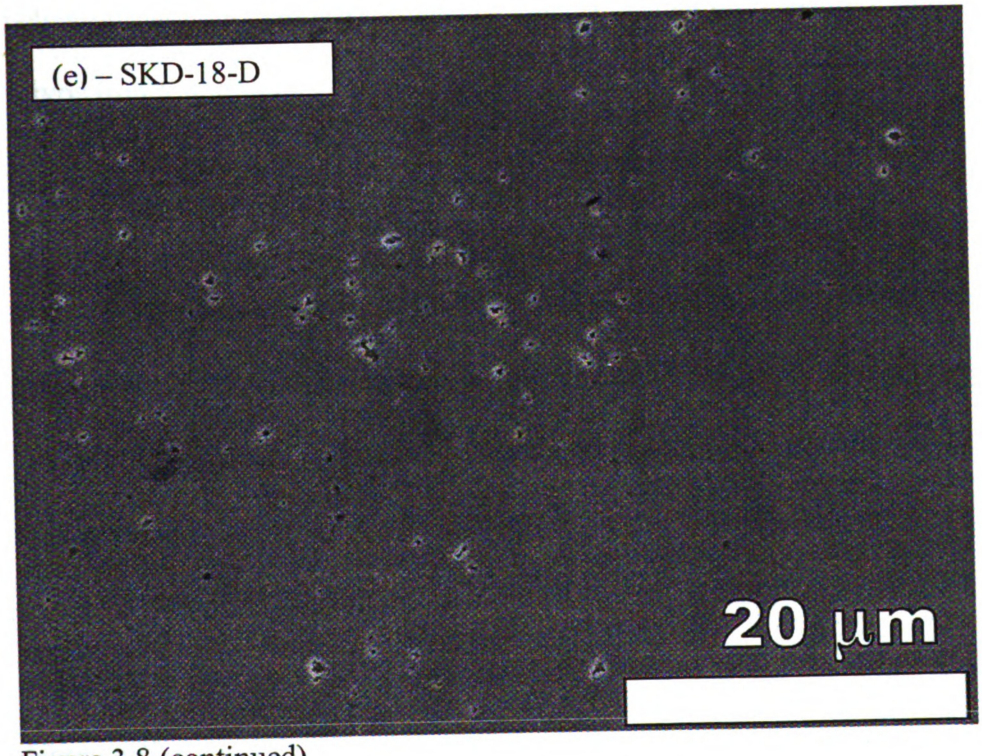

Figure 3.8 (continued)

SKD-Wet1 (Figure 3.8a), as expected for a specimen with a smaller relative density of 0.960, versus the relative density of 0.977 in SKD-Wet1.

The porosity of the p-type billet SKD-Wet3, $Ce_{0.9}Fe_{3.5}Co_{0.5}Sb_{12}$ hot pressed from wet milled powders of ingot JSp-SKD-15, was polygonal, often clustered in groups of up to 4 pores, and 1-3 μm in diameter. The relative density of SKD-Wet3, at 0.955, and SKD-Wet2, at 0.960, were similar, but the larger, clustered and polygonal porosity observed in SKD-Wet3 indicated the two did not sinter in the same way. The powder particle size distribution of wet milled SKD-Wet3 (Figure 3.4) was in the same range of size as the wet milled powders for SKD-Wet1 and SKD-Wet2 (Figure 3.1 and Figure 3.2). The difference in composition may account for the differences in the sintering behavior that may in turn result in differing pore structures and sizes. SKD-Wet3 was a p-type iron triantimonide-based composition while SKD-Wet1, SKD-Wet2 and SKD-Wet4 were all n-type cobalt triantiomide-based compositions.

Hot pressed billet SKD-Wet4, produced from wet milled powders of ingot JSn-SKD-14, was the same $Co_{0.95}Pd_{0.05}Te_{0.05}Sb_3$ composition as SKD-Wet2, and the size and shape of the porosity was similarly 1 μm or less and quasi-spherical pores (Figure 3.8d). Unlike SKD-Wet2, the porosity was clustered and in linear arrays of pores. The relative density of SKD-Wet4 was 0.936, which was lower than any other specimen observed, and consistent with an observation of more porosity on the polished surface. The number and shape of pores present suggest pore consolidation did not occur in SKD-Wet4 to the degree and extent of SKD-Wet3.

Billet SKD-18 was the same composition as SKD-Wet3, $Ce_{0.9}Fe_{3.5}Co_{0.5}Sb_{12}$, and the porosity was similar in 1-3 μm size, polygonal shape and distribution in clusters. The

relative density, at 0.975, was less than SKD-Wet3, and was consistent with the observed porosity (Figure 3.8e). The similarity in the appearance of the porosity suggests the sintering behavior of SKD-Wet3 and SKD-18 were also similar.

Specimens of SKD-Wet2 (Figure 3.9), SKD-Wet4 (Figure 3.10) and SKD-31-9 (Figure 3.11) were successfully thermally etched in vacuum at 873 K. The time of sintering varied from 4 hours (SKD-Wet2) to 2 hours (SKD-Wet4) to 1.5 hours (SKD-31-9). The grain sizes measured from the micrographs (Figures 3.9 – 3.11) were from 1.1 μm to 2.8 μm (Table 3.3). In contrast to the successful thermal etching of SKD-Wet2, SKD-Wet4 and SKD-31-9, the thermal etching of specimens of SKD-Wet1 and SKD-Wet3 was not successful. The thermal etch conditions attempted for SKD-Wet1 were in a flowing argon atmosphere in the tube furnace for 2 and 4 hours at 873 K, and in vacuum in an ampoule for 1.5 hours at 823 K and 873 K. For SKD-Wet3, the thermal etch was attemped in vacuum in an ampoule for 1.5 hours at 823 K and 873 K.

The successful thermal etch results from specimens SKD-Wet2, SKD-Wet4 and SKD-31-9 could not be reproduced on specimens SKD-Wet1 and SKD-Wet3. The thermal etching process for specimens SKD-Wet1 and SKD-Wet3 failed due to (i) material condensed on the surface, obscuring the etched surface or (ii) insufficient etch to distinguish grains within the billet. Specimens of SKD-Wet1 etched in a tube furnace could not be observed due to a buildup of material on the surface. Etch attempts at 823 K in vacuum were unsuccessful on specimens of SKD-Wet1 and SKD-Wet2, with no observed etching. Successful thermal etching of SKD-Wet2 and SKD-Wet4 occurred in a sealed glass ampoule approximately 20 cm long and 2.5 cm in diameter, with the specimen at one end inside the furnace and the other end outside the furnace exposed to

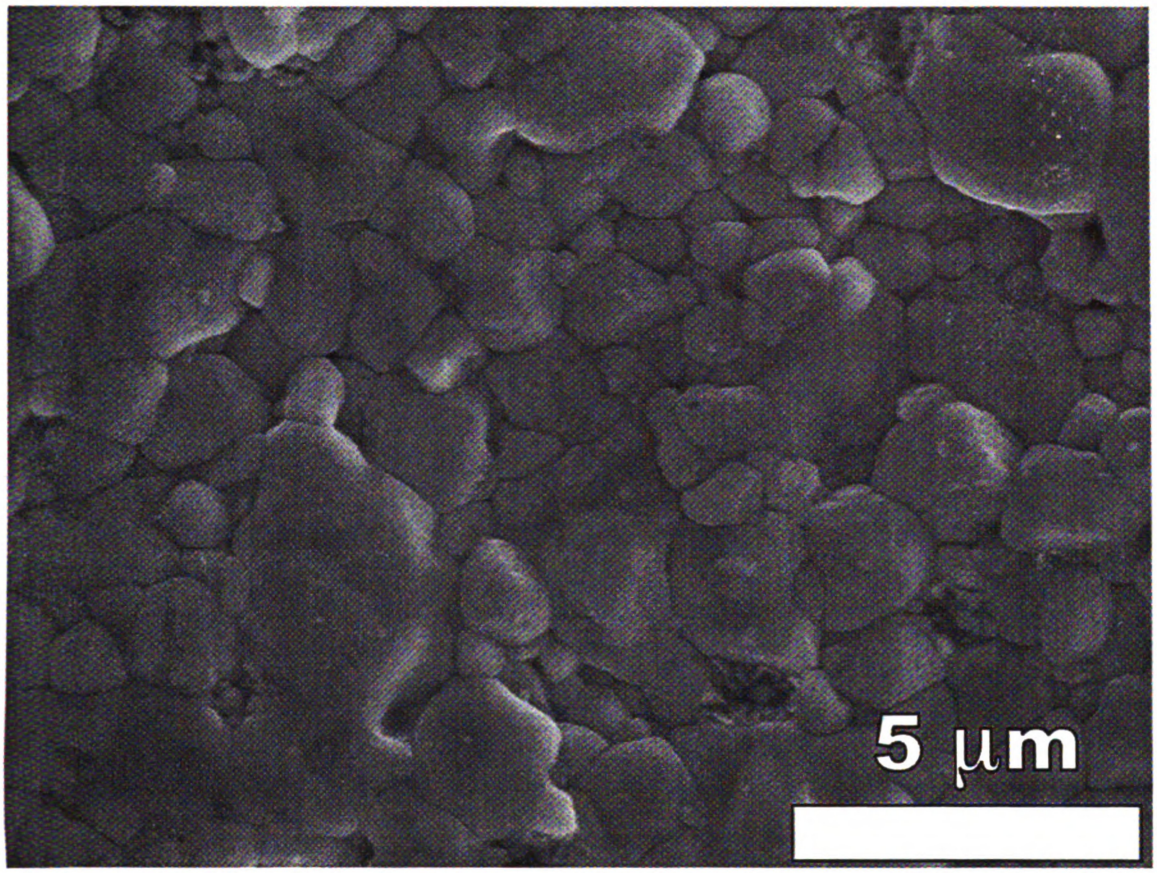

Figure 3.9 – Thermal etch SEM micrographs of SKD-Wet2I, $Co_{0.95}Pd_{0.05}Te_{0.05}Sb_3$, exhibited cross sectional grain sizes from sub-micron to 5 μm, consistent with expectations based on powder particle size distribution measurements for powders used to hot press the specimen. The specimen was sealed in a silica ampoule in vacuum, heated to 873 K and held for 4 hours at temperature.

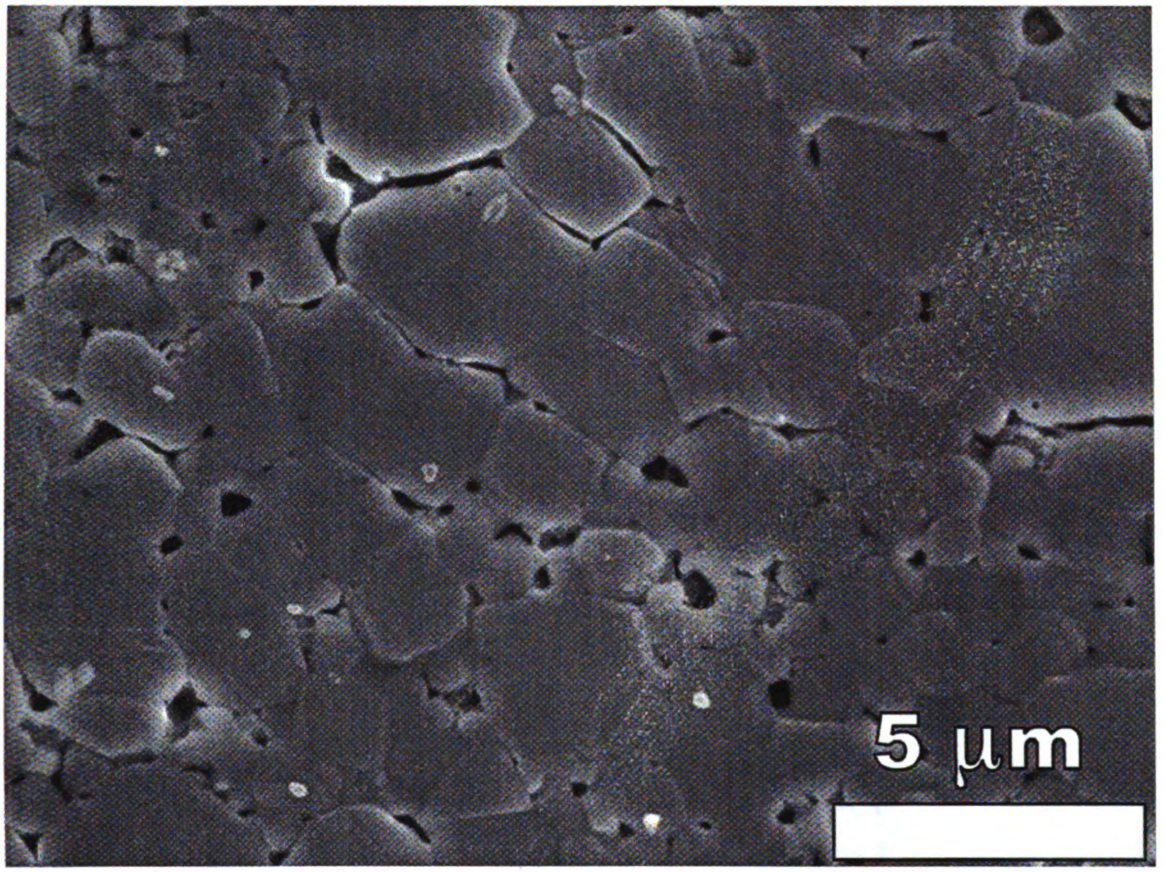

Figure 3.10 – Thermal etch SEM micrograph of SKD-Wet4J1, $Co_{0.95}Pd_{0.05}Te_{0.05}Sb_3$, exhibited cross sectional grain sizes from sub-micron to 5 μm, similar to the results of SKD-Wet2I of the same composition, and consistent with expectations based on similar processing methods. The specimen was sealed in a silica ampoule in vacuum, heated to 873 K and held for 2 hours at temperature.

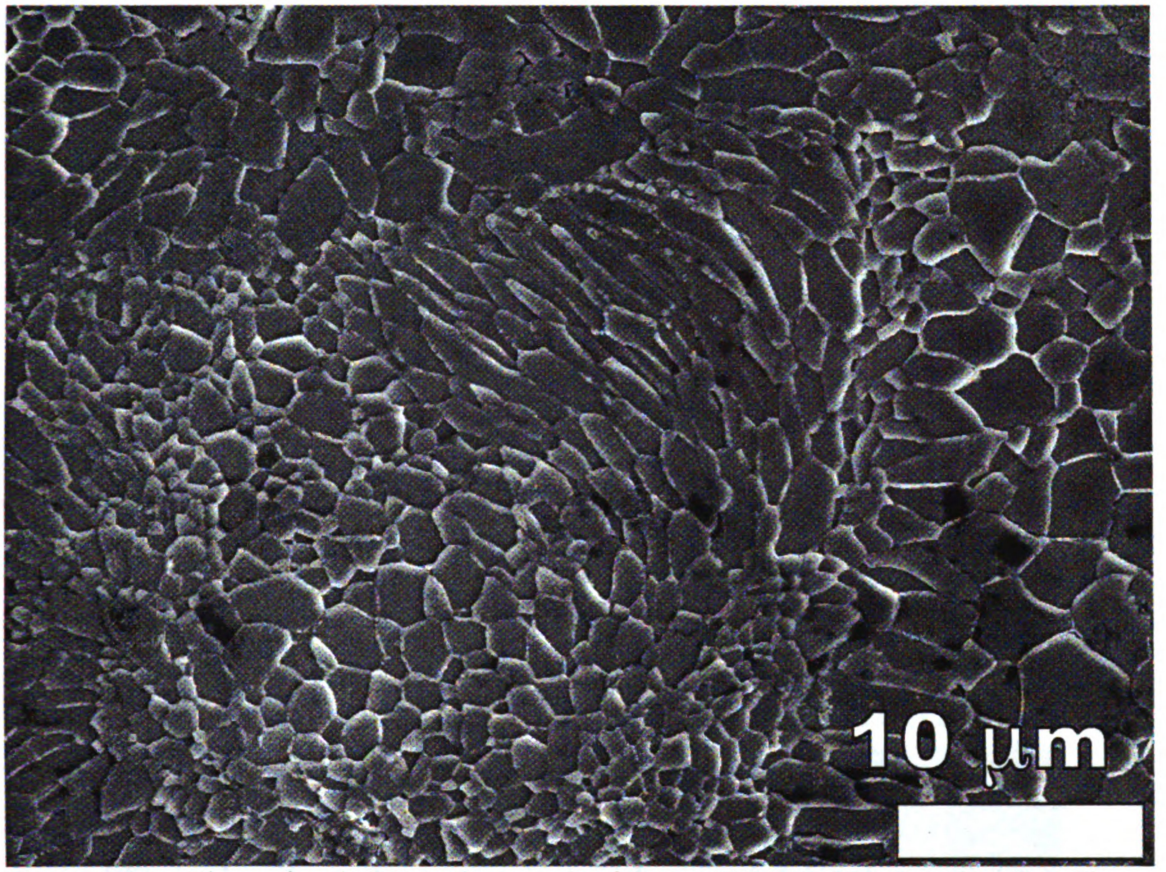

Figure 3.11 – Thermal etch SEM micrograph of p-type SKD-31-9D, $Ce_{0.9}Fe_{3.5}Co_{0.5}Sb_{12}$, after 1.5 hour at 873 K in a sealed ampoule. The specimen exhibited cross sectional grain sizes of approximately 1.8-2.8 μm, which were larger than any of the wet milled specimens, and consistent with expectations for a specimen hot pressed from dry milled powders. The specimen was sealed in a silica ampoule in vacuum, heated to 873 K and held for 1.5 hours at temperature.

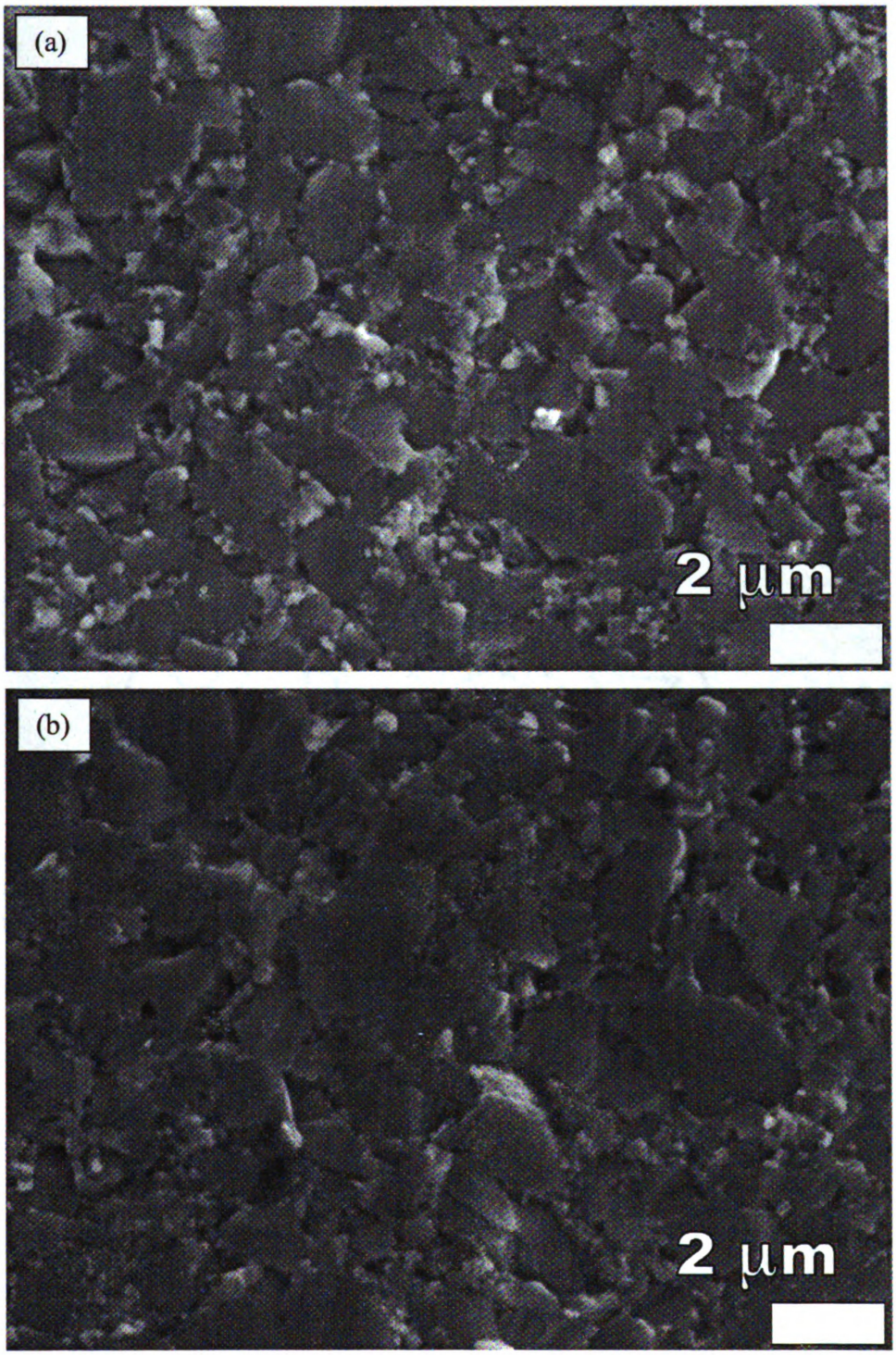

Figure 3.12 – Fracture surface SEM micrographs of SKD-Wet1M, $Co_{0.95}Pd_{0.05}Te_{0.05}Sb_3$ with 0.1 atomic % Ce, exhibited fracture surface grain sizes from sub-micron to 5 μm, consistent with expectations based on powder particle size distribution measurements for powders used to hot press the specimen. Average grain size from these micrographs was 1.0 μm.

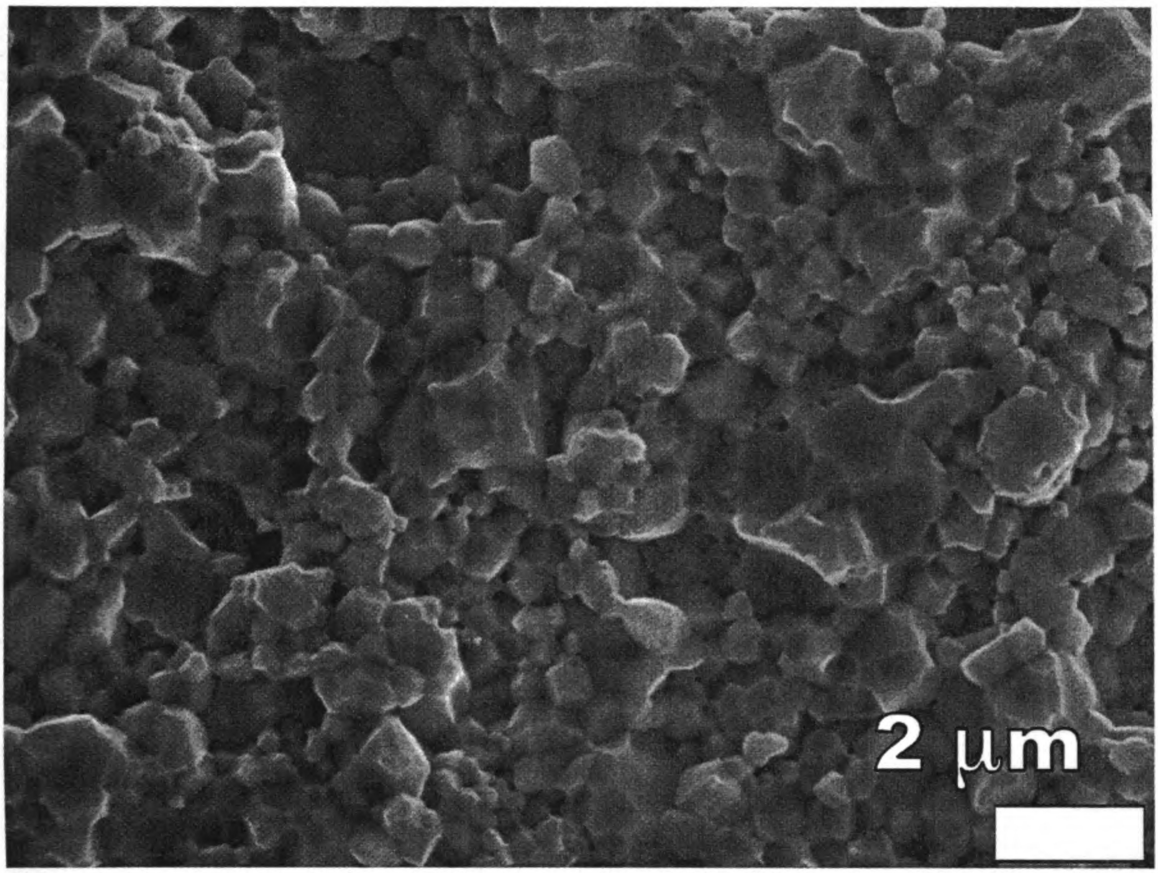

Figure 3.13 – Fracture surface SEM micrographs of SKD-Wet2, $Co_{0.95}Pd_{0.05}Te_{0.05}Sb_3$, exhibited fracture surface grain sizes from sub-micron to 5 μm, consistent with expectations based on powder particle size distribution measurements for powders used to hot press the specimen. Average grain size from these micrographs was 1.0 μm.

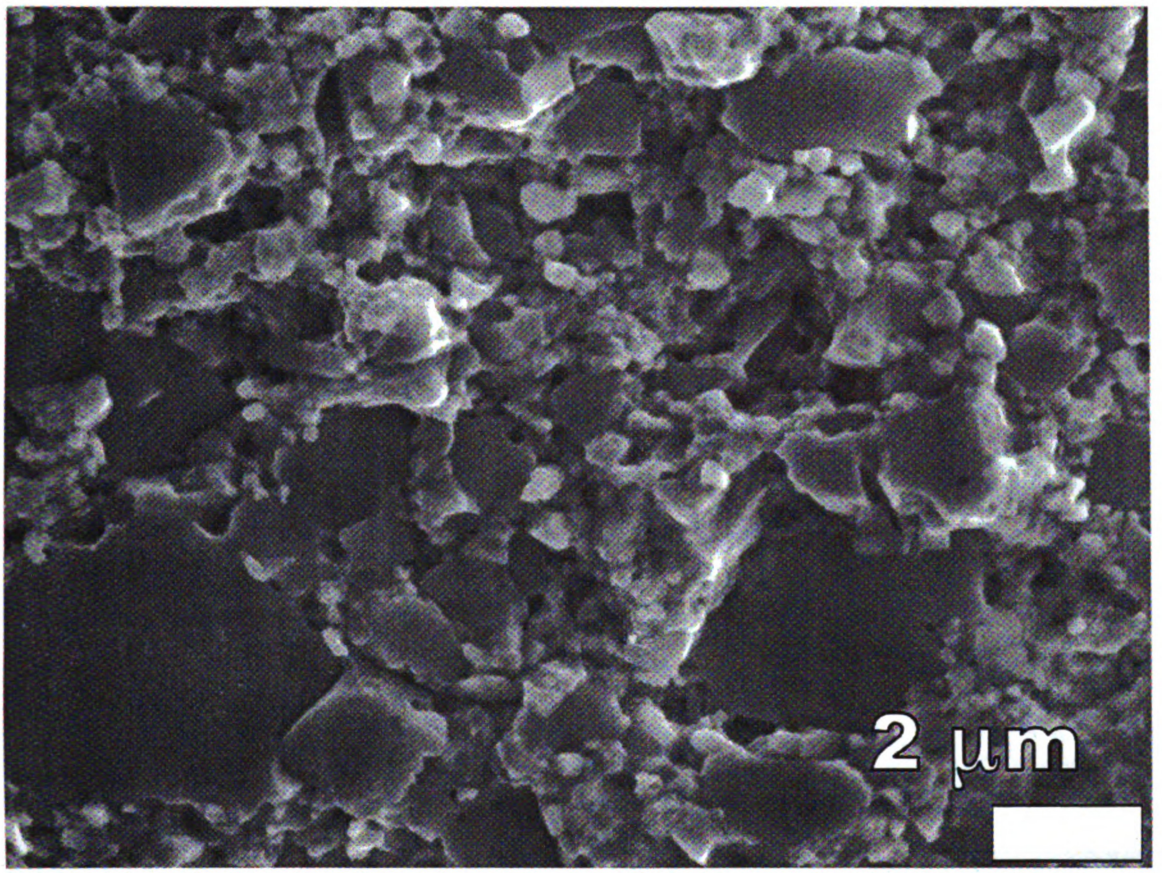

Figure 3.14 – Fractured surface microstructure SEM micrographs of SKD-Wet3I, $Ce_{0.9}Fe_{3.5}Co_{0.5}Sb_{12}$. The fracture revealed a bimodal distribution of 5-10 μm grains within a matrix of 1.2 μm average grain size.

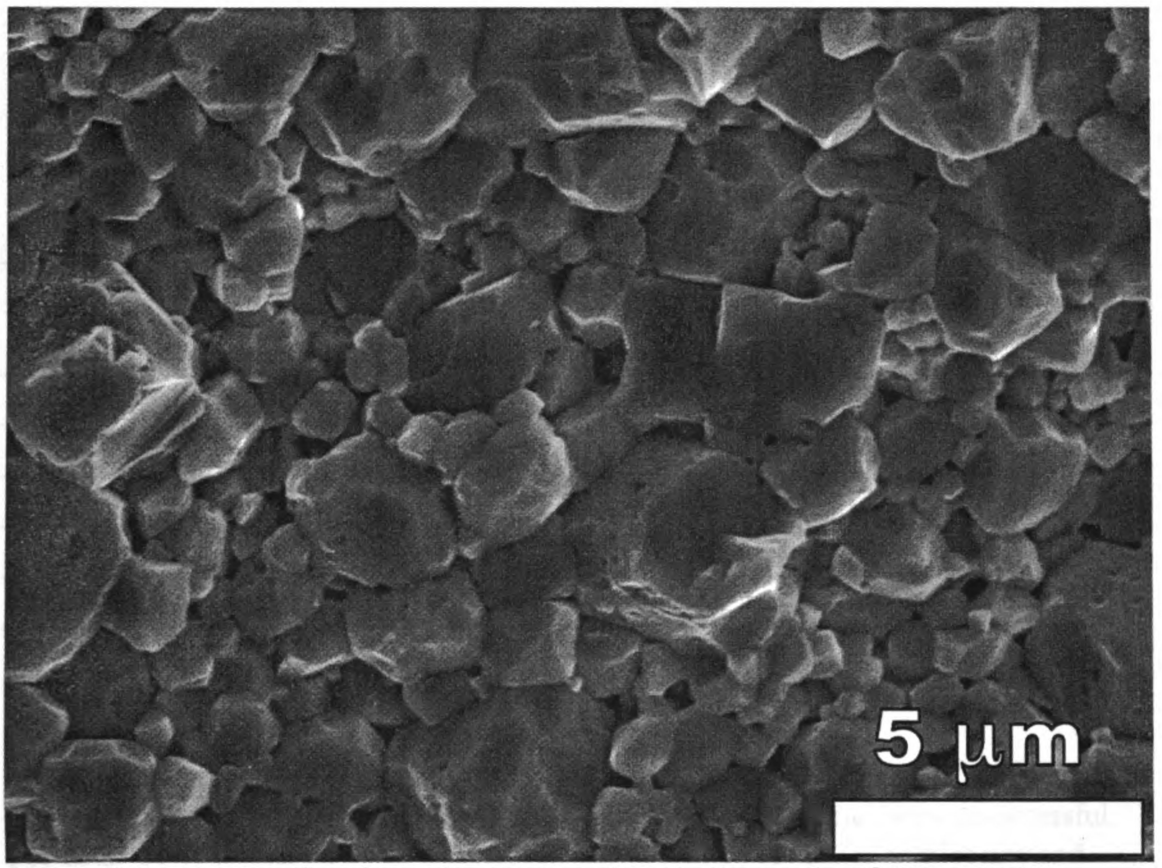

Figure 3.15 – Fractured surface microstructure SEM micrographs of SKD-Wet4J2, $Co_{0.95}Pd_{0.05}Te_{0.05}Sb_3$. The fracture occurred mostly intergranular, with a possible bimodal distribution evident.

Table 3.3 – Grain size for all wet milled specimens was observed to be below 2 μm for the matrix. The p-type specimen, SKD-Wet3, composition $Ce_{0.9}Fe_{3.5}Co_{0.5}Sb_{12}$, exhibited bimodal structure with some larger grains of 5-10 μm within the matrix. Given the grain sizes observed, any grain size distribution between the wet milled specimens will be limited to the range of 1-2 μm.

Billet Label	Type	Grain Size via Fracture (μm)	Grain Size via Thermal Etch (μm)
SKD-Wet1	n-type, Ce-doped	0.9-1.0[a]	NA[b]
SKD-Wet2	n-type	1.5	1.3-1.7[a]
SKD-Wet3	p-type	1.2[c]	NA[b]
SKD-Wet4	n-type	1.7-2.0[a]	1.1-1.5[a]
SKD-31-9	n-type	NA[b]	1.8-2.8[a]

[a]Range is provided when more than one SEM micrograph of the same specimen was analyzed.

[b]NA – Not Available. For SKD-Wet1 and SKD-Wet3, thermal etch was unsuccessful. For SKD-31-9, further analysis was not run due to limited specimen availability and limited processing information.

[c]SKD-Wet3 exhibited bimodal grain sizes, with grains of 5-10 μm interspersed within the 1.2 μm matrix.

room temperature. Regardless of the soak time, after each thermal etch, the inside of the ampoule (on the "cold" end of the ampoule that stuck outside the furnace) was partially coated with an unidentified silvery substance, indicating that the cold end of the ampoule likely served as a cold trap during the thermal etching process.

All specimens were successfully fractured for grain size analysis (Table 3.3). For consistency and comparative analysis, all billets hot pressed from wet milled powders were fractured, and the images used for grain size analysis (Figures 3.12 through 3.15) using the linear intercept technique with a 1.5 stereographic projection factor. The grain size via fracture was 0.9 to 2.0 μm (Table 3.3).

The calculated mean grain size from fractured surface of SKD-Wet1 ($Co_{0.95}Pd_{0.05}Te_{0.05}Sb_3$ with 0.1 atomic % doping of Ce) was 1.0 μm (Figure 3.12).

The calculated mean grain size of the hot pressed billet SKD-Wet2 ($Co_{0.95}Pd_{0.05}Te_{0.05}Sb_3$) was 1.5 μm, For a thermally etched surface of SKD-Wet2, the mean grain size calculated from the linear intercept technique was 1.68 μm. For the fractured surface and the thermally etched surface, a 1.5 stereographic projection factor was used.

Hot pressed billet SKD-Wet3 exhibited a bimodal grain size, with a matrix of 1.2 μm diameter grains surrounding grains roughly 5 to 10 μm using a fractured surface.

The powder used to hot press SKD-Wet3 (milled from ingot JSp-SKD15) was only analyzed with a single wet milled batch in the Saturn Digisizer. That single batch of milled powder indicated fewer large particles in the 5 to 10 μm range than in the powders used to hot press SKD-Wet1 or SKD-Wet2. The 5-10 μm grains within the matrix cannot be explained as pre-existing, as the same larger particles existed in equal or greater

quantity in SKD-Wet1 and SKD-Wet2, but larger grains did not appear in the hot pressed billets as frequently as in SKD-Wet3. The 5-10 μm grains observed in SKD-Wet3 developed after powder processing, during the sintering process. A difference in the sintering behavior is consistent with the observation of the polished surface (Figure 3.8c) of difference in the pores of SKD-Wet3 and the other three wet milled billets (Figure 3.8a, b, and d).

The mean grain size calculated from hot pressed billet SKD-Wet4 by the linear intercept technique was approximately 1.1 to 1.5 μm on a fractured surface. For a thermally etched surface, the calculated mean grain size was 1.7 to 2.0 μm. Both the specimens with the polished/thermally etched surfaces and specimens with the fractured surfaces were cut from the same specimen, SKD-Wet4J.

3.3 Room Temperature Elastic Moduli and Porosity

3.3.1 Room Temperature Elastic moduli by RUS

Each elastic modulus from room temperature Resonant Ultrasound Spectroscopy (RUS) (Table 3.4) was averaged from measurements of resonance spectra for 6 to 8 specimens per billet, and error as one standard deviation of the average. Each billet was a different density (Table 3.5), and as density increased for a type of material, so too did the Young's modulus and shear modulus. The change in modulus may be partially or mostly attributable to changes in porosity [Rice 1998].

The room temperature elastic moduli of the specific skutterudite compounds in this study are reported in only one source, a previously published in a paper by Schmidt et al. based on the same data in this thesis (Table 3.4) [Schmidt 2010], but studies of the elastic moduli for similar antimony-based skutterudite compounds have been published [Ravi 2007, Recknagel 2008]. Comparing the Young's and shear modulus of the skutterudite material in this study to the same properties of similar antimony-based compounds, the moduli in this study (Table 3.4) are within the range published by the Young's and shear modulus from Ravi and Recknagel [Schmidt 2010].

For n-type doped $CoSb_3$, Ravi published a Young's modulus of 137-141 GPa and a shear modulus of 60.7 GPa [Ravi 2007]. For n-type $CoSb_3$, Recknagel published a Young's modulus of 148 ± 26 GPa [Recknagel 2008]. The Young's modulus for the n-type skutterudite material in this study ranged from 129 to 141 GPa, completely contained within the range set by Ravi and Recknagel [Ravi 2007, Recknagel 2008].

Table 3.4 - Elastic moduli data for the wet milled billets and one production billet, averaged from multiple specimens tested. The specimens exhibited some differences based on porosity and composition effects. The porosity relationship may be observed between SKD-Wet2 and SKD-Wet4, both of composition , as well as between SKD-Wet3 and SKD-18, both of composition $Ce_{0.9}Fe_{3.5}Co_{0.5}Sb_{12}$, as each pair may be examined together because they are the same composition.

Billet Label	Number of Specimens	Type	Relative Density	E (GPa)	G (GPa)	ν
SKD-Wet1	6	n-type, Ce-doped	0.977 ± .002	140.6 ± 0.2	57.34 ± 0.05	0.226 ± .001
SKD-Wet2	8	n-type	0.960 ± .001	137.8 ± 1.2	56.01 ± 0.26	0.231 ± .006
SKD-Wet3	8	p-type	0.956 ± .002	126.8 ± 0.4	51.04 ± 0.30	0.242 ± .011
SKD-Wet4	8	n-type	0.936 ± .002	129.0 ± 0.5	52.28 ± 0.39	0.234 ± .008
SKD-18	7	p-type	0.975 ± .002	131.2 ± 0.6	53.35 ± 0.54	0.230 ± .008

Table 3.5 – Density of specimens. Relative density was calculated by dividing density by the theoretical density of the material from lattice parameter measurements. The theoretical density of n-type material was based on published value of lattice parameter for similar cobalt antimonide materials in literature [Recknagel 2007, Meisner 1998, Caillat 1996, Kraemer 2005]. Theoretical density of p-type material was based on lattice parameter from x-ray diffraction measurement.

Billet Label	Number of Specimens	Type	Density (g/cm^3)	Relative Density
SKD-Wet1	6	n-type, Ce-doped	7.59 ± 0.02	0.977 ± .002
SKD-Wet2	8	n-type	7.45 ± 0.01	0.960 ± .001
SKD-Wet3	8	p-type	7.57 ± 0.02	0.956 ± .002
SKD-Wet4	8	n-type	7.26 ± 0.02	0.936 ± .002
SKD-18	7	p-type	7.73 ± 0.02	0.975 ± .002

For p-type $CeFe_{3-x}Ru_xSb_4$, Ravi published a Young's modulus of 133-139 GPa and a shear modulus of 53.8-54.3 GPa [Ravi 2007]. For p-type $LaFe_4Sb_{12}$, Recknagel published a Young's modulus of 121 $\pm$ 20 GPa [Recknagel 2008]. The Young's modulus of the p-type skutterudite in this study was between 126.8 and 131.2 GPa, in between the values reported by Ravi and Reckangel [Schmidt 2010].

3.3.2 Room Temperature Elastic moduli as a function of porosity

The billets SKD-Wet2 and SKD-Wet4 had the same composition ($Co_{0.95}Pd_{0.05}Te_{0.05}Sb_3$), but different porosities (Table 3.5). The porosity was first noted to be linearly related to the elastic moduli when the shear modulus was plotted as a function of porosity within the billet SKD-Wet4. Within the billet of SKD-Wet4, the modulus varied (Figure 3.16 and 3.17), especially the shear modulus. When the linear function of porosity dependent shear modulus was extended from SKD-Wet4 to the same porosity as SKD-Wet2, the measurements from SKD-Wet2 continued to followed the same trend line (Figure 3.17).

After the shear modulus of SKD-Wet2 was noted to follow a linear trend with porosity, both the Young's modulus and shear modulus were fitted to an empirical formula as described by Rice [Rice 1998]. Rice noted an empirical relationship for elastic moduli and porosity that is approximately linear for small ranges of porosity [Rice 1998]. The modulus as a function of porosity can be fitted to the general form of Equation 3.1,

$$A=A_0\exp(-bP) \qquad \text{(Equation 3.1)}$$

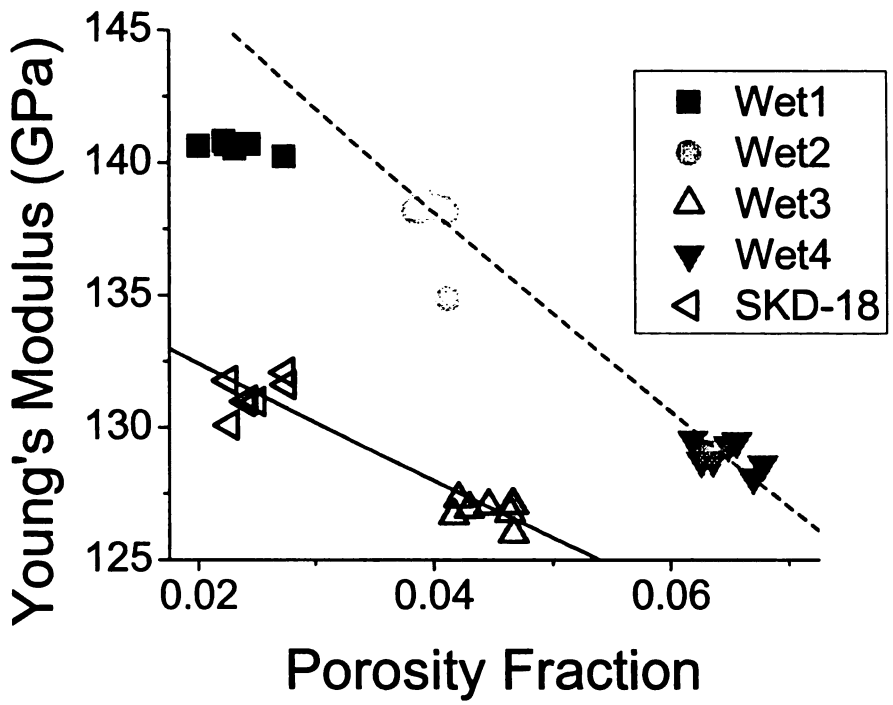

Figure 3.16 – The porosity dependence of Young's modulus. The porosity dependence of the p-type skutterudite (open symbols) and n-type skutterudite without cerium dopant is shown with the porosity relation fitted. Note SKD-Wet1, the n-type with cerium dopant (filled square), falls below the relationship line for the non-cerium doped specimens.

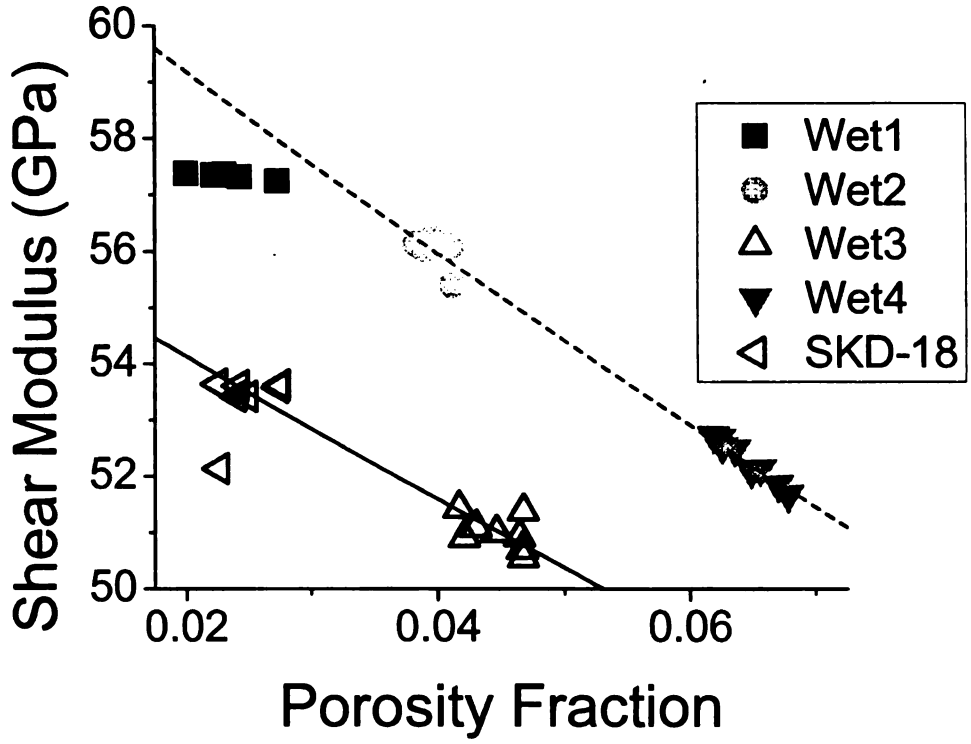

Figure 3.17 – The porosity dependence of the shear modulus. The porosity dependence of the p-type skutterudite, $Ce_{0.9}Fe_{3.5}Co_{0.5}Sb_{12}$, (open symbols) and n-type skutterudite without cerium dopant is shown with the porosity relation fitted. Note SKD-Wet1, the n-type with cerium dopant (filled square), falls below the relationship line for the non-cerium doped specimens.

Table 3.6 – Porosity relationship parameters for the skutterudite materials. These parameters are the fitting parameters for the elastic moduli to porosity relationship equation, $A = A_0 \exp(-bP)$, where A is the parameter to be fitted (Young's modulus, E, or shear modulus, G), A_0 is the theoretically dense value for the modulus, P is the volume percent porosity, and b is an experimentally determined fitting constant [Rice 1998].

Parameters	**Non-cerium doped n-type Constants**	**p-type Constants**
E_0	154.5 GPa	137 GPa
b(E)	2.8	1.7
G_0	62.6 GPa	56.8 GPa
b(G)	2.8	2.4

where A is the shear or Young's modulus at porosity P, P is the volume fraction porosity between 0 and 1 with 0 corresponding to fully dense, A_0 is the modulus at fully dense, and b is the experimentally derived fitting factor [Rice 1998]. The porosity dependent modulus equation has been shown empirically to describe the elastic modulus behavior for several ceramic materials [Rice 1998] and has been used to fit to the results of room temperature elastic moduli of the skutterudite materials in this study (Figures 3.16 and 3.17, Table 3.6).

For n-type skutterudite material without cerium, $Co_{0.95}Pd_{0.05}Te_{0.05}Sb_3$, fitting the porosity relationship of Equation 3.1 [Rice 1998], the fully dense Young's modulus of SKD-Wet2 and SKD-Wet4 was 154.5 GPa. Similarly, the fully dense shear modulus was 62.6 GPa. Both had a fitting factor, b, of 2.8 (Table 3.6). All specimens were within 0.04 to 0.07 volume fraction porosity and, although the fully dense moduli were extrapolations, the relationship was not tested beyond 0.04 to 0.07 volume fraction porosity.

For p-type material, $Ce_{0.9}Fe_{3.5}Co_{0.5}Sb_{12}$, the porosity relationship of the Young's and shear moduli was determine from the room temperature moduli of SKD-Wet3 and SKD-18. The fully dense Young's modulus was 137.0 GPa and the fully dense shear modulus was 56.8 GPa (Table 3.6). As with the n-type, the fully dense moduli were extrapolated, and moduli data beyond 0.02 to 0.05 volume fraction porosity were untested.

The elastic moduli for the cerium doped n-type skutterudite, SKD-Wet1, was less than the porosity relationship function for non-cerium doped (Figures 3.16 and 3.17). No mechanism was observed to be directly responsible for the reduction in modulus in the

cerium doped specimen. In other similar skutterudite materials, the addition of a misch-metal dopant resulted in a distortion of the lattice [Yang 2007]. Applying the assertion of Yang et al., the addition of the cerium dopant distorts the lattice [Yang 2007] and the lattice distortion may, in turn, be related to at least part of the change in the elastic moduli. A second explanation for the change in moduli is the precipitation of small quantities of additional phases, as evidenced by weak peaks of $CoSb_2$ observed in X-ray diffraction pattern [Schmidt 2010]. Future study would be required to determine the cause of modulus change.

An elastic modulus-porosity relationship is not available for the Ce-doped n-type skutterudite or the p-type skutterudite, since the elasticity data is known for only the restricted volume fraction porosity range from P = 0.972 to P = 0.979. Comparing with Equation 3.1 for the non-Ce-doped specimens (Table 3.6), the addition of cerium reduced moduli from the expected moduli of non-cerium doped at the same porosity. The Young's and shear moduli were measured as 140.6 GPa and 57.34 GPa, lower than the non-cerium doped by 4.2 GPa and 1.3 GPa, respectively, or 2.9% and 2.2%. According to X-ray diffraction studies, the atomic structure of the cerium doped specimen skutterudite is largely indistinguishable from the non-cerium doped powder except for a few weak peaks corresponding to $CoSb_2$ [Schmidt 2010]. The reduction in elastic moduli may have shifted the elastic modulus-porosity relationship down 2-3% without changing the fitting factor, b, as a result of the addition of 0.1 atomic % cerium, but the relationship was not determined.

Table 3.7 – Nanoindentation results for Young's moduli. For all specimens, Poisson's ratio was assumed as indicated to allow calculation of Young's modulus on unloading. For SKD-Wet1 and SKD-Wet2, three mutually orthogonal sides were indented to verify the specimens as isotropic, regardless of the direction of pressure during hot pressing. No significant anisotropy was noted. Before each batch of indentations were attempted, a standard aluminum specimen was indented to verify the consistency of the measurement and as a method to clean the indenter tip of debris. Results for SKD-Wet1, SKD-Wet2 and aluminum previously reported by Schmidt et al. [Schmidt 2010].

Billet Label	Number of Indentations	Type	Density (g/cm^3)	Relative density	In pressing direction	E (GPa)	ν
SKD-Wet1	22	n-type	7.59	0.977	No	154.7 ± 1.2	0.23
SKD-Wet1	20	n-type	7.59	0.977	No	153.1 ± 1.9	0.23
SKD-Wet1	21	n-type	7.59	0.977	Yes	149.8 ± 2.2	0.23
SKD-Wet2	18	n-type	7.45	0.960	No	151.0 ± 2.6	0.23
SKD-Wet2	16	n-type	7.45	0.960	No	147.5 ± 3.2	0.23
SKD-Wet2	20	n-type	7.45	0.960	Yes	139.4 ± 2.5	0.23
Al 6061 Test 1	16	Metal	2.69	0.998	Not applicable	81.0 ± 2.1	0.33
Al 6061 Test 2	16	Metal	2.69	0.998	Not applicable	81.9 ± 1.8	0.33
Al 6061 Test 3	14	Metal	2.69	0.998	Not applicable	82.0 ± 2.0	0.33
Al 6061 Test 4	15	Metal	2.69	0.998	Not applicable	83.3 ± 2.4	0.33

3.3.3 Room Temperature Elastic moduli by nanoindentation

Young's moduli values were measured by nanoindentation on a specimen each of SKD-Wet1 and SKD-Wet2 (Table 3.7). To calculate a Young's modulus from the unloading behavior using the Oliver-Pharr method, a Poisson's ratio of 0.23 was assumed. The choice of the assumed Poisson's ratio was based upon an average value of Poisson's ratio determined by RUS (Table 3.4) [Schmidt 2010, Oliver 1992]. A minimum of 20 indentations were attempted per surface, with 16 in a 4 x 4 grid separated by 50 μm and 4 or more added manually outside the grid. Invalid indentations may be caused by external vibrations in the building, or the indenter contacting the specimen surface on a pore or crack, and these invalid indentations were disregarded. The indentations of SKD-Wet1 and SKD-Wet2 on 3 mutually orthogonal surfaces did not exhibit significant anisotropy [Schmidt 2010]. The moduli of SKD-Wet1 and SKD-Wet2 averaged about 8% higher than those determined by RUS [Schmidt 2010].

Young's modulus by nanoindentation was higher than the value determined by RUS. Radovic et al. demonstrated that nanoindentation to determine Young's moduli for alumina, among other materials, was higher than Young's modulus determined by RUS, likely due in part to porosity differences, but lower than theoretically dense Young's modulus [Radovic 2004]. Comparing the Young's modulus of SKD-Wet2 by nanoindentation (Table 3.7) to the theoretically dense Young's modulus of the same material (Table 3.6), the theoretically dense Young's modulus was about 6% higher than the average by nanoindentation. Radovic et al. stated the value of Young's modulus by nanoindentation in alumina was near the theoretically dense value when the indenter was

not influenced by nearby porosity and lower than theoretically dense when the indenter was near porosity, with the general result that Young's modulus determined by nanoindentation was between a minimum of the bulk Young's modulus determined by RUS and the theoretically dense Young's modulus [Radovic 2004]. The Young's modulus value determined by nanoindentation for the skutterudite material in this study was bracketed by the theoretically dense value at the high end and the bulk value by RUS at the low end, as predicted by Radovic et al. for alumina [Radovic 2004].

The MTS nanoindenter XP at Michigan State University used in this study has been used in a previous study of lead telluride-based thermoelectric materials [Ren 2009]. In the previous study by Ren et al., nanoindentations of aluminum alloy Al6061 gave H values of 85.5 ± 1.8 GPa [Ren 2009], as compared to H values of 82.0 ± 2.2 GPa measured on the same aluminum alloy, Al6061, in this study [Schmidt 2010]. The consistent values provide greater confidence in consistent results of the modulus measurement in this study.

3.4 Coefficient of Thermal Expansion by Bulk Measurement

For the skutterudite materials in this study, the coefficient of thermal expansion (CTE) was measured by TMA for four bulk specimens (Table 3.8). The CTE for the p-type material, $Ce_{0.9}Fe_{3.5}Co_{0.5}Sb_{12}$, was measured by both X-ray diffraction of the powder (see section 3.5 for detailed X-ray diffraction result) and TMA of the hot pressed bulk. As expected, the CTE measurement performed by TMA and X-ray diffraction agreed closely, as the thermal expansion is normally not a function of porosity for most ceramic materials [Rice 1998]. All specimens that were heated above 573 K began showing an increased rate of thermal expansion above a point between 573 K and 723 K that was not recovered upon cooling. The specimens heated above 573 K lengthened on progressive thermal cycles, with the greatest length change after the initial cycle (Figures 3.18 through 3.21).

The thermal expansion of each of the four billets hot pressed from wet milled powders were measured with a thermomechanical analyzer (TMA) at the High Temperature Materials Laboratory at Oak Ridge National Laboratories.

Each specimen had a nearly constant rate thermal expansion from room temperature through 573 K or greater, increasing by 20% or less (Figures 3.18 through 3.21, Table 3.8). The CTE versus temperature behavior for specimens SKD-Wet1-B and SKD-Wet2-B changed to non-linear at approximately 723 K. To calculate the thermal expansion rate of SKD-Wet1-B and SKD-Wet2-B, the temperature range was truncated to include only the linear range of 323 K to 698 K. The average coefficient of thermal

Table 3.8 – Average Coefficient of Thermal Expansion (CTE) for four different specimens by bulk measurement in the TMA machine. The measured CTE was different for SKD-Wet2-B and SKD-Wet4-B due to a different range in temperature, as the CTE increases with temperature.

Specimen	Type	Thermal expansion coefficient (K^{-1})	Temperature Range (K)	Heating Rate (K/min)	Number of cycles
SKD-Wet1-B	n-type, Ce-doped	11.6×10^{-6}	323-698	3	5
SKD-Wet2-B	n-type	10.2×10^{-6}	323-698	1.5	2
SKD-Wet3-J	p-type	13.0×10^{-6}	303-573	1.5	3
SKD-Wet4-B	n-type	9.8×10^{-6}	303-573	1.5	4

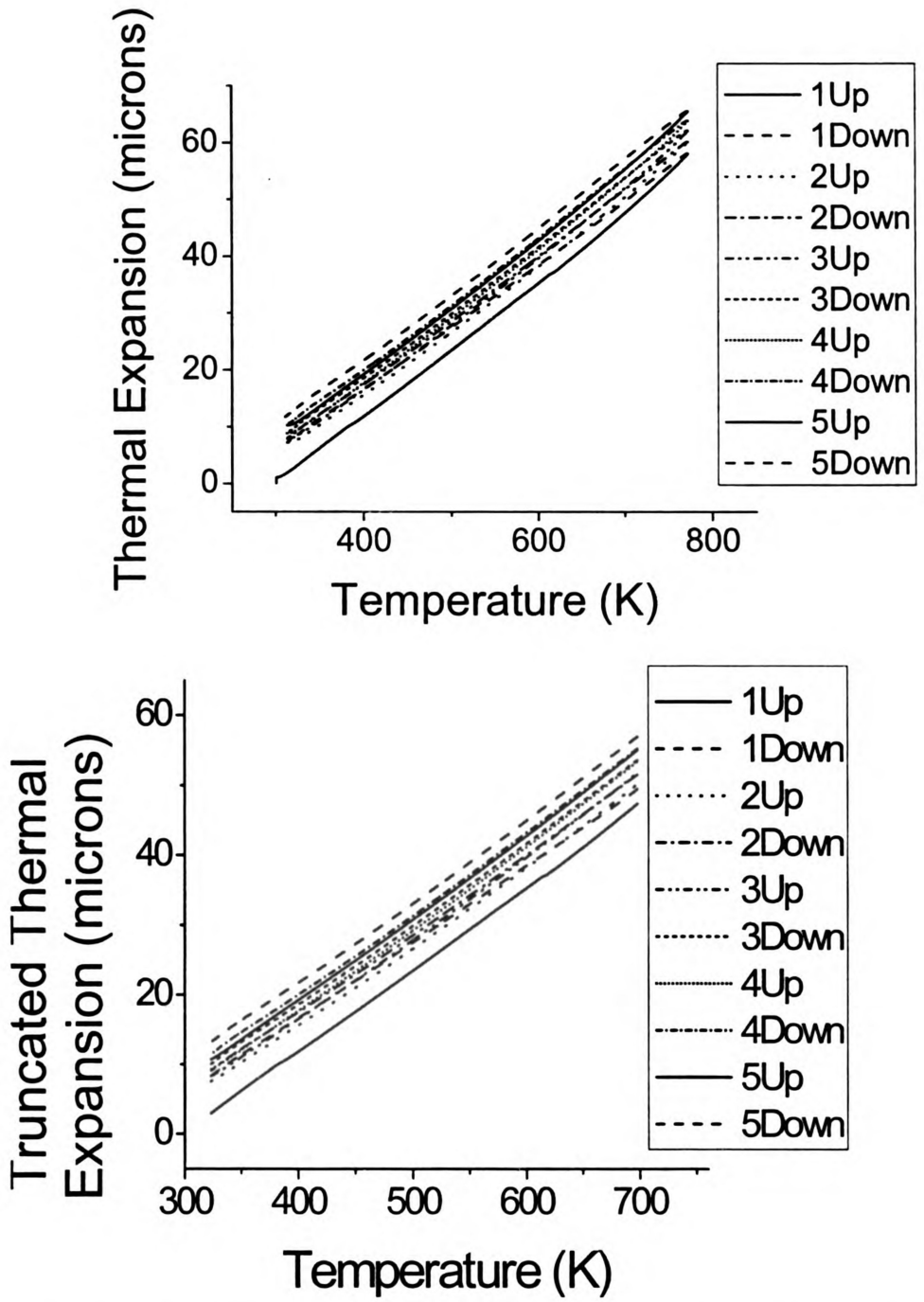

Figure 3.18 – The thermal expansion measurement for specimen SKD-Wet1B, nominally 5 x 7 x 10 mm. The thermal expansion rate was consistent between cycles except above 723 K, where the specimen expanded at a faster rate on heating but not upon cooling, growing between 1 and 3 μm each cycle.

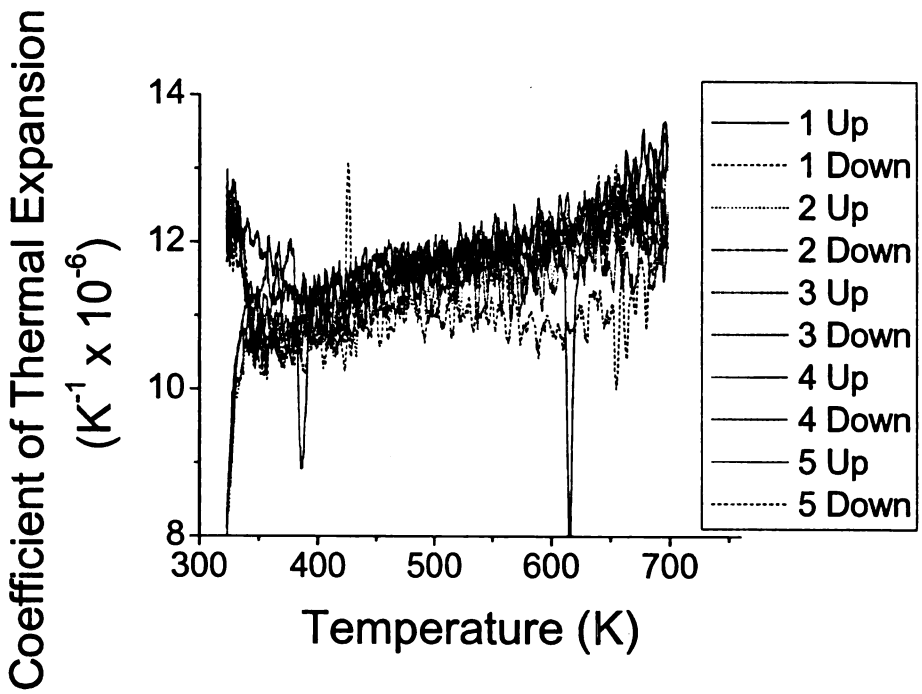

Figure 3.18 (continued)

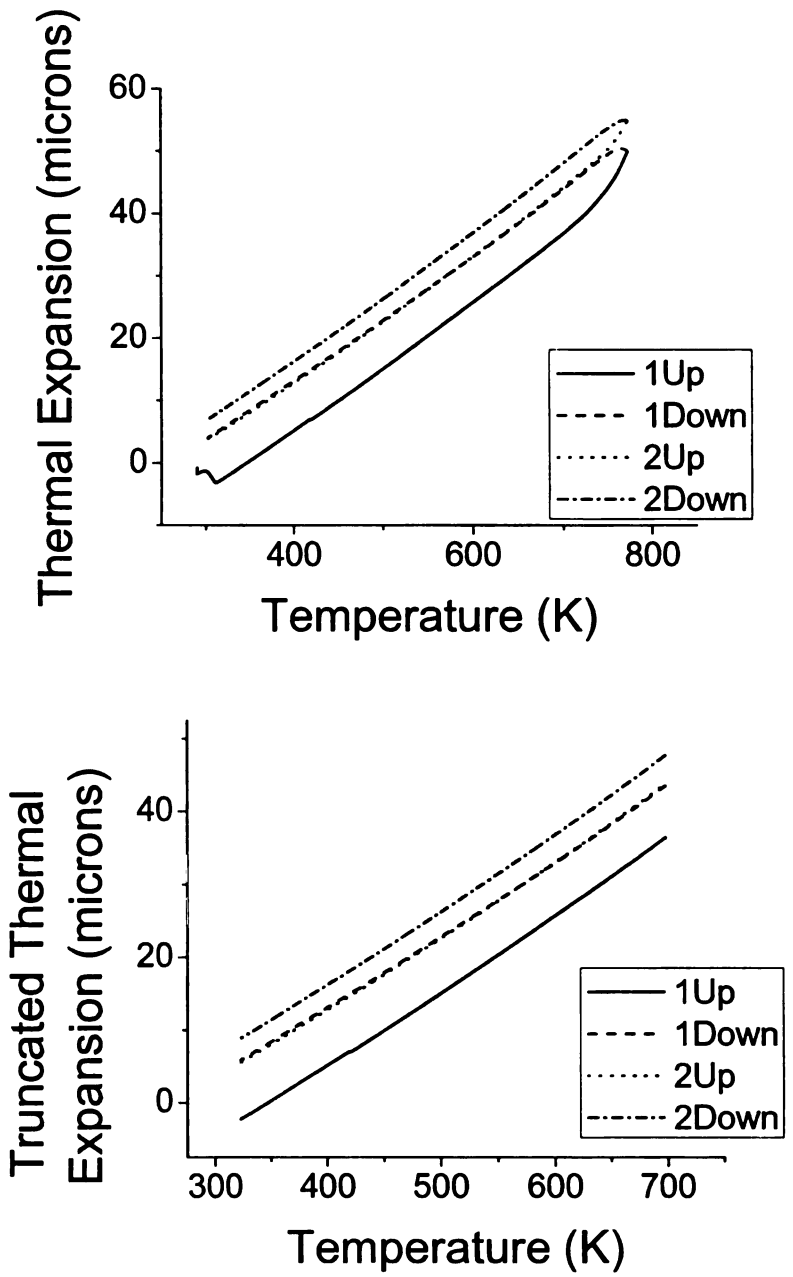

Figure 3.19 – The thermal expansion measurement for specimen SKD-Wet2B, nominally 5 x 7 x 10 mm. Due to the changes in SKD-Wet1B, the specimen SKD-Wet2B was cycled at a slower rate of 1.5 K per minute to more accurately observe any changes, resulting in fewer cycles. The thermal expansion rate was consistent between cycles except above 723 K, where the specimen expanded at a faster rate on heating but not upon cooling, growing between 3 and 8 μm each cycle.

Figur

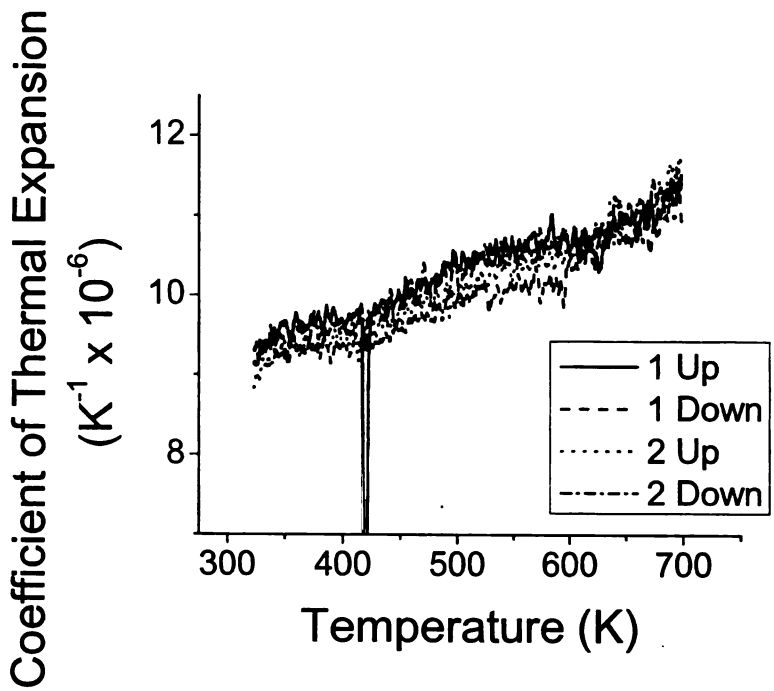

Figure 3.19 (continued)

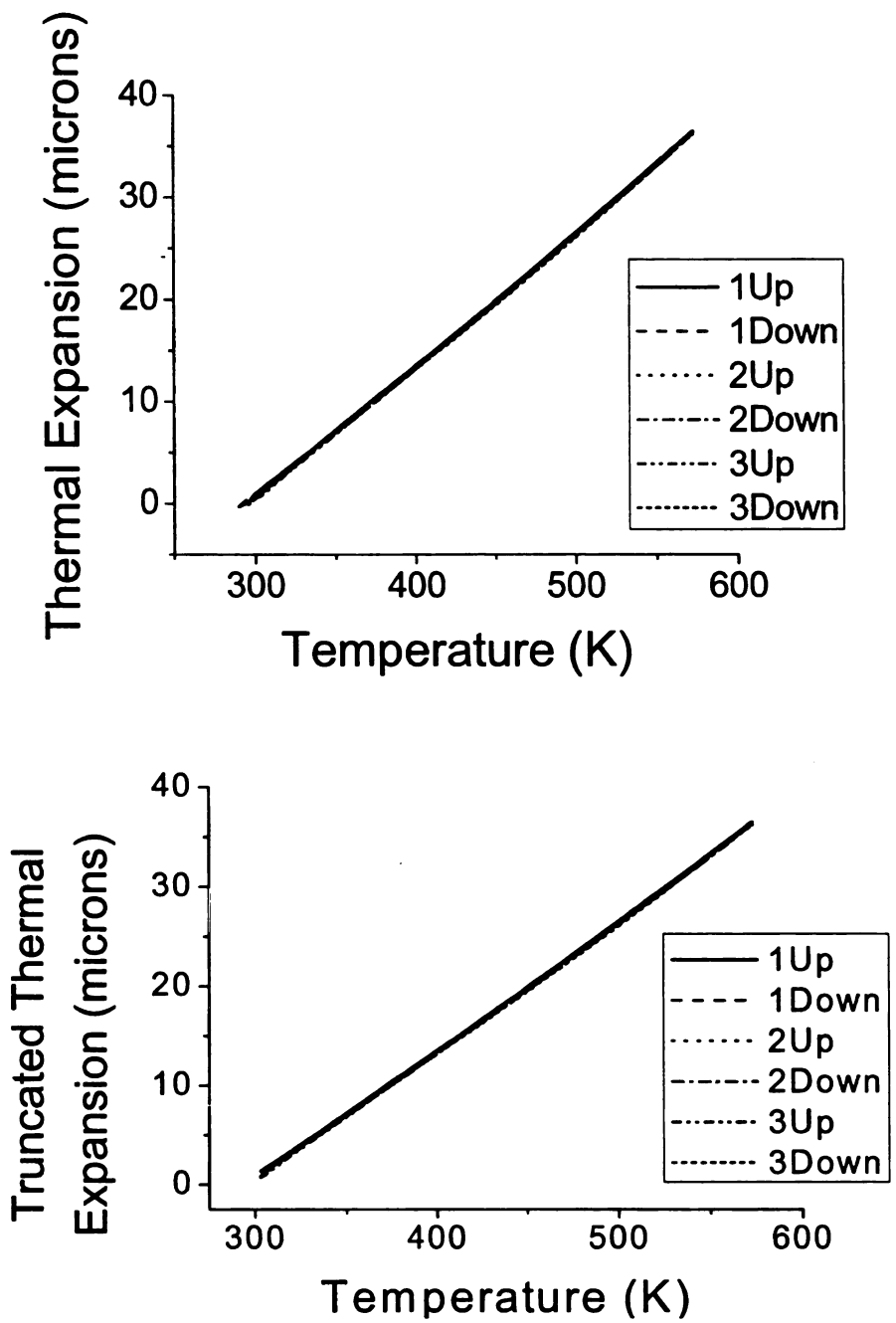

Figure 3.20 – The thermal expansion measurement for specimen SKD-Wet3J, composition $Ce_{0.9}Fe_{3.5}Co_{0.5}Sb_{12}$, nominally 5 x 7 x 10 mm. The thermal expansion rate was measured to 573 K in an effort to minimize any new phase development as was observed by X-ray above 573 K. The resulting cycling was the most consistent of all runs between cycles, shrinking by less than 0.4 μm over the entire test.

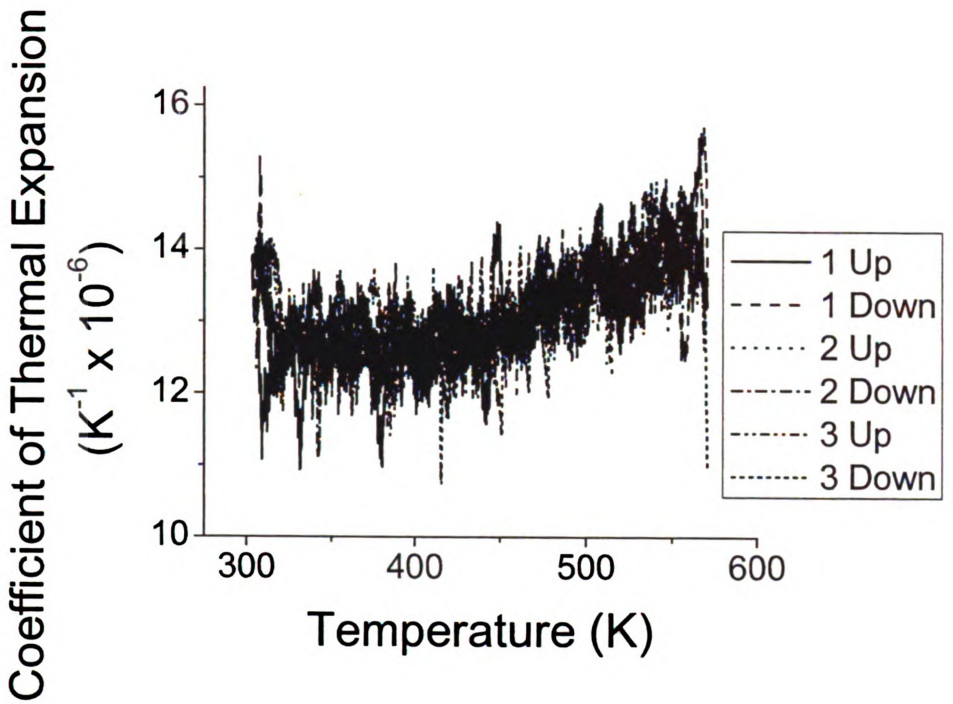

Figure 3.20 (continued)

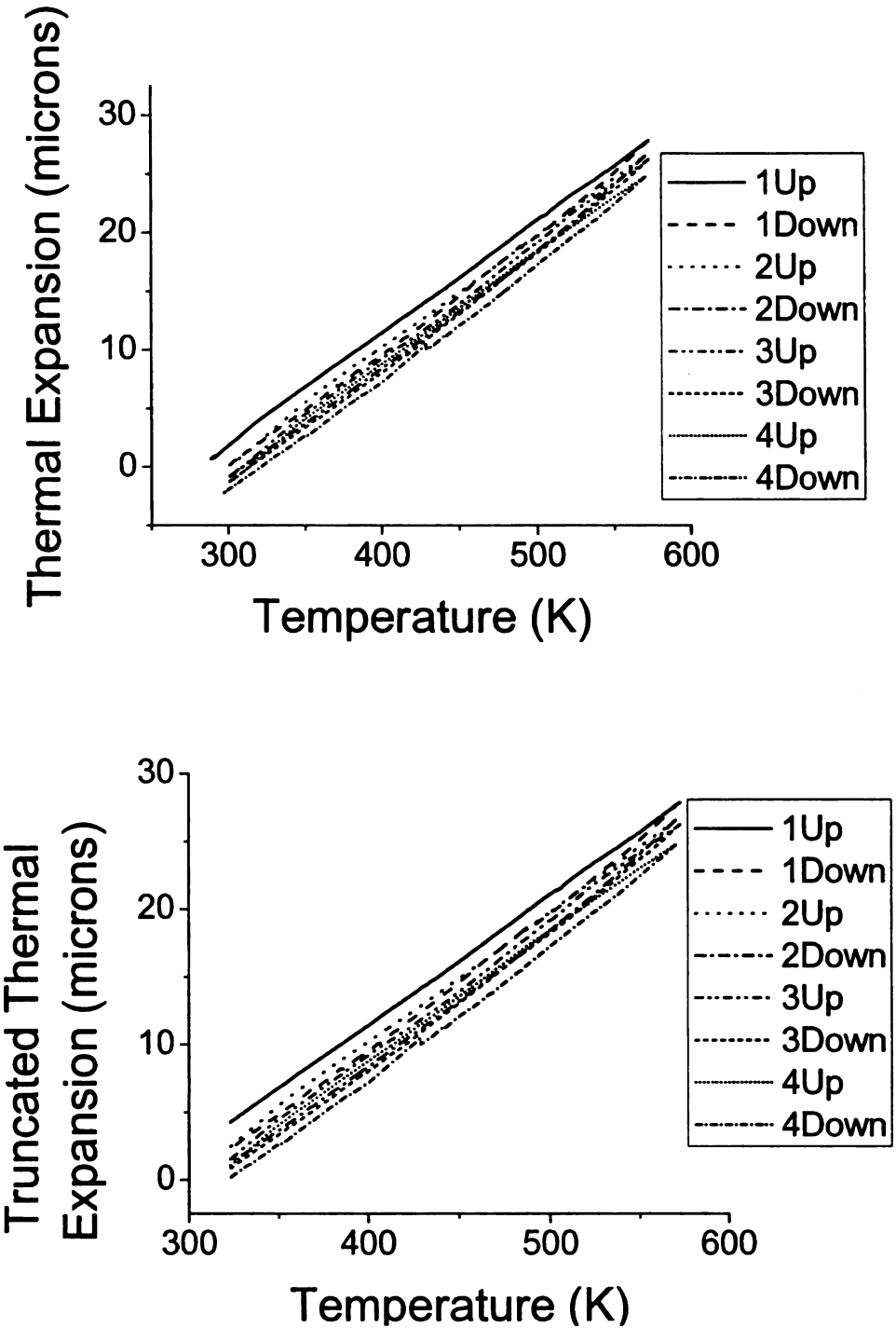

Figure 3.21 – The thermal expansion measurement for specimen SKD-Wet4B, nominally 5 x 7 x 10 mm. The thermal expansion rate was measured to 573 K in an effort to minimize large thermal expansions during heating above 573 K. Several jogs were noted, particularly during the cooling segment of tests, where the measured length suddenly grew.

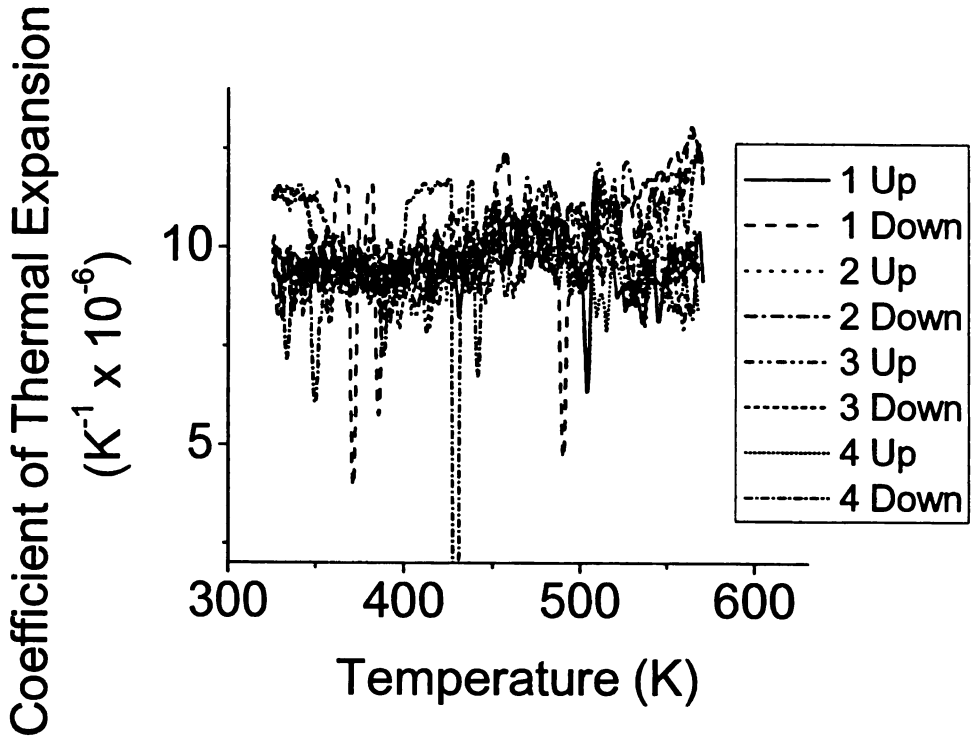

Figure 3.21 (continued)

Table 3.9 – Strain between thermal cycles during thermal expansion measurement for specimen SKD-Wet1B. The strain was evaluated between cycles at 373 K.

Heating Cycle	Length at 373K (mm)	Strain (μm/m)
1	9.991418	
2	9.995232	382.1
3	9.996006	77.5
4	9.997155	115.1
5	9.998671	151.9

Cooling Cycle	Length at 373K (mm)	Strain (μm/m)
1	9.996277	
2	9.997110	83.4
3	9.998116	100.8
4	9.999556	144.2
5	10.00129	173.5

Table 3.10 – Strain between thermal cycles during thermal expansion measurement for specimen SKD-Wet2B. The strain was evaluated between cycles at 373 K.

Heating Cycle	Length at 373K (mm)	Strain (μm/m)
1	10.05581	
2	10.06353	767.8

Cooling Cycle	Length at 373K (mm)	Strain (μm/m)
1	10.06388	
2	10.06693	303.5

Table 3.11 – Strain between thermal cycles during thermal expansion measurement for specimen SKD-Wet3J, composition $Ce_{0.9}Fe_{3.5}Co_{0.5}Sb_{12}$. The strain was evaluated between cycles at 373 K.

Heating Cycle	Length at 373K (mm)	Strain (μm/m)
1	9.99265	
2	9.99231	-34.27
3	9.99230	-0.81

Cooling Cycle	Length at 373K (mm)	Strain (μm/m)
1	9.99249	
2	9.99236	-13.46
3	9.99229	-6.93

Table 3.12 – Strain between thermal cycles during thermal expansion measurement for specimen SKD-Wet4B. The strain was evaluated between cycles at 373 K.

Heating Cycle	Length at 373K (mm)	Strain (μm/m)
1	9.982832	
2	9.981646	-118.9
3	9.980565	-108.4
4	9.980175	-39.1

Cooling Cycle	Length at 373K (mm)	Strain (μm/m)
1	9.980877	
2	9.979734	-114. 6
3	9.979373	-36.2
4	9.978670	-70.4

expansion of each specimen was determined by linear regression for the truncated temperature region.

The specimen SKD-Wet1-B transitioned to an increased rate of thermal expansion on heating at approximately 723 K (Figure 3.18). The increased rate of thermal expansion did not recover upon cooling, producing a permanent increase in length following each thermal cycle. The length increase after the first thermal cycle (Table 3.8) was the largest observed increase. The coefficient of thermal expansion increased by about 14% over the truncated temperature range.

The specimen SKD-Wet2-B increased in thermal expansion at a similar temperature as SKD-Wet1-B (Figure 3.19). For the experiment on SKD-Wet2-B, the heating and cooling rate was halved to determine if a possible lag in response, or other rate-dependent variable, changed the increase in length per thermal cycle. The general behavior of increasing thermal expansion around 723 K, particularly on the first thermal cycle, remained unchanged (Table 3.9). With the slower heating and cooling rate of 1.5 K/minute, only 2 heating and cooling thermal cycles were completed. Despite completing only 2 thermal cycles, a thermal expansion rate was determined for a truncated temperature range, excluding the temperature region where the thermal expansion was nonlinear. Through the truncated temperature range of 323 K to 698 K, the coefficient of thermal expansion increased by about 20%.

The thermal expansion of SKD-Wet3-J was measured to a maximum temperature of 573 K. The high temperature limit on temperature was chosen (i) to stay in the linear region observed during high temperature RUS on SKD-Wet3, where a change in modulus behavior occcured at about 673 K, (ii) based on thermal expansion rate changes in

previous specimens, observed above about 723 K for SKD-Wet1 and SKD-Wet2, and (iii) to remain below the temperature at which new peaks were observed in X-ray diffraction, 603K. All three thermal cycles of SKD-Wet3-J produced repeatable results with no significant change between thermal cycles (Figure 3.20, Table 3.10). The coefficient of thermal expansion increased by about 8% with increasing temperature from room temperature to 573 K.

Thermal expansion measurements of SKD-Wet4-B were taken between room temperature and 573 K (Figure 3.21) The temperature range was chosen for (i) consistency with the measurement of SKD-Wet3 and (ii) minimizing non-linear behavior above 573K. The SKD-Wet4-B specimen was of the same composition as SKD-Wet2-B, $Co_{0.95}Pd_{0.05}Te_{0.05}Sb_3$, and the differences observed in the average coefficient of thermal expansion (Table 3.10) were largely a result of the lower temperature range observed.

The expansion behavior of specimens SKD-Wet1 and SKD-Wet2 on successive thermal cycles was not unique to skutterudite material. Irreversible specimen expansion on successive heating and cooling thermal cycles was observed by Thakur et al. on magnesium alloy-based hybrid composites [Thakur 2004]. Successive thermal cycles increased the length of the composite, particularly on the initial thermal cycle. After cycling two composite specimens, an initial strain of 620 μm/m and 730 μm/m reduced to 110 and 50 by the 10^{th} thermal cycle [Thakur 2004]. Thakur et al. attribute the irreversible thermal expansion to the release of stress between the different composite materials, particularly at the boundary of the matrix and reinforcement, and the formation of stable precipitates reduced the strain on successive thermal cycles [Thakur 2004].

For the skutterudite materials included in this study, Thakur et al.'s [Thakur 2004] explanations are not adequate or complete enough to explain the expansion behavior. First, there is no reinforcement material to create stresses. Secondly, while some new phase may be forming at higher temperatures, there is no reinforcement to stabilize. A new phase has been observed in the p-type powder in X-ray diffraction to occur, which may account for a portion of the irreversible length change, but not in the method described by Thakur et al. [Thakur 2004]. Alternative explanations advanced by Thakur et al. include damage saturation from thermal cycling and the formation of higher dislocation density [Thakur 2004]. For the skutterudite materials included in this study, identifying the cause of the irreversible component of the progressive thermal expansion is an area for further research.

Each measurement of thermal expansion included more than one discontinuous change in slope, easily observed as a spike in the coefficient of thermal expansion (Figures 3.18 through 3.21). The discontinuities occurred most frequently on SKD-Wet4-B, and with repetition between thermal cycles at a given temperature (Figure 3.21). The same type of discontinuous slope changes also occurred on control tests of alumina, but the temperature at which the discontinuity occurred was not repeatable when tested a second time (Figures 3.22 through 3.24) The majority of discontinuous length changes reoccurred at about the same temperature during successive thermal cycles of a single test. For example, from the September 2009 alumina test, one of the discontinuities occurred at about 550 K on every cooling half cycle (Figure 3.24).

For two reasons, the discontinuities were, in part or whole, due to machine error. First, the discontinuities in alumina are not characteristic of the material. Second, the

discontinuities occurred at a consistent temperature within a set of thermal cycles, but changed from test to test. If the material caused the discontinuities, the results should be repeatable on different tests, however the discontinuities either occur at a consistent temperature every test or at more random temperatures across all tests. For these reasons, the discontinuities in CTE as a function of temperature were not considered a real change in the material, but rather a machine-related error.

The thermal expansion rates of 9.8 and 10.2 x 10^{-6} K^{-1} for non cerium doped n-type material and 11.6 x 10^{-6} K^{-1} for cerium doped n-type material compares favorably to a literature measurement of 9.3 to 8.8 x 10^{-6} K^{-1} by Salvador et al. for a similar material, $Yb_xCo_4Sb_{12}$, where x is 0.17, 0.31 or 0.35 [Salvador 2009]. Contrary results from this study and Salvador et al., the coefficient of thermal expansion of $CoSb_3$ was measured by Caillat et al. as 6.36 x 10^{-6} K^{-1} [Caillat 1996].

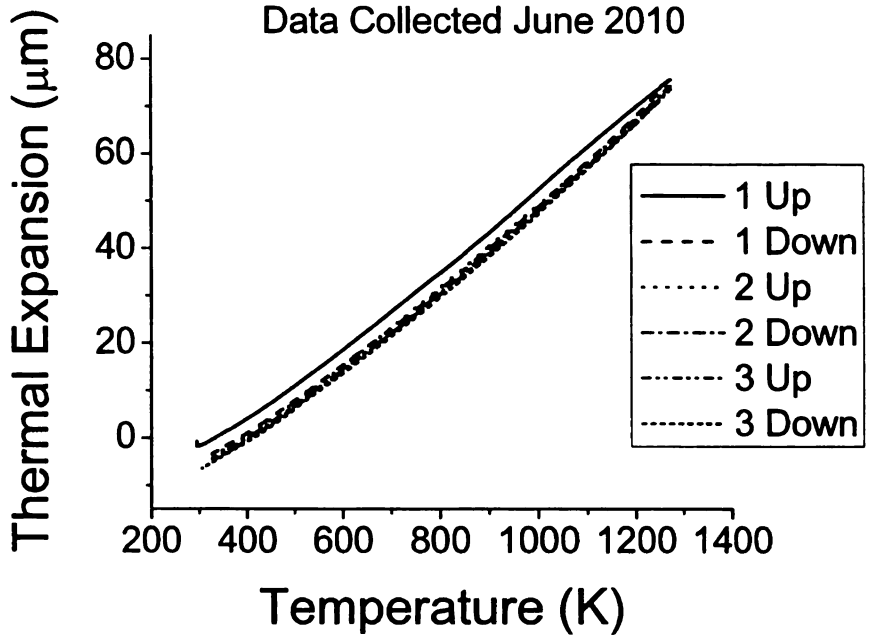

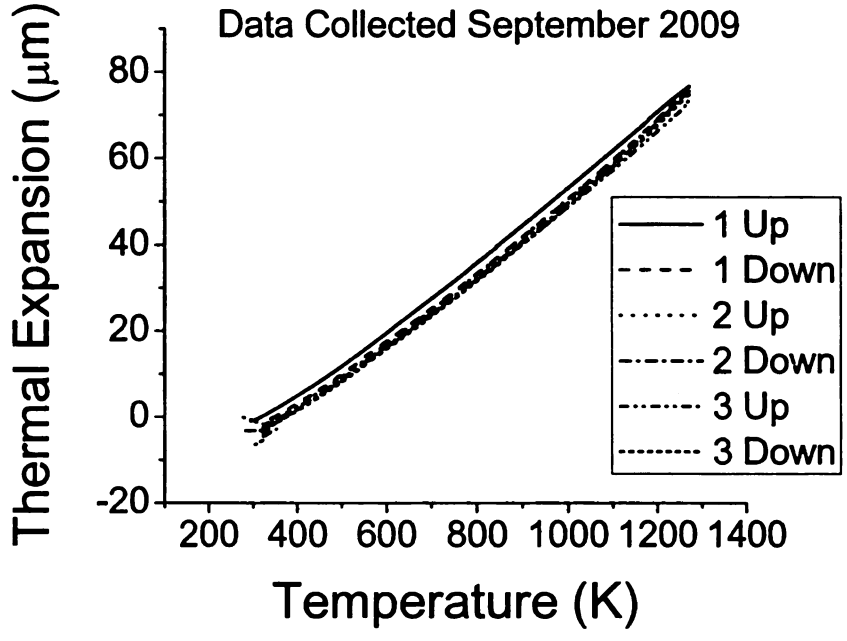

Figure 3.22 – The thermal expansion of alumina, as measured on June 25, 2010 and September 18, 2009. Note jogs within the curve occurring in groups. Often a jog from one heating cycle occurs at nearly the same temperature on all heating cycles. These jogs are not characteristic of alumina, and must be caused by the TMA machine.

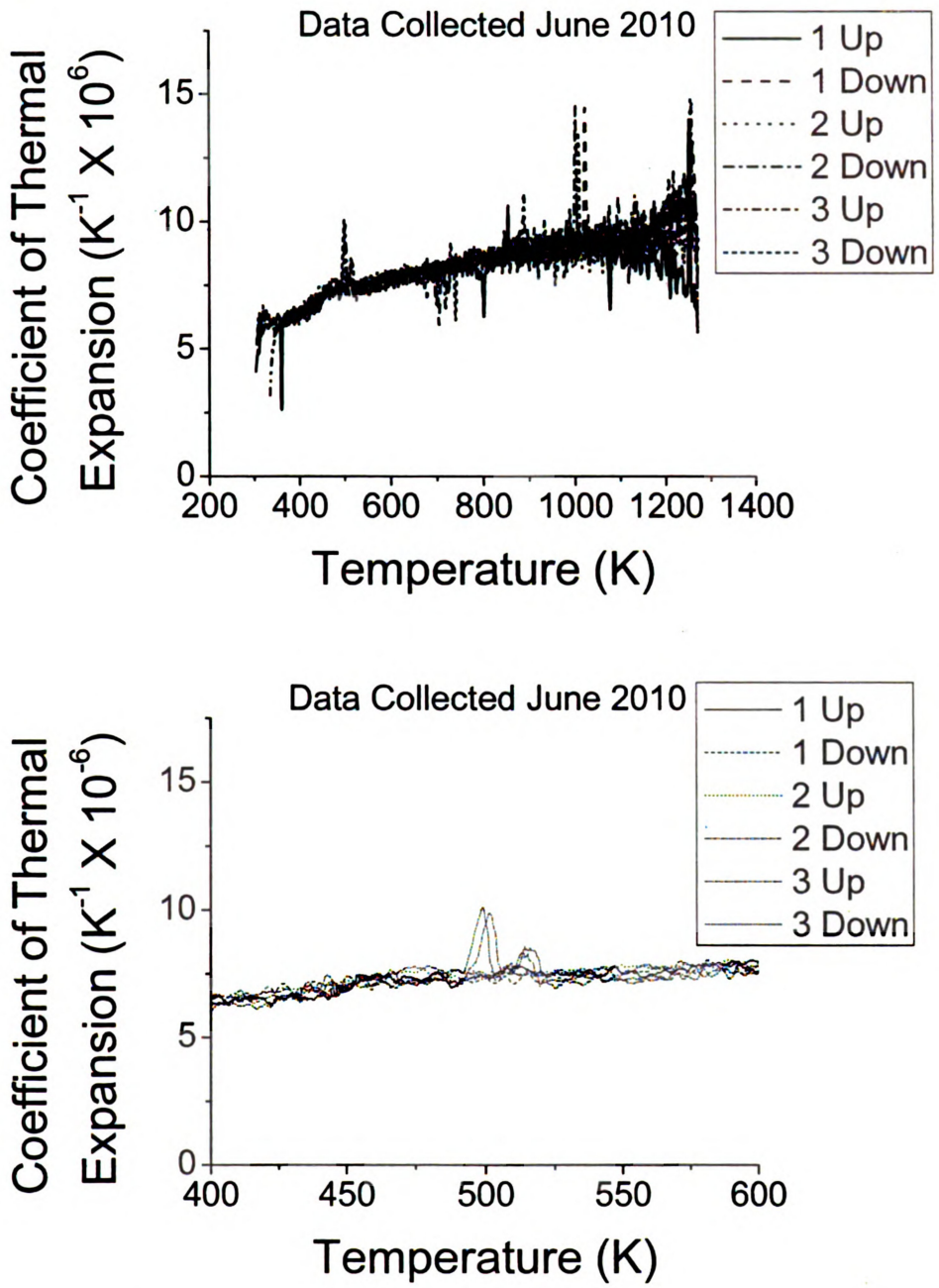

Figure 3.23 – The thermal expansion coefficient for alumina more clearly shows spikes of changing thermal expansion rates, based on small jumps in the measurement data. Many of the spikes reoccur on successive cycles. One example spike at 500K occurs on both cycle 2 Up and cycle 3 Up, with a nearly identical shape and a shift of 3K, indicating they were caused by the same mechanism.

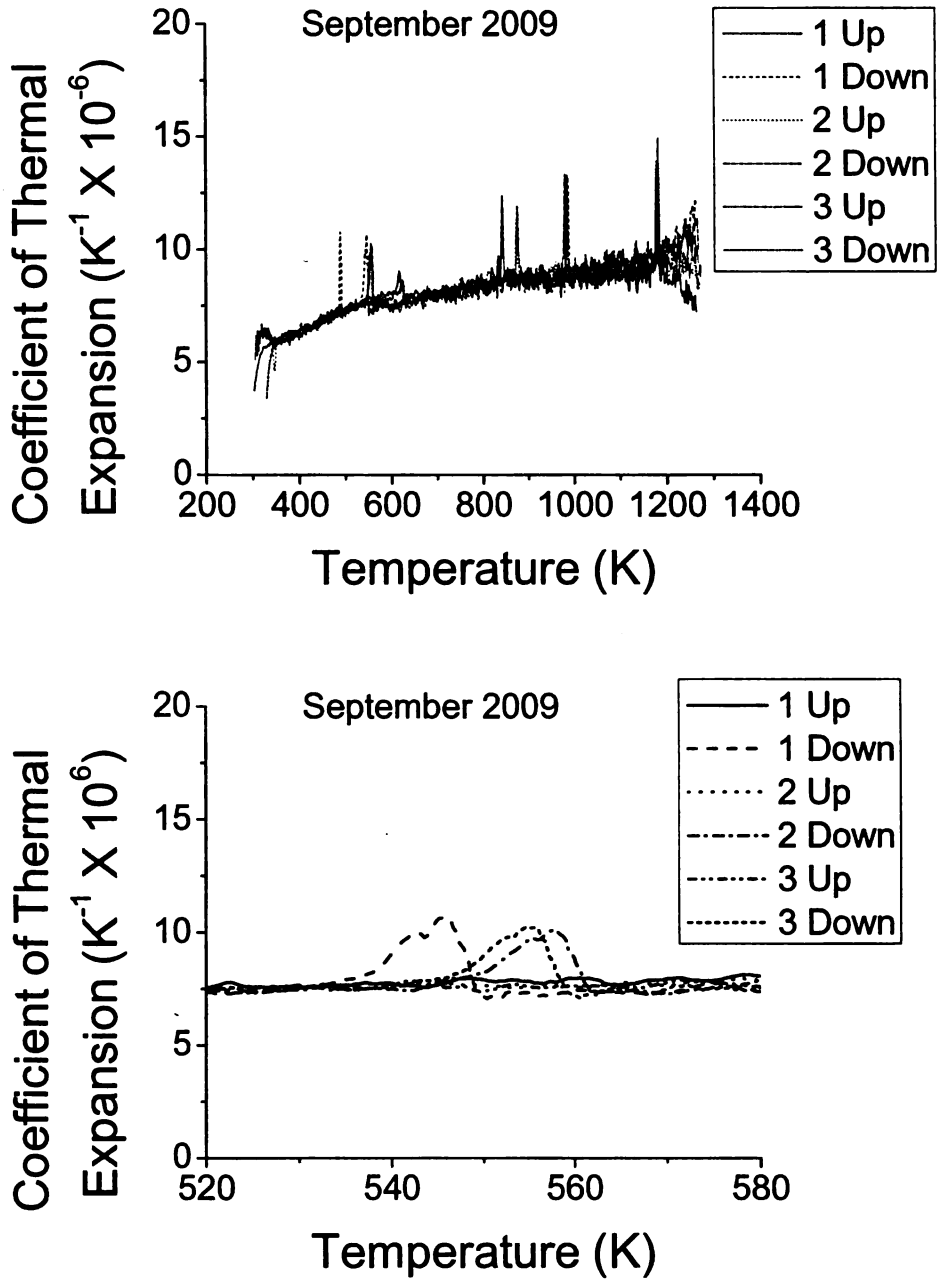

Figure 3.24 – The thermal expansion coefficient for alumina from a second run shows a similar behavior of spikes as occurred in Figure 3.23. The temperature at which the spikes occurred was different, but the behavior of reoccurring on successive cycles within less than 15K separation was consistent, as demonstrated by the reoccurance of one spike around 550K on each cooling cycle. The behavior was consistent with error due to equipment. If the spikes are disregarded as outliers, the general behavior is consistent with expected behavior for alumina.

3.5 Lattice Parameter

The lattice parameter of the p-type skutterudite material, $Ce_{0.9}Fe_{3.5}Co_{0.5}Sb_{12}$, has not been accurately evaluated in previous published work. The lattice parameter of some similar skutterudite material has been measured, such as $LaFe_4Sb_{12}$ [Recknagel 2007], at 0.91487(2) nm.

Using the PANalytical X-ray diffraction (XRD) equipment at the HTML in Oak Ridge National Laboratories (operated by Roberta Peascoe-Meisner and E. Andrew Payzant), the lattice parameter of the p-type skutterudite material was determined between 303 K and 633 K. All the peaks detected matched those for $LaFe_4Sb_{12}$ until two new peaks were detected after heating to 603 K (Figure 3.25). After detection, the two new XRD peaks persisted through the entire cooling cycle. No attempt was made to identify the phase(s) represented by two new peaks that were detected. The new phase did not change the lattice parameter or CTE of the primary skutterudite phase.

The lattice parameter for the p-type skutterudite material was measured as 0.91241 ± 0.00003 nm at 303 K, and increased linearly up to 633 K. Fitting the measured values of the lattice parameter (Table 3.13) to a linear function (Figure 3.26), the slope was used to determine the coefficient of thermal expansion (CTE). The slope of the linear function is the rate of length change of the lattice parameter length, and, by definition, the CTE is the rate of length change per unit length. Therefore, the CTE is the slope divided by the lattice parameter length. Using a least-squares fit of the lattice parameter versus temperature, the slope was determined as 0.00001187 nm/K, and the

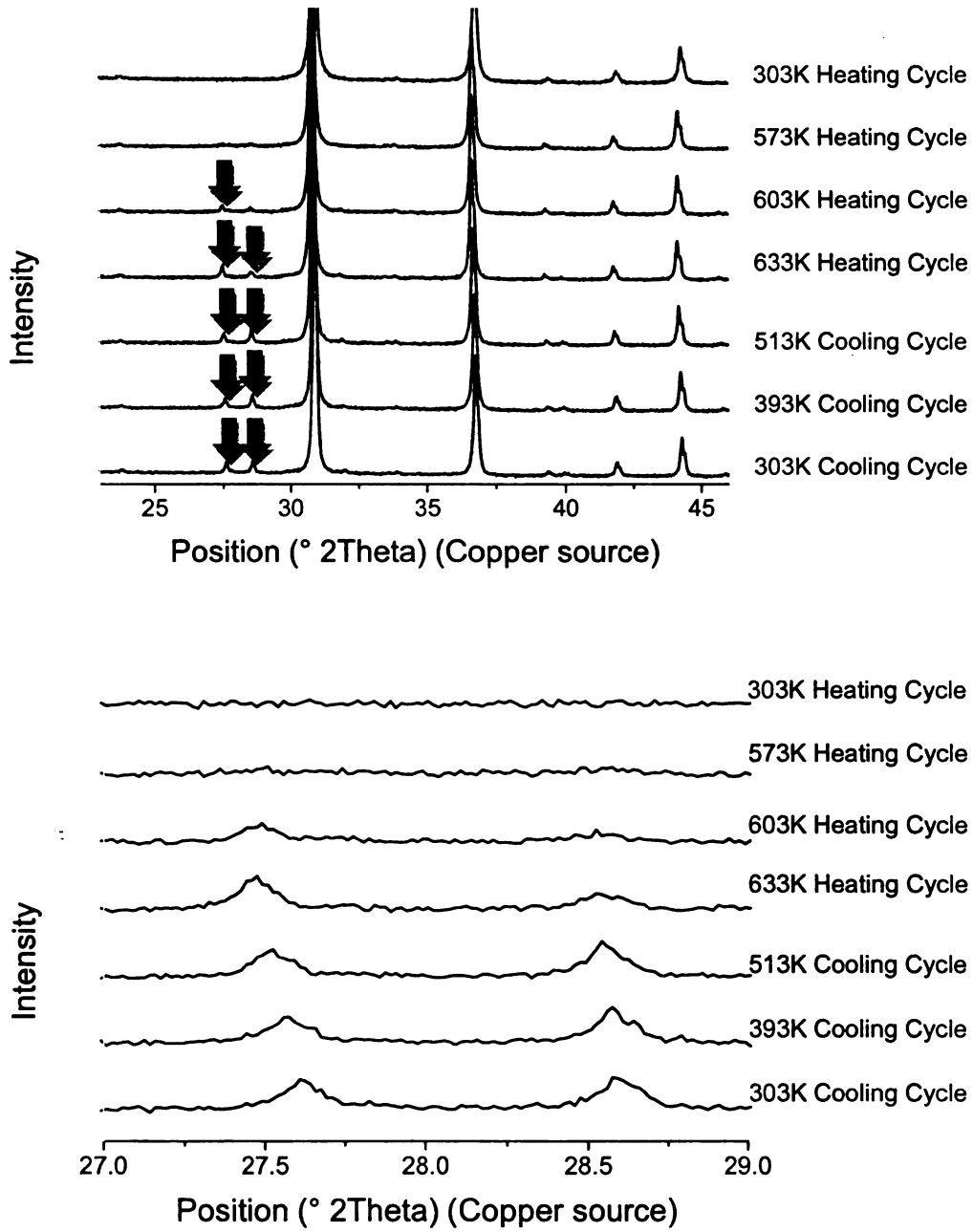

Figure 3.25 – The x-ray diffraction charts of powders of JSpSKD-15, composition $Ce_{0.9}Fe_{3.5}Co_{0.5}Sb_{12}$, show the development of two new peaks between 27° and 29° that were not detected until heating above 573 K. The earliest measurement is at the top and selected measurements in chronological order are visible as moving down. The peaks were not visible until after heating to 573 K, indicating a new phase was growing, beginning around 573 K. The peaks remained when the specimen was cooled back below 573 K, remaining unchanged through all the cooling cycle measurements.

Table 3.13 – Lattice Parameter Measurement of p-type Skutterudite powder specimen, JSp-SKD-15, composition $Ce_{0.9}Fe_{3.5}Co_{0.5}Sb_{12}$. The powder was a sample of the material later pressed into p-SKD-Wet3.

Temperature (K)	Lattice parameter during heating (nm)	Lattice parameter during cooling (nm)
303	0.912431	0.912392
333	0.9128093	0.9127528
363	0.9131402	0.9131128
393	0.9134926	0.9134737
423	0.9138298	0.9138736
453	0.9142037	0.9142023
483	0.914584	0.9145149
513	0.9149294	0.9148895
543	0.915287	0.9152463
573	0.9156438	0.9156098
603	0.9159726	0.9159688
633	0.9163382*	0.9163382*

* The lattice parameter is the same for heating and cooling at 633K, as this was the highest temperature reached.

Figure
$Ce_{0.9}F$
coolin
and 6(

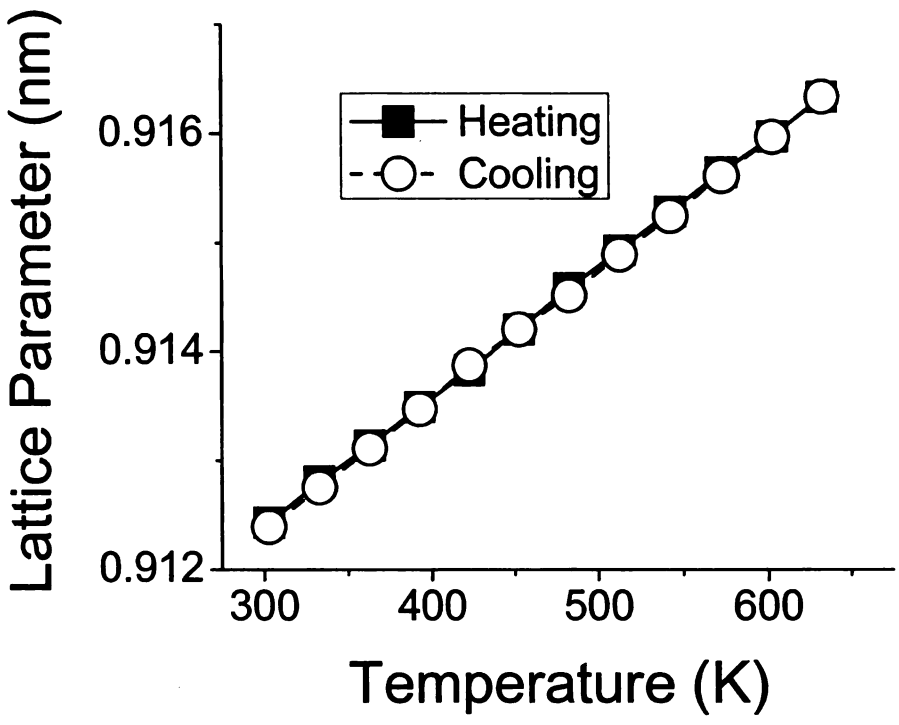

Figure 3.26 – Plot of lattice parameter for p-type powder JSpSKD-15, composition $Ce_{0.9}Fe_{3.5}Co_{0.5}Sb_{12}$, from the powder hot pressed to make SKD-Wet3. The heating and cooling were very linear and consistent, despite the new peaks forming between 573 K and 603 K on heating and remaining during the entire cooling cycle.

CTE

XRI

dete

the

Uni

Co

Jen

Eng

cor

latt

[Re

par

0.9

der

wi

lat

we

do

pe

typ

de

CTE was 13.0 x 10^{-6} K^{-1}. The change in lattice parameter with temperature determined by XRD measurement on powder specimens was consistent with the thermal expansion determined via the TMA for the bulk material (see section 3.4).

The XRD pattern of the n-type, $Co_{0.95}Pd_{0.05}Te_{0.05}Sb_3$, was previously obtained for the Ce-doped specimen by X-ray diffraction by Dr. Rui Huang at Michigan State University Department of Chemistry. Subsequently, the lattice parameter of $Co_{0.95}Pd_{0.05}Te_{0.05}Sb_3$ was analyzed using Jade software (Jade 5, MDI, Livermore, CA) by Jennifer Ni (Graduate Student, Michigan State University, Department of Chemical Engineering and Materials Science). The calculated lattice parameter, 0.904827 nm, was consistent with published values for materials of a similar composition. For example, the lattice parameter of undoped $CoSb_3$ ranged between 0.90345 nm and 0.90385 nm [Recknagel 2007, Meisner 1998, Caillat 1996, Kraemer 2005]. Also, the lattice parameter of $CoSb_{3-x}Te_x$ (x was between 0 and 0.10) was measured as 0.90350 Å to 0.90442 Å [Liu 2007], as determined by Liu et al. The theoretically dense values of density the n-type skutterudite materials were calculated with the same lattice parameter, with the assumption that the 0.1atomic % Ce doping would not appreciably change the lattice parameter. Samples of both Ce-doped and non-Ce-doped skutterudite powders were analyzed by X-ray diffraction. The analysis confirmed both Ce-doped and non-Ce-doped skutterudite powders were substantially the same material structure, with XRD peaks detected at the same 2θ values [Schmidt 2010].

The lattice parameter was used to calculate the theoretical density values of the p-type and n-type materials. For the p-type $Ce_{0.9}Fe_{3.5}Co_{0.5}Sb_{12}$, the calculated theoretical density was 7.9237 g/cm^3, and for the n-type $Co_{0.95}Pd_{0.05}Te_{0.05}Sb_3$, the calculated

theoretical density was 7.7637 g/cm^3. The theoretical density was used to determine volume fraction density and volume fraction porosity for all the specimens tested and the effect of changing the volume fraction porosity on moduli (see section 3.3.2).

3.6 Temperature Dependent Elastic Moduli

The elastic moduli as a function of temperature were measured for each of the four hot pressed skutterudite billets from wet milled powders (Figures 3.27 through 3.30, Appendix B). Every specimen exhibited a linear decrease of Young's and shear moduli with increasing temperature between room temperature and a cutoff temperature, T_{CUTOFF}. Above a cutoff temperature, T_{CUTOFF}, between 523 K and 623 K, the rate of moduli change with temperature increased.

The T_{CUTOFF} marks a change from the linear region to a viscoelastic region. In the higher temperature regime, a viscoelastic region due to grain boundary sliding influences the elastic moduli [Ren 2009]. The acoustic Debye temperature, θ_D, was between 303 and 318 K for each of the four skutterudite specimens (Table 3.14), as calculated by the Anderson approximation [Anderson 1963]. The minimum temperature included in the elasticity testing was 298 K, making the reduced temperature, T_R, 0.9 or greater (where $T_R = \theta_D/T$). The linear region typically begins at $T_R > 0.3$ to 0.5, and a cryogenic region between T = 0 K and T_R [Ren 2009]. All skutterudite specimens were tested above a T_R of 0.5, thus none of the tested specimens were expected to exhibit behavior characteristic of the cryogenic region.

The elastic moduli of SKD-Wet1 decreased linearly from room temperature to 600 K (Figure 3.27). Within the linear region, the Poisson's ratio remained relatively constant at approximately 0.224.

Through the heating of SKD-Wet2, the elastic moduli decreased linearly to approximately 600 K before decreasing at higher temperatures (Figure 3.28). At the

highest temperature reached, 773 K, the moduli diverged from the previously established behavior, with the shear modulus nearly the same as measured at 723 K and the Poisson's ratio dropping about 7% to 0.2288. The outlier at 773 K did not appear to indicate a change in the material that could be seen during cooling. Upon cooling, the moduli largely returned to the same elastic moduli measurements as during heating, with small variations of 0.5% or less.

For specimen SKD-Wet3-K, the thermal cycle of heating and cooling was limited to a maximum temperature of 573 K (Figure 3.29), after a previous attempt to thermal cycle specimen SKD-Wet3-G to 773 K produced RUS spectra that could not be fitted above 673 K. The high temperature was chosen to provide a region largely within the linear region for previous specimens. The smaller temperature range permitted more frequent sampling at 20 K increments. A transition of moduli rate of change was observed at about 523 K, above which the elastic moduli decreased at a faster rate with temperature. For SKD-Wet3, the decreasing moduli above 523 K may involve the development of a new phase, as observed in X-ray diffraction above 573 K (see section 3.5).

The decrease in modulus with temperature above the transition was not as significant as observed for previous specimens (Figures 3.27 and 3.28), although only 50 K above the transition was observed, making characterization of the behavior above the transition limited. Poisson's ratio remained within a range of 0.235 to 0.241, with one outlier, throughout the entire range of temperature tested (Figure 3.29). Due to scatter within the Poisson's ratio, any effect on Poisson's ratio with temperature may not be apparent within the temperature range tested.

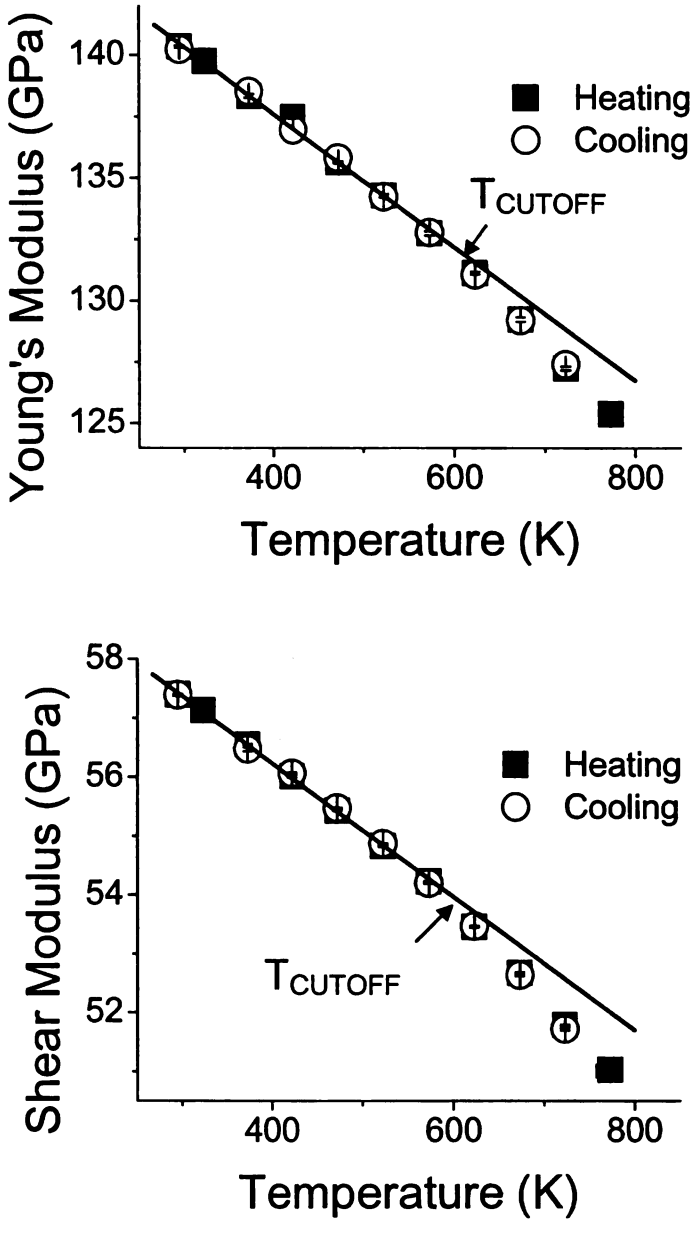

Figure 3.27 – The Young's modulus and shear modulus of SKD-Wet1-A changed linearly with temperature from room temperature until above T_{CUTOFF}, 600 K. Similarly, the Poisson's ratio, ν, remained relatively constant around 0.224 until about 600 K, above which it began to rise.

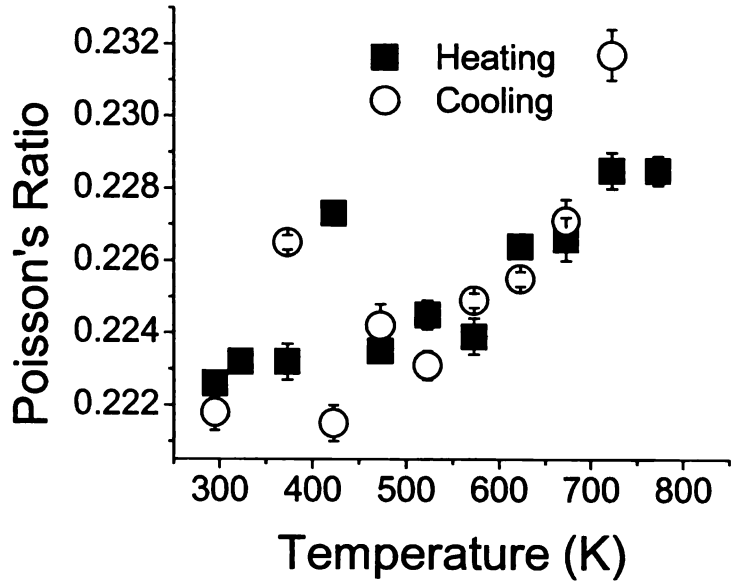

Figure 3.27 (continued)

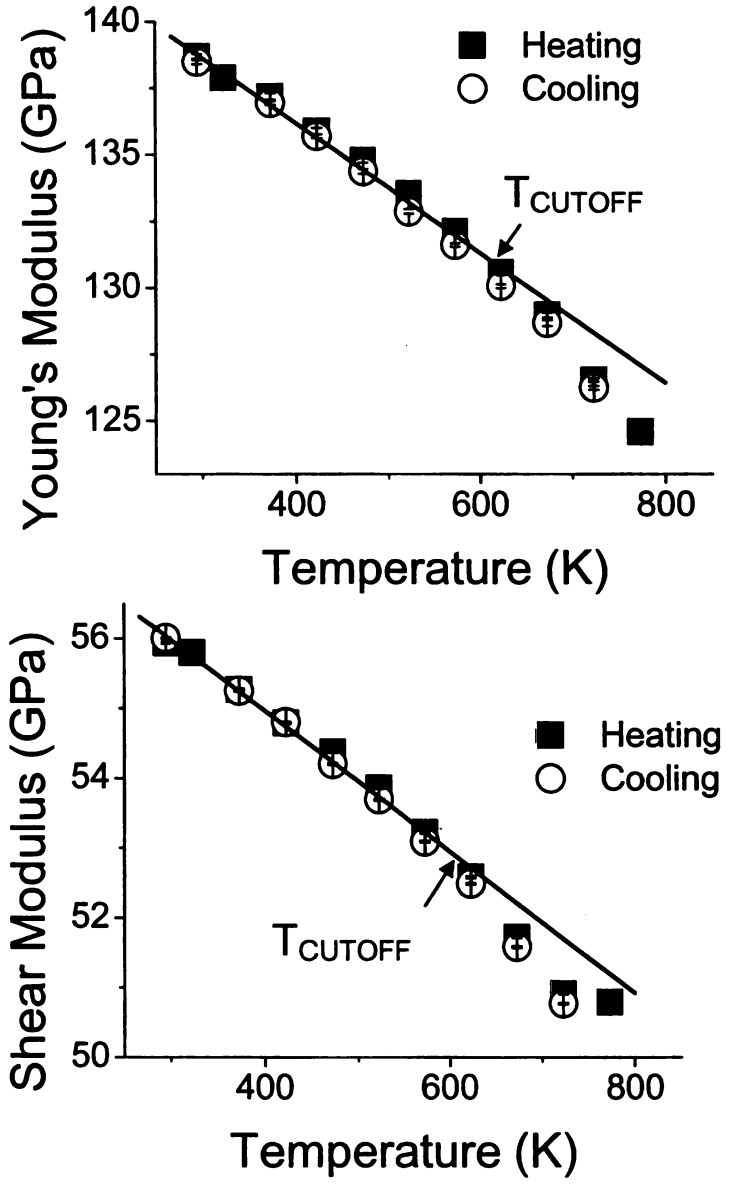

Figure 3.28 – The Young's modulus and shear modulus of SKD-Wet2-A, changed linearly with temperature from room temperature until above T_{CUTOFF}, 600 K. The highest temperature datapoint, 773 K, was an outlier, although the material returned to a similar measured value of all elastic moduli during cooling. Similarly, the Poisson's ratio, v, remained relatively constant around 0.240 until above 623 K, above which it began to rise with an outlier at 773 K

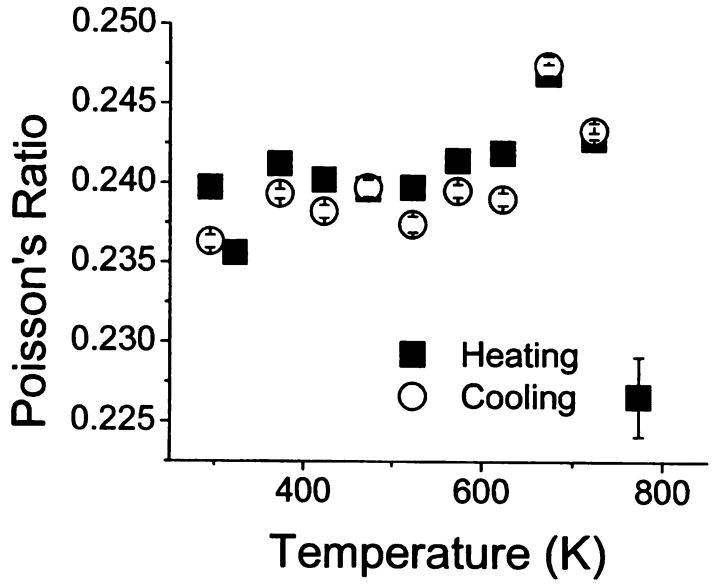

Figure 3.28 (continued)

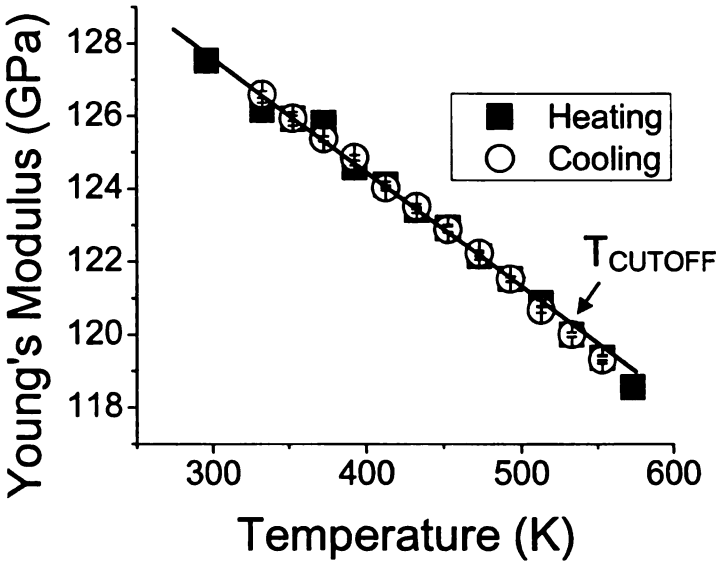

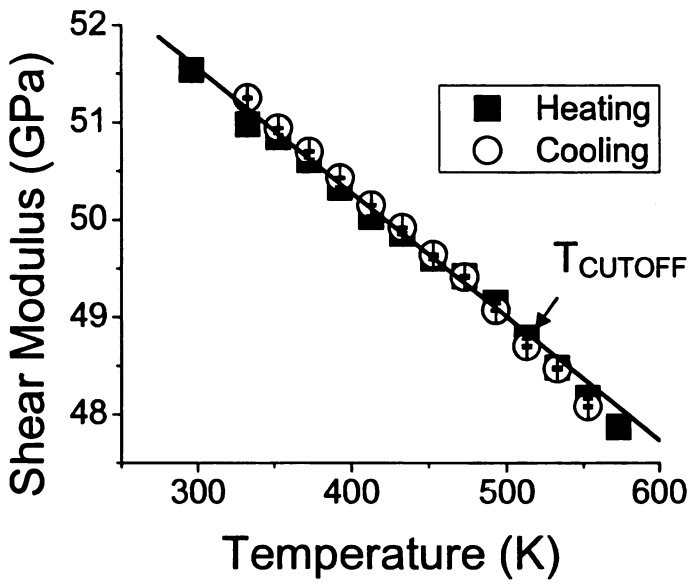

Figure 3.29 – The Young's and shear moduli of SKD-Wet3-K, composition $Ce_{0.9}Fe_{3.5}Co_{0.5}Sb_{12}$, remained linear with temperature until T_{CUTOFF}, above 523 K, when it began to increase the reduction of moduli with temperature. Some scatter exists within the Poisson's ratio, although it remains fairly constant near 0.238 throughout the range of 298 K to 573 K, with a possible increase at higher temperatures.

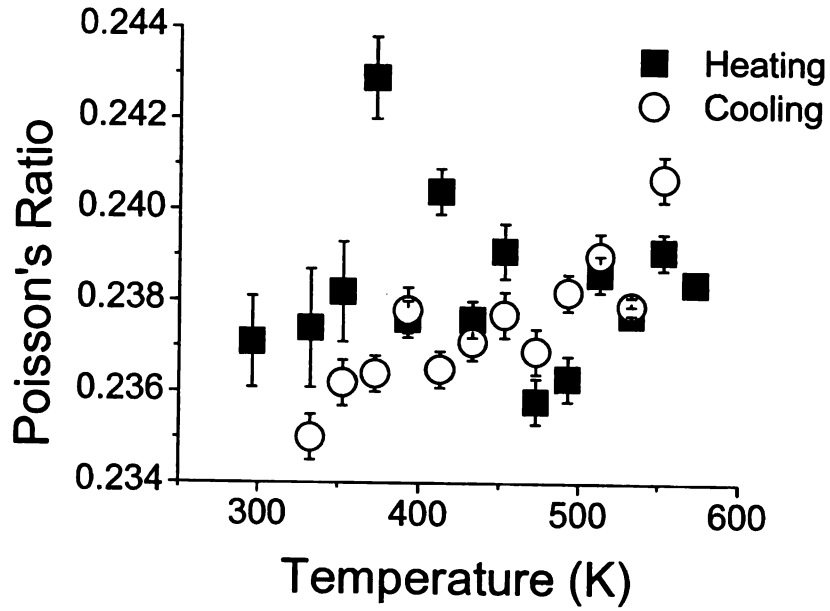

Figure 3.29 (continued)

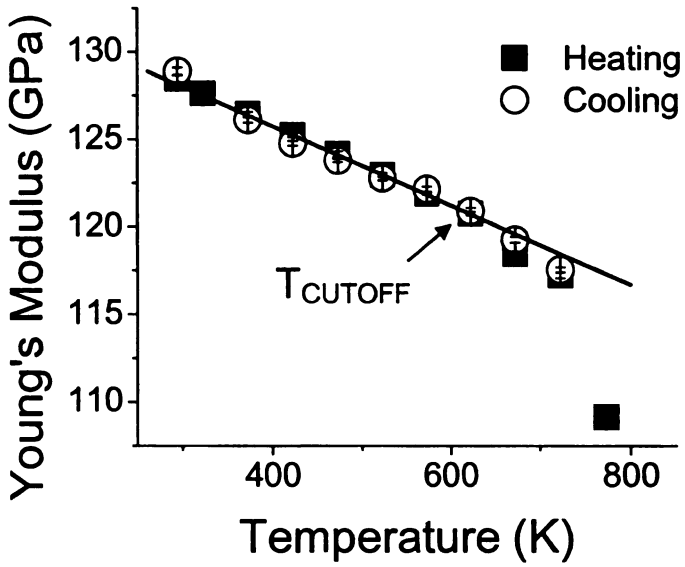

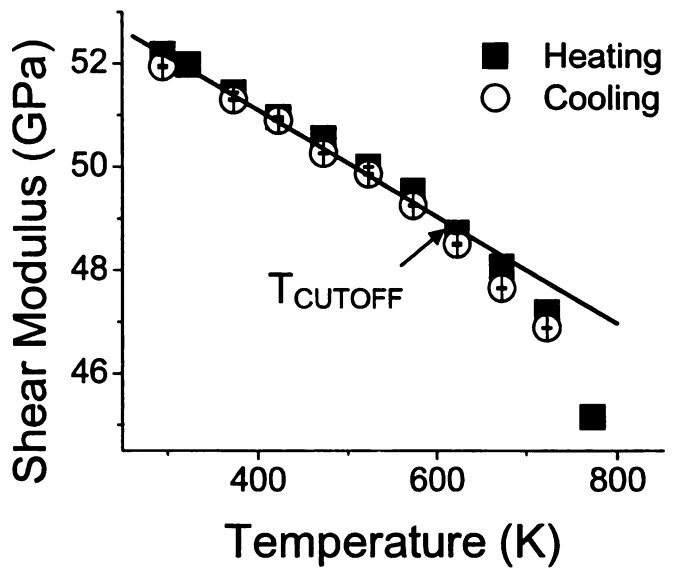

Figure 3.30 – SKD-Wet4 – The Young's modulus and shear modulus of SKD-Wet4-A changed linearly with temperature from room temperature until above T_{CUTOFF}, 623 K. The highest temperature datapoint, 773 K, was an outlier, although the material returned to a similar measured value of all elastic moduli during cooling. Similarly, the Poisson's ratio, c, remained relatively constant around 0.230 until above 573 K, above which it began to rise with an outlier at 773 K, and returning to near-constant upon cooling below 573 K.

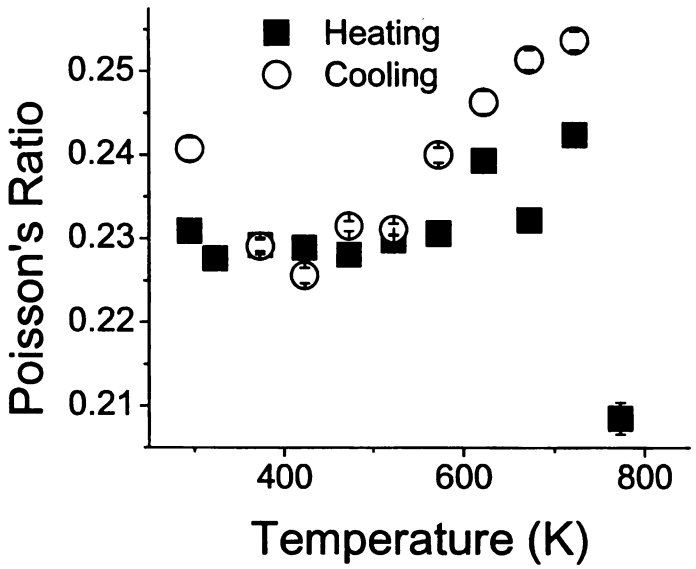

Figure 3.30 (continued)

Table 3.14 – The acoustic Debye temperature, as computed from the room temperature RUS measurements of the acoustic longitudinal velocity, V_L, and the shear velocity, V_S. The mean sound velocity, V_M, was calculated from these measurements and used to obtained the acoustic Debye temperature, θ_D.

	SKD-Wet1	SKD-Wet2	SKD-Wet3	SKD-Wet4
V_L (km/s)	4.622	4.602	4.460	4.551
V_S (km/s)	2.750	2.744	2.595	2.683
V_M (km/s)	3.044	3.037	2.879	2.973
θ_D (K)	318.1	317.4	303.8	310.6

On SKD-Wet3, a surface change was noticed after heating. The specimen was coated in a thin rust-colored material after cycling, although no change in specimen dimensions were detected. The entire thermal cycle was run in a chamber with flowing argon 96% - hydrogen 4%, making oxidizing of the surface unlikely. The surface material was not identified, and may be examined for future work.

The Young's modulus and shear modulus of SKD-Wet4 remained linear to approximately 623 K, and Poisson's ratio began to increase above 573 K (Figure 3.30). The moduli dropped dramatically from 723 K to 773 K, with Young's modulus decreasing 7% and shear modulus dropping 4.4%. The dramatic change in modulus was not permanent, as the cooling cycle moduli measurements resembled the heating cycle moduli measurements (Figure 3.30). Comparing against SKD-Wet2 (Figure 3.28), both specimens transitioned near 600 K, and both displayed a significant but non-permanent change in moduli at 773 K. Similar moduli behavior was expected for the two materials of the same composition, $Co_{0.95}Pd_{0.05}Te_{0.05}Sb_3$.

3.7 Vickers Hardness

The Vickers hardness was measured on the four wet milled skutterudite specimens, plus two dry milled p-type skutterudite specimens, with loads from 0.245 N to 4.9 N (Table 3.15, Figure 3.31). For four of the more difficult to measure sets of indentations, typically loads of 0.49N and less, some of the indentation impressions were measured by imaging the specimen on the SEM instead of the optical measurement on the hardness tester. Both optically measured and SEM micrograph measured hardness values were reported for a single load (Table 3.15) when both optical and SEM measurement methods were used.

The measurement of hardness of SKD-Wet3-A at 0.49 N illustrated the difficulty of accurate optical measurement of indentation impressions by the Shimadzu Microhardness Tester equipment when the size of the indentation was less than 15 μm. When comparing the hardness, H, measured by SEM and by optical at 0.49 N, the H values were nearly identical at 5.7 GPa, but the optical measurement produced significantly greater error than the SEM (Figure 3.31). Even though the Vickers hardness was measured from the same set of 25 indentation impressions, the optical measurement standard deviation,1.74 GPa, was nearly 9 times greater than the standard deviation of the SEM measurment, 0.20 GPa.

The hardness was not measured for loads greater than 4.9 N because the indentation impression was surrounded by cracking and spalling for the 2.94 N and 4.9 N loads. The spalling (Figure 3.32) was worse on larger loads, which made accurate

Table 3.15 – Vickers Hardness Measurements. Some Vickers indentation measurements were difficult to measure optically and were measured from SEM imaging, as indicated. The coefficient of variation, calculated as the standard deviation divided by hardness, is listed as COV.

Specimen	Type	Load (N)	Measurment Technique	Hardness (GPa)	Standard Dev	COV
SKD-Wet1-G	n-type	4.9	Optical	6.62	0.30	0.04
SKD-Wet1-H	n-type	2.94	Optical	6.42	0.17	0.03
SKD-Wet1-J	n-type	0.98	Optical	6.66	0.40	0.06
SKD-Wet1-J	n-type	0.49	Optical	6.95	0.50	0.07
SKD-Wet1-J	n-type	0.245	Optical	7.04	0.41	0.06
SKD-Wet2-K	n-type	0.98	Optical	5.36	0.28	0.05
SKD-Wet2-K	n-type	0.49	SEM	5.67	0.29	0.05
SKD-Wet2-K	n-type	0.245	SEM	5.92	0.29	0.05
SKD-Wet3-A	p-type	0.98	Optical	5.12	0.30	0.06
SKD-Wet3-A	p-type	0.98	SEM	4.83	0.20	0.04
SKD-Wet3-A	p-type	0.49	Optical	5.68	1.74	0.31
SKD-Wet3-A	p-type	0.49	SEM	5.67	0.29	0.05
SKD-Wet3-A	p-type	0.245	Optical	5.17	0.33	0.06
SKD-Wet4-G	n-type	0.98	Optical	4.35	0.33	0.08
SKD-Wet4-G	n-type	0.49	Optical	4.58	0.32	0.07
SKD-Wet4-G	n-type	0.245	Optical	4.86	0.44	0.09
SKD-17	p-type	2.94	Optical	5.63	0.24	0.04
SKD-18	p-type	2.94	Optical	5.60	0.21	0.04

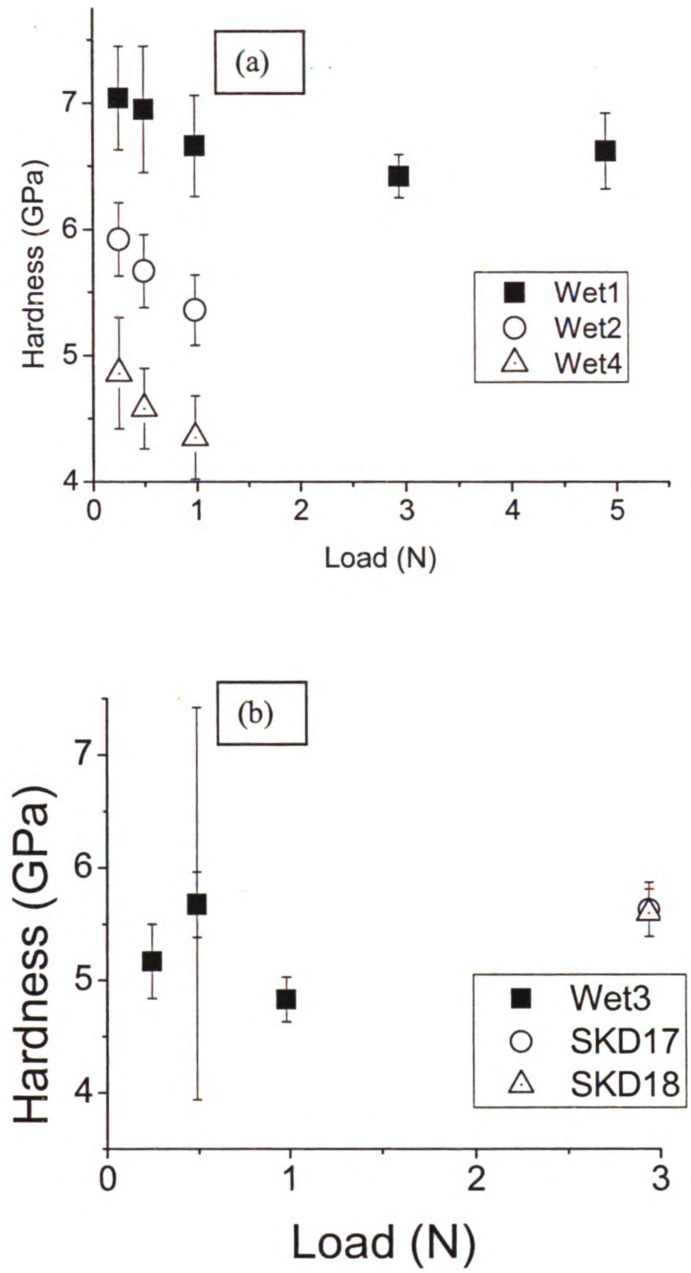

Figure 3.31 – Vickers hardness measurements for n-type (a) and p-type (b). The n-type hardness exhibited consistent hardness values, with a possible rise in hardness at lower loads. Increased hardness corresponds to decreasing porosity between billets. The p-type specimens were less consistent, but all were in a range of 4.8 to 5.7 GPa, regardless of load. The plot shows the difference in error between two measuring techniques at the same load, with measurement by SEM micrographs producing a smaller error on the same indentations than optical measurement.

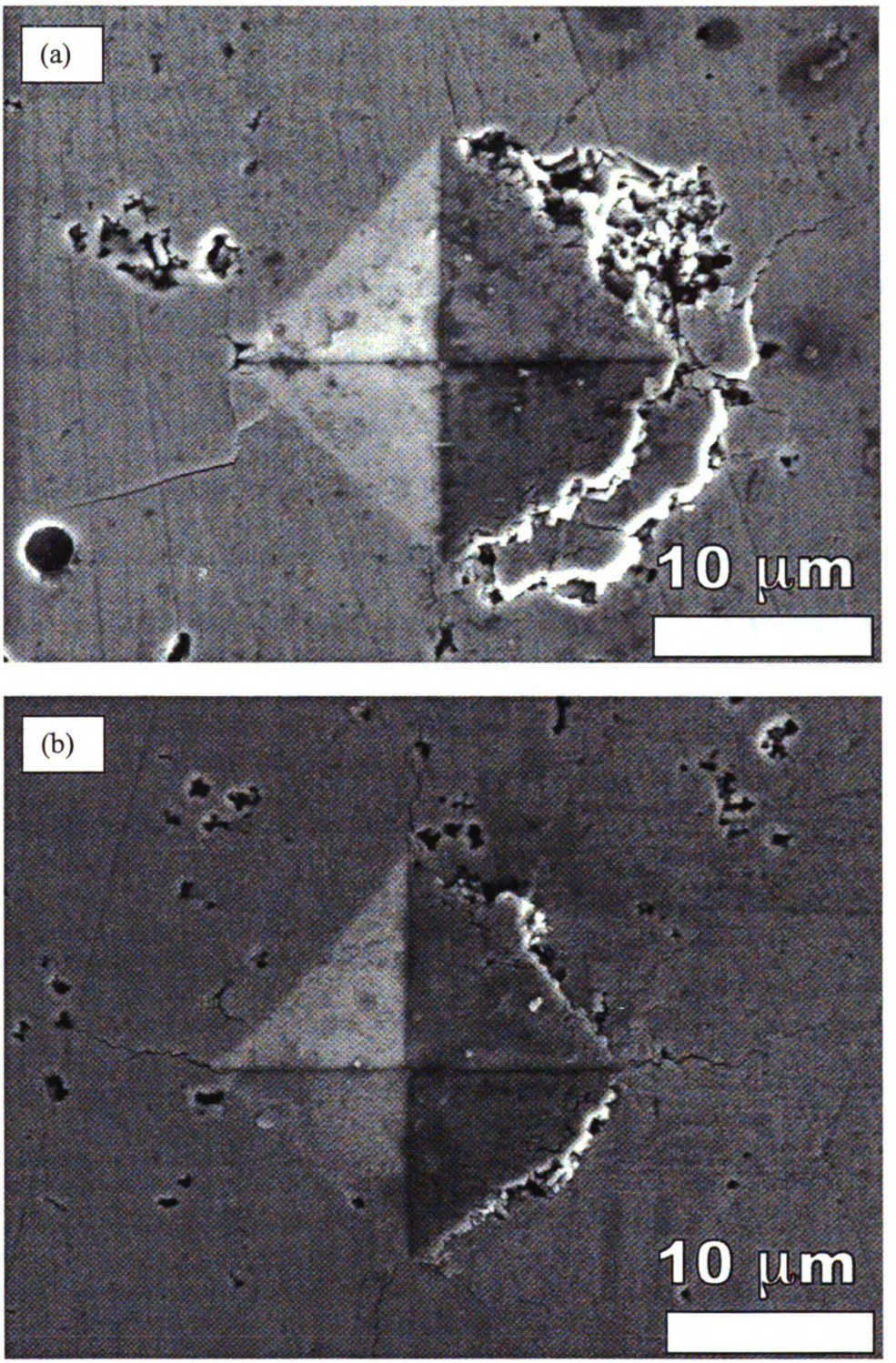

Figure 3.32 – Vickers indentation impressions, showing an impression with significant spalling (a), making measurement of the impression size impossible, and a typical impression (b). Both SEM micrographs were taken from specimen SKD-Wet3A, composition $Ce_{0.9}Fe_{3.5}Co_{0.5}Sb_{12}$, with a 0.245 N load.

measurement of the dimensions of the indentation impression impossible for loads above 4.9 N.

Vickers impressions for the 0.49 N and 0.245 N loads were between 8 μm and 20 μm (Figure 3.32), which was about 5 to 10 times the average grain size for the material. The size of these indentation impressions crossed multiple grains and should not be considered a potential single grain measurement size.

A possible indentation size effect [Bull 1989] was observed for n-type materials tested between 0.245 N and 0.98 N loads, before reaching a plateau of hardness (Figure 3.31a). Bull et al. have observed an increase in hardness for SiC, MgO and Al_2O_3 when the indentation impression decreased below 10 μm to 20 μm [Bull 1989], sizes consistent with the observed increase in hardness of n-type skutterudite materials in this study. The error bars of all the loads overlap (Figure 3.31a), indicating that there were no statistically significant differences among the H values for the load range from 0.245 N to 0.98 N, although the behavior of decreasing hardness with increasing load was consistently observed across all three specimens.

Differences in hardness among specimens of the same type may be attributed in part or whole to differences in porosity. The hardness consistently was higher for more dense specimens, which is consistent with the hardness-porosity behavior of many ceramic materials [Rice 1998]. Examining several ceramic materials, including Al_2O_3, B_4C, hydroxyapatite and ZrO_2, Rice noted the porosity relationship between hardness and elastic properties often was very similar [Rice 1998], and a first estimate of the porosity dependence of hardness may be taken from the porosity dependence of elastic moduli

(Equation 3.1, see section 3.3.2). Further study may determine the porosity dependence to hardness for the materials in this study.

3.8 Surface material changes and mass change

Following the high temperature RUS measurement of SKD-Wet3-G (see section 3.6) heating to 773 K and returning to room temperature, a visible change in the surface material was observed. The surface material was observed to be a dull rusty brown color, with an underlying shiny base. Visual inspection estimated the thickness at microns to tens of microns thick.

As a result of observing a new phase upon the heating of SKD-Wet3 to 773 K, all heated specimens were compared by mass for changes. If a new compound was formed with the addition of mass from air or by a reaction releasing material as a gas, the mass of the bulk material was expected to change. For example, if iron oxide formed in the first 20 micrometers of the surface, the mass would increase by 0.0007 g. Several reactions are possible, but the mass change may be detected if the sum of all mass changes is sufficiently large.

The mass change for each specimen (Table 3.?) indicated a possible loss of mass for all specimens but SKD-Wet1-A run in the high temperature RUS chamber. The change in mass for SKD-Wet3-G was the greatest of all specimens, with a loss of 0.0019 g. The loss of mass may be due to the loss of powder from the surface of the specimen. The surface layer was powdery and would partially come off with handling.

The change in mass of SKD-Wet3-G was inconclusive in identifying the changes to the specimen induced by heating to 773 K. Possible explanations include an oxide of iron or antimony, or a transferred rust from the Inconel thermocouple shield near the specimen in the furnace.

Table 3.16 – Mass of specimens after thermal cycling in high temperature RUS chamber. The SKD-Wet3-G specimen was removed from the chamber with a rusty colored surface of unknown origin. Mass change measurements were inconclusive for assisting to identify the surface material.

Specimen	Mass before run	Mass after run	Difference	% difference	maximum temp of run
SKD-Wet1-A	2.699	2.7004	-0.0014	-0.05%	773
SKD-Wet2-A	2.513	2.5126	0.0004	0.02%	773
SKD-Wet3-G	2.4814	2.4795	0.0019	0.08%	773
SKD-Wet3-K	2.4936	2.4931	0.0005	0.02%	573
SKD-Wet4-A	2.4903	2.4890	0.0013	0.05%	573

3.3.3 Room Temperature Elastic moduli by nanoindentation

Young's moduli values were measured by nanoindentation on a specimen each of SKD-Wet1 and SKD-Wet2 (Table 3.7). To calculate a Young's modulus from the unloading behavior using the Oliver-Pharr method, a Poisson's ratio of 0.23 was assumed. The choice of the assumed Poisson's ratio was based upon an average value of Poisson's ratio determined by RUS (Table 3.4) [Schmidt 2010, Oliver 1992]. A minimum of 20 indentations were attempted per surface, with 16 in a 4 x 4 grid separated by 50 μm and 4 or more added manually outside the grid. Invalid indentations may be caused by external vibrations in the building, or the indenter contacting the specimen surface on a pore or crack, and these invalid indentations were disregarded. The indentations of SKD-Wet1 and SKD-Wet2 on 3 mutually orthogonal surfaces did not exhibit significant anisotropy [Schmidt 2010]. The moduli of SKD-Wet1 and SKD-Wet2 averaged about 8% higher than those determined by RUS [Schmidt 2010].

Young's modulus by nanoindentation was higher than the value determined by RUS. Radovic et al. demonstrated that nanoindentation to determine Young's moduli for alumina, among other materials, was higher than Young's modulus determined by RUS, likely due in part to porosity differences, but lower than theoretically dense Young's modulus [Radovic 2004]. Comparing the Young's modulus of SKD-Wet2 by nanoindentation (Table 3.7) to the theoretically dense Young's modulus of the same material (Table 3.6), the theoretically dense Young's modulus was about 6% higher than the average by nanoindentation. Radovic et al. stated the value of Young's modulus by nanoindentation in alumina was near the theoretically dense value when the indenter was

not influenced by nearby porosity and lower than theoretically dense when the indenter was near porosity, with the general result that Young's modulus determined by nanoindentation was between a minimum of the bulk Young's modulus determined by RUS and the theoretically dense Young's modulus [Radovic 2004]. The Young's modulus value determined by nanoindentation for the skutterudite material in this study was bracketed by the theoretically dense value at the high end and the bulk value by RUS at the low end, as predicted by Radovic et al. for alumina [Radovic 2004].

The MTS nanoindenter XP at Michigan State University used in this study has been used in a previous study of lead telluride-based thermoelectric materials [Ren 2009]. In the previous study by Ren et al., nanoindentations of aluminum alloy Al6061 gave H values of 85.5 ± 1.8 GPa [Ren 2009], as compared to H values of 82.0 ± 2.2 GPa measured on the same aluminum alloy, Al6061, in this study [Schmidt 2010]. The consistent values provide greater confidence in consistent results of the modulus measurement in this study.

4 Summary and Conclusions

The work presented in this thesis on the n-type skutterudite, $Co_{0.95}Pd_{0.05}Te_{0.05}Sb_3$, both with and without 0.1 atomic % cerium dopant, and the p-type skutterudite, $Ce_{0.9}Fe_{3.5}Co_{0.5}Sb_{12}$, may be broadly categorized in three areas, (i) processing and microstructure, (ii) room temperature mechanical properties, and (iii) mechanical properties as a function of temperature.

Powder processing was accomplished in an argon atmosphere glove box with a mechanical mortar and pestle (Retsch RM200, Retsch GmbH, Haan, Germany) and ball mill (Retsch PM100). Microstructure was evaluated by SEM micrography (JEOL 6400, JEOL Ltd., Japan). Elastic moduli were determined by resonant ultrasound spectroscopy (Quasar RUSpec, Quasar International, Albuquerque, NM) and nanoindentation (Nanoindenter XP with CSM/LFM, MTS, Oak Ridge, TN). Hardness was measured by microindentation (Buehler Semimacro Indenter, Lake Bluff, IL, and Shimadzu HMV-2000, Kyoto, Japan) and nanoindentation. Thermal expansion was measured by thermomechanical analyzer (Q400, TA Instruments, New Castle, DE). Lattice parameter was measured by X-ray diffraction (PANalytical PW3040-PRO, Serial #DY1331, PANalytical B. V., Almeno, Netherlands).

Processing and microstructure began by processing an ingot of skutterudite material into a powder. The powder processing first began with crushing, grinding and regrinding the ingot until all powder passed through a 75 μm sieve. The powder was then processed to reduce the particle size to a minimum via ball milling (Appendix A).

Milling evolved from a two step process with significant scraping of the mill jar after each milling to a one step process with reduced caking and scraping of the mill jar, and less powder lost during processing. Ball milling was initially run by a process previously developed for LAST [Hall 2008], with a 3 hour dry milling at 150 RPM, followed by a 6 hour wet milling at 120 RPM with a hexane milling medium. Later batches that employed wet milling with ethanol resulted in reduced caking and easier processing of the powder (Appendix A). Beginning with batch 2 of the third ingot processed, JSpSKD-15, the 3 hour dry milling was eliminated and only wet milling was used. To achieve similar or better results without dry milling, milling time was increased to 9 hours. Increasing milling time also increased evaporation of the ethanol, requiring an increase from 25 mL to 42 mL. Eliminating dry milling reduced the manual handling of the powder between steps, and ethanol use decreased the caking of powder and increased the powder recovered after each milling.

Microstructural evaluation of the milled powders was done by evaluating a sample from each batch of the powders before hot pressing until safety concerns stopped powder particle size analysis. Powder samples of the first two hot pressed billets, SKD-Wet1 and SKD-Wet2, plus one batch from SKD-Wet3, were analyzed for powder particle size analysis (Tables 3.1 and 3.2, Figures 3.1, 3.2, 3.4), with the results confirmed qualitatively by SEM micrograph inspection (Figures 3.5 through 3.7). Powders of specimens JSpSKD-15 and JSnSKD-14 were pyrophoric when exposed to air, spontaneously combusting while handling. Due to safety concerns, the powder particle size analysis was suspended.

All four hot pressed billets were fractured and thermal etched to determine grain size (Table 3.3). The average matrix grain size was consistently less than 2 μm in diameter, consistent with the powder particle size of the wet milled powder (Tables 3.1 and 3.2). Thermally etching a specimen required a polished surface, and the thermal etch was not always successful. The only reliable method of grain size analysis was by SEM micrography analysis of a fractured surface.

Room temperature elastic moduli were measured by resonant ultrasound spectroscopy and nanoindentation. Specimens for RUS were nominally 10 x 7 x 5 mm. The moduli for p-type were 126.8 to 131.2 GPa Young's modulus, 51.04 to 53.35 GPa shear modulus, and 0.230 to 0.242 Poisson's ratio (Table 3.4). For n-type, Young's modulus was 129.0 to 140.6 GPa, shear modulus was 52.28 to 57.34 GPa, and Poisson's ratio was 0.226 to 0.234. The moduli measured by RUS were consistent within each billet to a maximum standard deviation of 1.2 GPa for Young's modulus, 0.54 GPa for shear modulus and 0.011 for Poisson's ratio. The variation in moduli may be accounted for by variation in porosity. In the case of the n-type skutterudite material, the addition of 0.1 atomic % cerium in SKD-Wet1 may account for some variation in moduli between SKD-Wet1 and the other two n-type materials, SKD-Wet2 and SKD-Wet4 (Figure 3.20 and 3.21). The elastic modulus data were fit to the following equation

$$A = A_0 \exp(-bP) \qquad \text{(Equation 3.1)}$$

where A was the Young's or shear modulus at the indicated porosity, A_0 was the theoretically dense Young's or shear modulus, P was the volume fraction porosity, and b was a material-dependent fitting parameter (Table 3.6).

Specimens of SKD-Wet1 and SKD-Wet2 were polished on 3 mutually orthogonal faces, one face normal to the hot press direction, and nanoindented on each face (Table 3.7). The results of the nanoindentation indicated no significant anisotropy for either specimen, with the Young's modulus of SKD-Wet1 measured between 149.8 GPa and 154.7 GPa, and the Young's modulus of SKD-Wet2 between 139.4 GPa and 151.0 GPa [Schmidt 2010]. The values of the Young's moduli measured (Table 3.7) was between the theoretically dense and the measured bulk values, as anticipated.

Vickers hardness for each specimen was determined for multiple loads between 0.245 N and 4.9 N (Table 3.15). Hardness values did not change in a statistically significant amount as a function of load, as all the error bars overlapped, but a possible indentation size effect for loads less than 1 N was observed on the n-type material (Figure 3.31). Hardness was between 4.35 GPa and 7.04 GPa for all specimens, with hardness increasing with the density of the specimen (Table 3.5, 3.15).

Thermal expansion by bulk was measured for each of four wet milled billets (Table 3.8). The n-type, cerium doped specimen had a thermal expansion coefficient of $11.6 \times 10^{-6}\ K^{-1}$, the CTE for the non-cerium doped was 9.8 to $10.2 \times 10^{-6}\ K^{-1}$, and the p-type thermal expansion coefficient was $13.0 \times 10^{-6}\ K^{-1}$. A CTE of $13.0 \times 10^{-6}\ K^{-1}$ was measured via X-ray powder diffraction for the p-type specimen.

The lattice parameter of the p-type material was measured by X-ray diffraction as 0.91241 nm at 303 K, and increased linearly through 633 K (Figure 3.30, Table 3.14). A new set of peaks appeared on the X-ray diffraction pattern when the powder was heated to 603 K. The extra XRD peaks remained after cooling, indicating a new phase

developed around 603 K and remained stable as the sample was cooled to room temperature (Figure 3.29).

The elastic moduli decreased linearly with increasing temperature over the interval from room temperature to a cutoff temperature between 523 K and 623 K. At temperatures greater than the cutoff temperature, a viscoelastic region began and the elastic moduli decreased nonlinearly (Figure 3.16 through 3.19). The acoustic Debye temperature, θ_D, (Table 3.13) was between 303 K and 318 K for all specimens. The typical high temperature limit for cryogenic behavior of $0.3\theta_D$ to $0.5\theta_D$ [Ren 2009] was well below any of the temperatures tested in this study.

The skutterudite thermoelectric materials in this study are sturdy enough to be assembled into a reasonable thermoelectric generator for a temperature range from room temperature to 603 K. At 603 K, a new phase was observed to develop in the p-type material, and, at a temperature between 573 K and 773 K, an unidentified rust-colored surface layer developed on the p-type. The rust-colored surface layer and the new phase observed in X-ray diffraction may be the same phase, but the phase has not been determined for either material. For these reasons, the p-type material should be studied above 603 K to determine if the material remains suitable for use. In addition, all specimens reached a viscoelastic region above 623 K, which may reduce the mechanical integrity of a thermoelectric device if operated above 623 K. The elastic moduli may be tuned as desired if the porosity of the hot pressed material can be controlled. The CTE of the p-type skutterudite material was about 30% higher than the n-type, non-cerium doped material, and the increased thermal expansion needs to be managed in a device. Based on hardness and an accidental drop, the skutterudite material appears robust enough to

withstand field use in a generator package. In general, the skutterudite materials in this study may be used between room temperature and 603 K without material changes. Higher temperature use may require further study.

5 Future Work

The porosity-elastic moduli relationship has been determined for a narrow range between 0.023 and 0.064 volume fraction porosity for the p-type skutterudite material and the non-cerium doped n-type material (Figures 3.20 and 3.21, Table 3.6). With the narrow range of experimental porosity values, the elastic modulus-porosity relationship is not well determined. Also, the porosity-elastic modulus relationship for cerium-doped n-type skutterudite material has not been evaluated. Additional specimens of all the skutterudite materials in this study with varying volume fraction porosity could be used to evaluate and extend the porosity-elastic moduli relationships.

If the skutterudite materials are used at temperatures above 623 K, the viscoelastic region of the temperature-elastic moduli region (Figure 3.27 through 3.30) must be examined further, especially on the p-type skutterudite. For all materials, the mechanism for the viscoelastic behavior should be determined to ensure the material is stable above 623 K. For the p-type skutterudite material, a new phase developed in XRD at 603 K. The new phase in p-type skutterudite material should be identified and the material with both the unidentified phase and the p-type skutterudite phase checked for mechanical, electrical and thermal properties.

Also an unidentified rust-colored surface layer developed on the p-type skutterudite material when heated to 773 K in a 96% argon 4% hydrogen atmosphere. The nature and physical properties of the rust-colored surface layer should be determined.

For all specimens included in this study, the thermal expansion curves evidenced an irreversible increase in specimen volume that occurred at temperatures above 573 K.

Although the physical mechanism that generates the irreversible increase in the specimen volume has not yet been identified, understanding the behavior may be necessary to use the skutterudite materials above about 600 K.

Additional measurements of the Vickers hardness would be enlightening to see if there is a indentation size effect in the n-type material for loads of less than 1 N. Current results were inconclusive due to the amount of error in the hardness measurement, but suggested a possible indentation size effect on the n-type material.

During the oral defense of this thesis, the following additional areas of future work were discussed. First differential scanning calorimeter (DSC) measurements of the p-type material was discussed as a method to investigate the new phase observed in X-ray diffraction measurements. DSC measures the change in heat energy as a function of heat for a specimen by carefully measuring the heat lost or gained as the specimen temperature changes.

APPENDIX A

Appendix A1 – Dry Milling Conditions

Ingot	Batch Number	Batch Size	Date	Media Diameter	Media Amount	Media Type
N-SKD-Min2	B1	30.00g	8 March 2009	10 mm	390.77g	WC
	B2	25.00g	24 March 2009	20 mm 6 mm	226.20g 170.03g	SS
	B3	23.00g	26 March 2009	20 mm	227.21g	SS
	B4	23.05g	1 April 2009	10 mm	233.31g	SS
ETN-SKD-10	B1	24.33g	2 June 2009	10 mm	229.90g	SS
	B2	24.00g	4 June 2009	10 mm	229.99g	SS
	B3	23.88g	5 June 2009	10 mm	230.13g	SS
	B4	23.88g	8 June 2009	10 mm	230.08g	SS
JSp-SKD-15	B1	23.81g	16 June 2009	20 mm	226.49g	SS
	B2	N/A	N/A	N/A	N/A	N/A
	B3	N/A	N/A	N/A	N/A	N/A
	B4	N/A	N/A	N/A	N/A	N/A
JSn-SKD-14	B1	N/A	N/A	N/A	N/A	N/A
	B2	N/A	N/A	N/A	N/A	N/A
	B3	N/A	N/A	N/A	N/A	N/A
	B4	N/A	N/A	N/A	N/A	N/A

Appendix A2 – Wet Milling Conditions

Ingot	Batch Number	Batch Size	Date	Media Diameter	Media Amount	Milling Fluid	Media Type
N-SKD-Min2	B1	26.60g	8 March 2009	20 mm 6 mm	412.82g 100.20g	25 mL Hexane	WC
	B2	20.55g	25 March 2009	20 mm 6 mm	226.22g 170.32g	25 mL Hexane	SS
	B3	21.00g	26 March 2009	20 mm 6 mm	226.30g 173.23g	25 mL Hexane	SS
	B4	18.70g	3 April 2009	20 mm 3 mm	226.14g 170.10g	25 mL Hexane	SS
ETN-SKD-10	B1	22.01g	4 June 2009	20 mm 6 mm	226.05g 170.10g	25 mL Ethanol	SS
	B2	22.00g	4 June 2009	20 mm 6 mm	226.13g 170.14g	25 mL Ethanol	SS
	B3	21.50g	5 June 2009	20 mm 6 mm	226.12g 170.23g	25 mL Ethanol	SS
	B4	22.00g	8 June 2009	20 mm 6 mm	226.02g 170.26g	25 mL Ethanol	SS
JSp-SKD-15	B1	18.00g	16 June 2009	20 mm 6 mm	230.23g 170.05g	25 mL Ethanol	SS
	B2	23.80g	17 June 2009	20 mm 6 mm	226.42g 170.39g	25 mL Ethanol	SS
	B3	23.80g	18 June 2009	20 mm 6 mm	226.41g 170.47g	25 mL Ethanol	SS
	B4	23.80g	25 June 2009	20 mm 6 mm	226.44g 170.08g	37 mL Ethanol	SS
JSn-SKD-14	B1	23.50g	30 July 2009	20 mm 6 mm	226.08g 170.02g	25 mL Ethanol	SS
	B2	23.50g	31 July 2009	20 mm 6 mm	226.15g 170.32g	25 mL Ethanol	SS
	B3	23.50g	2 August 2009	20 mm 6 mm	226.21g 170.44g	37 mL Ethanol	SS
	B4	23.50g	3 August 2009	20 mm 6 mm	226.23g 170.43g	42 mL Ethanol	SS

APPENDIX B

Appendix B1 – High temperature RUS measurement results for SKD-Wet1-A in chronological order from the top, where E is Young's modulus, G is shear modulus, v is Poisson's ratio, and RMS error is the error of the model fit to the frequency peaks.

Temp (K)	E (GPa)	Eerror (GPa)	G (GPa)	Gerror (GPa)	v	verror	RMS error	Number of Frequencies Matched
295	140.35	0.05	57.40	0.006	0.223	0.0003	0.06%	23
323	139.76	0.06	57.13	0.011	0.223	0.0003	0.04%	20
373	138.34	0.08	56.55	0.011	0.223	0.0005	0.05%	27
423	137.48	0.07	56.01	0.017	0.227	0.0003	0.06%	24
473	135.64	0.05	55.43	0.006	0.223	0.0003	0.03%	19
523	134.28	0.07	54.83	0.011	0.224	0.0004	0.04%	22
573	132.75	0.08	54.23	0.011	0.224	0.0005	0.04%	19
623	131.12	0.06	53.46	0.011	0.226	0.0003	0.04%	21
673	129.24	0.09	52.68	0.011	0.227	0.0006	0.04%	17
723	127.24	0.08	51.79	0.010	0.228	0.0005	0.04%	17
773	125.38	0.09	51.03	0.020	0.229	0.0004	0.07%	16
723	127.40	0.12	51.72	0.021	0.232	0.0007	0.06%	15
673	129.19	0.10	52.64	0.016	0.227	0.0006	0.04%	14
623	131.06	0.05	53.47	0.011	0.226	0.0002	0.05%	26
573	132.78	0.05	54.20	0.011	0.225	0.0002	0.05%	29
523	134.23	0.07	54.87	0.011	0.223	0.0004	0.04%	23
473	135.81	0.09	55.47	0.011	0.224	0.0006	0.05%	22
423	136.96	0.10	56.06	0.017	0.222	0.0005	0.06%	25
373	138.52	0.11	56.47	0.034	0.226	0.0002	0.05%	31
295	140.24	0.10	57.39	0.017	0.222	0.0005	0.06%	28

Appendix B2 – High temperature RUS measurement results for SKD-Wet2-A in chronological order from the top, where E is Young's modulus, G is shear modulus, ν is Poisson's ratio, and RMS error is the error of the model fit to the frequency peaks.

Temp (K)	E (GPa)	Eerror (GPa)	G (GPa)	Gerror (GPa)	ν	verror	RMS error	Number of Frequencies Matched
295	138.70	0.09	55.94	0.011	0.240	0.001	0.05%	21
323	137.89	0.12	55.80	0.017	0.236	0.001	0.07%	23
373	137.20	0.12	55.27	0.017	0.241	0.001	0.07%	27
423	135.90	0.12	54.79	0.016	0.240	0.001	0.08%	27
473	134.79	0.09	54.37	0.011	0.240	0.001	0.06%	26
523	133.54	0.07	53.86	0.016	0.240	0.000	0.06%	26
573	132.13	0.10	53.22	0.016	0.241	0.001	0.06%	25
623	130.59	0.11	52.58	0.016	0.242	0.001	0.07%	23
673	128.98	0.09	51.72	0.010	0.247	0.001	0.06%	24
723	126.54	0.06	50.91	0.010	0.243	0.000	0.05%	18
773	124.59	0.39	50.79	0.056	0.227	0.002	0.18%	13
723	126.25	0.07	50.77	0.010	0.243	0.000	0.04%	20
673	128.68	0.11	51.58	0.015	0.247	0.001	0.07%	24
623	130.07	0.07	52.49	0.010	0.239	0.000	0.04%	19
573	131.61	0.07	53.09	0.011	0.239	0.000	0.04%	20
523	132.87	0.08	53.69	0.011	0.237	0.001	0.06%	22
473	134.38	0.09	54.20	0.011	0.240	0.001	0.06%	24
423	135.70	0.08	54.80	0.011	0.238	0.000	0.05%	21
373	136.95	0.06	55.25	0.011	0.239	0.000	0.05%	22
295	138.49	0.08	56.01	0.011	0.236	0.000	0.05%	20

Appendix B3 – High temperature RUS measurement results for SKD-Wet3-K, where E is Young's modulus, G is shear modulus, ν is Poisson's ratio, and RMS error is the error of the model fit to the frequency peaks.

Temp (K)	E (GPa)	Eerror (GPa)	G (GPa)	Gerror (GPa)	ν	verror	RMS error	Number of Frequencies Matched
293	126.03	0.19	50.78	0.025	0.241	0.0012	0.08%	14
333	126.03	0.19	50.78	0.025	0.241	0.0012	0.08%	14
333	126.17	0.20	50.98	0.025	0.241	0.0013	0.08%	14
353	125.92	0.19	50.85	0.031	0.237	0.0011	0.07%	14
373	125.81	0.14	50.61	0.020	0.238	0.0009	0.06%	14
393	124.58	0.07	50.33	0.010	0.243	0.0004	0.04%	18
413	124.11	0.08	50.03	0.015	0.238	0.0005	0.05%	14
433	123.42	0.08	49.86	0.015	0.240	0.0004	0.05%	15
453	122.92	0.10	49.60	0.015	0.238	0.0006	0.07%	21
473	122.15	0.09	49.42	0.015	0.239	0.0005	0.05%	16
493	121.53	0.08	49.15	0.015	0.236	0.0005	0.06%	18
513	120.86	0.08	48.79	0.015	0.236	0.0004	0.05%	15
533	120.00	0.06	48.48	0.015	0.239	0.0002	0.05%	17
553	119.37	0.07	48.17	0.014	0.238	0.0004	0.05%	16
573	118.56	0.05	47.87	0.014	0.239	0.0002	0.05%	17
553	119.31	0.09	48.08	0.014	0.238	0.0005	0.05%	14
533	120.01	0.06	48.47	0.015	0.241	0.0002	0.06%	19
513	120.68	0.08	48.70	0.015	0.238	0.0005	0.05%	17
493	121.52	0.06	49.07	0.010	0.238	0.0004	0.04%	17
473	122.23	0.08	49.41	0.015	0.237	0.0005	0.05%	15
453	122.88	0.08	49.64	0.015	0.238	0.0005	0.05%	22
433	123.51	0.07	49.92	0.010	0.237	0.0004	0.04%	17
413	124.02	0.07	50.15	0.010	0.236	0.0004	0.05%	17
393	124.85	0.08	50.43	0.010	0.238	0.0005	0.05%	22
373	125.37	0.07	50.70	0.010	0.236	0.0004	0.05%	21
353	125.94	0.07	50.94	0.010	0.236	0.0005	0.05%	21
333	126.59	0.09	51.25	0.015	0.235	0.0005	0.06%	21

Appendix B

Appendix B4 – High temperature RUS measurement results for SKD-Wet4-A in chronological order from the top, where E is Young's modulus, G is shear modulus, ν is Poisson's ratio, and RMS error is the error of the model fit to the frequency peaks.

Temp (K)	E (GPa)	Eerror (GPa)	G (GPa)	Gerror (GPa)	ν	verror	RMS error	Number of Frequencies Matched
295	128.46	0.19	52.18	0.026	0.231	0.0012	0.11%	21
323	127.62	0.15	51.98	0.021	0.228	0.0010	0.08%	17
373	126.46	0.11	51.44	0.015	0.229	0.0007	0.08%	19
423	125.24	0.11	50.96	0.015	0.229	0.0007	0.08%	19
473	124.16	0.16	50.55	0.020	0.228	0.0011	0.09%	18
523	122.98	0.11	50.00	0.015	0.230	0.0007	0.06%	14
573	121.90	0.06	49.53	0.010	0.231	0.0003	0.04%	15
623	120.75	0.10	48.72	0.015	0.239	0.0007	0.06%	15
673	118.44	0.14	48.06	0.019	0.232	0.0009	0.09%	14
723	117.24	0.17	47.18	0.024	0.242	0.0012	0.09%	16
773	109.13	0.27	45.15	0.041	0.209	0.0019	0.11%	12
723	117.54	0.15	46.88	0.019	0.254	0.0011	0.09%	15
673	119.26	0.16	47.65	0.019	0.251	0.0012	0.09%	19
623	120.89	0.20	48.50	0.024	0.246	0.0014	0.10%	17
573	122.14	0.14	49.25	0.020	0.240	0.0009	0.08%	16
523	122.76	0.12	49.86	0.020	0.231	0.0007	0.08%	17
473	123.79	0.10	50.26	0.015	0.231	0.0006	0.08%	20
423	124.76	0.14	50.90	0.020	0.226	0.0009	0.07%	14
373	126.10	0.15	51.30	0.021	0.229	0.0010	0.09%	15
295	128.89	0.21	51.94	0.026	0.241	0.0014	0.09%	15

REFERENCES

[Anderson 1963] O. Anderson. A simplified method for calculating the Debye temperature from elastic constants. J. Phys. Chem. Solids 24 (1963) 909-917.

[Bull 1989] S.J. Bull, T.F. Page, E.H. Yoffe. An explanation of the indentation size effect in ceramics. Phil. Mag. Lett. 59 (1989) 281-288.

[Caillat 1996] T. Caillat, A. Borshchevsky, J.-P. Fleurial. Properties of single crystalline semiconducting $CoSb_3$. J. Appl. Phys. 80 (1996) 4442-4449.

[Case 1984] E. D. Case and C. Glinka, Characterization of Microcracks in $YCrO_3$ Using Small Angle Neutron Scattering and Elasticity Measurements, J. Mater. Sci. 19 (1984) 2962-2968.

[Case 1993] E.D. Case, Y. Kim, The Effect of Surface Limited Microcracks on the Effective Young's Modulus of Ceramics, J. Mater. Sci. 28 (1993) 1885-1900.

[Case 2005] E.D. Case, I.O. Smith, M.J. Baumann. "Microcracking and porosity in calcium phosphides and the implications for bone tissue engineering" Mat. Sci. Eng. A 390 (2005) 246-254.

[Feldman 1995] J.L. Feldman, D.J. Singh. Lattice dynamics of skutterudites: First-principles and model calculations for CoSb3. Phys. Rev. B 53 (1995) 6273-6282.

[Francombe 1958] M.H. Francombe. Structure-cell data and expansion coefficients of bismuth telluride. Br. J. Appl. Phys. 9 (1958) 415-417.

[Fujishiro 2005] H. Fujishiro, K. Katagiri, A. Murakami, Y. Yoshino, K. Noto. Database for thermal and mechanical properties of REBaCuO bulks. Physica C 426-431 (2005) 699-704.

[Grzesik 2008] W. Grzesik. "Machining of Hard Materials", chapter 4 in Advanced machining processes of metallic material: Theory, Modeling and Applications, Elsevier Science (2008) 97-126. J. Am. Ceram. Soc. 90 (2007) 673-680.

[Hall 2008] B.D. Hall. Powder processing, powder characterization, and mechanical properties of LAST (Lead-Antimony-Silver-Tellurium) and LASTT (Lead-Antimony-Silver-Tellurium -Tin) thermoelectric materials. Unpublished master's thesis, Michigan State University, 2008.

[Hasselman 1993] D.P.H. Hasselman, K.Y. Donaldson, E.M. Anderson, T.A. Johnson, Effect of thermal history on the thermal diffusivity and thermal expansion of an alumina-aluminum titanate composite. J. Am. Ceram. Soc. 76 (1993) 2180-2184.

[Jiang 2005] J. Jiang, L.D. Chen, S.Q. Bai, Q. Yao, Q. Wang. Fabrication and thermoelectric performance of textured n-type Bi-2(Te,Se)(3) by spark plasma sintering. Mat. Sci. Eng. B 117 (2005) 334-338.

[Johnson 2001] E. Johnson. Simulations of microcracking in the process region of ceramics with a cell model. Int. J. Fract.111 (2001) 361-380.[Kenfaui 2010] D. Kenfaui, D. Chateigner, M. Gomina, J. G. Noudem. Texture, mechanical and thermoelectric properties of Ca3Co4O9 ceramics. J. Alloys Compd. 490 (2010) 472-479.

[Kraemer 2005] A.C. Kraemer, C.A. Perottoni, J.A.H. da Jornada. Isothermal equation of state for the skutterudites $CoSb_3$ and $LaFe_3CoSb_{12}$. J. Solid State Comm. 133 (2005) 173-176.

[Liu 2007] W.-S. Liu, B.-P. Zhang, J.-F. Li, H.-L. Zhang, L.-D. Zhao. Enhanced thermoelectric properties in $CoSb_{3-x}Te_x$ alloys prepared by mechanical alloying and spark plasma sintering. J. Appl. Phys. 102 (2007) 103717.

[Meisner 1998] G.P. Meisner, D.T. Morelli, S. Hu, J. Yang, C. Uher. Structure and Lattice Thermal Conductivity of Fractionally Filled Skutterudites: Solid Solutions of Fully Filled and Unfilled End Members. Phys. Rev. Lett. 80 (1998) 3551-3554.

[Migliori 1997] A. Migliori, J.L. Sarrao. Resonant Ultrasound Spectroscopy: Applications to Physics, Materials Measurements, and Nondestructive Evaluation. Academic Press, New York, 1997.

[Ni 2010] J.E. Ni, E.D. Case, K.N. Khabir, R.C. Stewart, C.I. Wu, T.P. Hogan, E.J. Timm, S.N. Girard, M.G. Kanatzidis. Room temperature Young's modulus, shear modulus, Poisson's ratio and hardness of PbTe-PbS thermoelectric materials. Mat. Sci. Eng. B 170 (2010) 58-66.

[Nye 1957] J.F. Nye. Physical properties of crystals. Clarendon Press, Oxford (1957).

[Oliver 1992] W.C. Oliver, G.M. Pharr. An improved technique for determining hardness and elastic modulus using load and displacement sensing indentation experiments. J. Mater. Res. 7 (1992) 1564-1583.

[Radovic 2004] M. Radovic, E. Lara-Curzio, L. Reister, Comparison of different experimental techniques for determination of elastic properties of solids, Mat. Sci. Eng. A368 (2004) 56-70.

[Ravi 2008] V. Ravi, S. Firdosy, T. Caillat, B. Lerch, A. Calamino, R. Pawlik, M. Nathal, A. Sechrist, J. Buchhalter, S. Nutt. Mechanical Properties of Thermoelectric Skutterudites. Space Technology and Applications International Forum – STAIF (2008) 656-662.

[Recknagel 2007] C. Recknagel, N. Reinfreid, P. Höhn, W. Schnelle, H. Rosner, Yu. Grin, A. Leithe-Jasper. Application of spark plasma sintering to the fabrication of binary and ternary skutterudites. Science and Technology of Advanced Materials 8 (2007) 357-363.

[Ren 2006] F. Ren, E.D. Case, E.J. Timm, M.D. Jacobs, H.J. Schock. Weibull analysis of the biaxial fracture strength of a cast p-type LAST-T thermoelectric material. Phil. Mag. Lett. 86 (2006) 673-682.

[Ren 2009] F. Ren, E.D. Case, J.E. Ni, E.J. Timm, E. Lara-Curzio, R.M. Trejo, C.-H. Lin, M.G. Kanatzidis. Temperature-dependent elastic moduli of lead telluride-based thermoelectric materials. Philos. Mag. 89 (2009) 143-167.

[Rice 1998] R.W. Rice. Porosity of Ceramics, Marcel Dekker, New York (1998) 43-167.

[Salvador 2006] J.R. Salvador, J. Yang, X. Shi, H. Wang, A.A. Wereszczak, H. Kong, C Uher. Transport and mechanical properties of Yb-filled skutterudites. Philos. Mag. 89 (2009) 1517-1534.

[Schmidt 2010] R.D. Schmidt, J.E. Ni, E.D. Case, J.S. Sakamoto, D.C. Kleinow, B.L. Wing, R.C. Stewart, E. J. Timm. Room temperature Young's modulus, shear modulus, and Poisson's ratio of $Ce_{0.9}Fe_{3.5}Co_{0.5}Sb_{12}$ and $Co_{0.95}Pd_{0.05}Te_{0.05}Sb_3$ skutterudite materials. J. Alloys Compd. (2010) 303-309.

[Seo 1997] J. Seo, K. Park, D. Leo, C. Lee. Thermoelectric properties of hot pressed n-type $Bi_2Te_{2.85}Se_{0.15}$ compounds doped with SbI_3 Mater. Sci. Eng. B49 (1997) 247-250.

[Shin 1988] B.C. Shin, H.G. Kim. Partial discharge, microcracking, and breakdown in BaTiO3 ceramics. Ferroelectrics 77: 1 (1988) 161-166.

[Thakur 2004] S.K. Thakur, B.K. Dhindaw, N. Hort, K.U. Kainer. Some studies on the thermal-expansion behavior of C-fiber SiC_p, and in-situ Mg_2Si-reinforced az31 Mg alloy-based hybrid composites.

[Ueno 2005] K. Ueno, A. Yamamoto, T. Noguchi, T. Inoue, S. Sodeoka, H. Obara. Optimization of hot-pressed conditions of Zn_4Sb_3 for high thermoelectric performance. II. Mechanical properties. J. Alloys Compd. 388 (2005) 118-121.

[Wachtman 1996] J.B. Wachtman, Mechanical properties of ceramics. Wiley, New York (1996) 92-115.

[Xu 1995] H.H.K. Xu, L Wei, S Jahanmir. "Grinding force and microcrack density in abrasive machining of silicon nitride" J. Mater. Res. 10 (1995) 3204-3209.

[Yang 2007] J. Yang, G.P. Meisner, C.J. Rawn, H. Wang, B.C. Chakoumakos, J. Martin, G.S. Nolan, B.L. Pedersen, J.K. Stalik. Low temperature transport and structural properties of misch-metal-filled skutterudites. J. Appl. Phys 102 (2007) 083702.

[Yang 2009a] X. Yang, L. Liu, P. Zhai, Q. Zhang. Modeling of skutterudite $CoSb_3$ with molecular dynamics method. Comp. Mater. Sci. 44 (2009) 1390-1396.

[Yang 2009b] X. Yang, P. Zhai, A. Zhou, L. Liu, Q. Zhang. Molecular Dynamics Simulation on Mechanics of Skutterudite CoSb3 Nanowire. J. Electron. Mater. 7 (2009) 1189-1193.

[Zhao 2009] D. Zhao, X. Li, L. He, W. Jiang, L. Chen. Interfacial evolution behavior and reliability evaluation of $CoSb_3$/Ti/Mo-Cu thermoelectric joints during accelerated thermal aging. J. Alloys Compd. 477 (2009) 425-431.